

Synthesis and Characterization of Diamond Like Carbon (DLC) Based Nano-composite Thin Films Grown by PLD

By

Madhusmita Panda

(Enrolment No. PHYS 02 2013 04 007)

Indira Gandhi Centre for Atomic Research, Kalpakkam

*A thesis submitted to the
Board of Studies in Physical Sciences
In partial fulfillment of requirements
for the Degree of*

DOCTOR OF PHILOSOPHY

of

HOMI BHABHA NATIONAL INSTITUTE

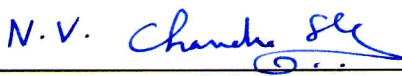



July, 2019

Homi Bhabha National Institute¹


Recommendations of the Viva Voce Committee


As members of the Viva Voce Committee, we certify that we have read the dissertation prepared by **Mrs. Madhusmita Panda** entitled "**Synthesis and Characterization of Diamond Like Carbon (DLC) based Nano-composite Thin Films Grown by PLD**" and recommend that it may be accepted as fulfilling the thesis requirement for the award of Degree of Doctor of Philosophy.


(Chairman- Dr. N. V. Chandra Shekar) Date: 4/2/2020


(Guide/ Convener- Dr. M. Kamruddin) Date: 4/2/20


(Co-guide- Dr. R. Krishnan) Date: 04/feb/2020


(External- Examiner: Dr. Bodh Raj Mehta) Date: 04/02/2020


(Member-1: Dr. Tom Mathews) Date: 04/02/2020


(Member-2: Dr. Arup Dasgupta) Date: 04/02/2020


(Member-3: Dr. Awadhesh Mani) Date: 04/02/2020

Final approval and acceptance of this thesis is contingent upon the candidate's submission of the final copies of the thesis to HBNI.

I/We hereby certify that I/we have read this thesis prepared under my/our direction and recommend that it may be accepted as fulfilling the thesis requirement.

Date: 04/02/2020

Place: Kalpakkam

Signature

Co-guide

Signature

Guide

¹ This page is to be included only for final submission after successful completion of viva voce.

STATEMENT BY AUTHOR

This dissertation has been submitted in partial fulfillment of requirements for an advanced degree at Homi Bhabha National Institute (HBNI) and is deposited in the Library to be made available to borrowers under rules of the HBNI.

Brief quotations from this dissertation are allowable without special permission, provided that accurate acknowledgement of source is made. Requests for permission for extended quotation from or reproduction of this manuscript in whole or in part may be granted by the Competent Authority of HBNI when in his or her judgment the proposed use of the material is in the interests of scholarship. In all other instances, however, permission must be obtained from the author.

Date: 04/02/2020

Place: Kalpakkam


Madhusmita Panda

DECLARATION

I, hereby declare that the investigation presented in the thesis has been carried out by me. The work is original and has not been submitted earlier as a whole or in part for a degree / diploma at this or any other Institution / University.

M. Panda
04/02/2020
Madhusmita Panda

List of Publications arising from the thesis

(a) Journals:

1. Nano scale investigation of particulate contribution to diamond like carbon film by pulsed laser deposition, **M. Panda**, G. Mangamma, R. Krishnan, K. K. Madapu, D. N. G. Krishna, S. Dash and A. K. Tyagi, **RSC Adv.**, **2016**, **6**, **6016–6028**.
2. Tuning the tribological property of PLD deposited DLC-Au nano-composite thin films, **M. Panda**, R. Krishnan, N.G. Krishna, S. Amirthapandian, P. Magudapathy, M. Kamruddin, **Ceramics International**, **2019**, **45**, **8847–8855**.
3. Influence of particulate on surface energy and mechanical property of diamond-like carbon films synthesized by pulsed laser deposition, **M. Panda**, R. Krishnan, K. K. Madapu, P. Panda, M. Sahoo, R. Ramaseshan, T. Sundari and M. Kamruddin, **Applied Surface Science**, **2019**, **484**, **1176-1183**.

(b) Under Preparation:

1. Influence of Au cluster size on optical, surface energy, mechanical and tribological property of DLC- Au nano-composite films, **M. Panda**, R. Krishnan, P. Panda, M. Sahoo, K. G. Raghavendra, R. Ramaseshan, A. Dasgupta and M. Kamruddin.

(c) Conference Proceedings:

1. Spectroscopic Studies on Diamond Like Carbon films synthesized by Pulsed Laser Ablation, **M. Panda**, R. Krishnan, T. R. Ravindran, A. Das, G. Mangamma, S. Dash and A. K. Tyagi, **AIP Conference Proceedings**, **2016**, **1731**, **080040**, **1-3**.

2. Intrinsic stress modulation in diamond like carbon films with incorporation of gold nanoparticles by PLA, **M. Panda**, R. Krishnan, N. G. Krishna, K. K. Madapu and M. Kamruddin, **AIP Conference Proceedings**, **2018**, **1942**, **080023**; 1-3.

(d) Conference Presentations:

1. Evolution of structural and optical properties of DLC with energy density of Nd: YAG laser, **M. Panda**, R. Krishnan, T. R. Ravindran, A. Das, G. Mangamma, S. Dash and A.K. Tyagi, **ISRS-2014, IIT Madras, India. (Contributory talk)**.
2. Evolution of indentation hardness and modulus of DLC films with laser pulse energy, **M. Panda**, R. Krishnan, P. Panda, R. Ramaseshan, M. Kamruddin, **RSM MSEN- 2018, Kalpakkam, India. (Poster Presentation)**

(e) Other Publications (Not part of the present thesis):

1. Optimization of Selenization and Sintering Conditions of DC Magnetron Sputtered Ag/In/Ag/In Multi-Layer Metal Precursor for Preparation of AgInSe₂ Thin Films, R. Panda, **M. Panda**, H. Rath, P. Dash, R. Naik, U. P. Singh, N. C. Mishra, **Advanced Science Letters**, **2014**, **20**, **3-4**, **631-634**.
2. Annealing induced AgInSe₂ formation from Ag/In/Ag/In multilayer film for solar cell absorbing layer, R. Panda, **M. Panda**, H. Rath, U.P. Singh, R. Naik, N.C. Mishra, **Optical Materials**, **2018**, **84**, **618-624**.
3. Structural and morphological modifications of AgInSe₂ and Ag₂Se composite thin films on 140 MeV Ni ion irradiation, R. Panda, **M. Panda**, H. Rath, B. N. Dash, K. Asokan, U. P. Singh, R. Naik, N. C. Mishra, **Applied Surface Science**, **2019**, **479**, **997-1005**.

4. Thermal annealing induced modifications on the structural and optical properties of AgInSe₂ thin film. R. Panda, **M. Panda**, R. Naik, U. P. Singh, and N. C. Mishra. **AIP Conference Proceedings**, 2017, 1832, 080042, 1-3.

M. Panda
04/02/2020
Madhusmita Panda

DEDICATED

To

The Almighty Goddess.....



"I did my best and God did the rest"

To

"My Parents"

To

"My Teachers"

To

My Sweet Heart "Janu"

ACKNOWLEDGEMENTS

First of all, I express my deep sense of gratitude to my research supervisors Dr. M. Kamruddin and Dr. S. Dash for their valuable guidance throughout my Ph. D. tenure. I am extremely grateful to my mentor Kamruddin Sir, for all his supports during the struggling periods of Ph. D. days and the task of thesis writing. I specially thank Dr. S. Dash for his experimental supports, ideas and suggestions.

I would like to extend my sincere thanks to my co-guide Dr. R. Krishnan for PLD training and all experimental co-operations during my research period.

I am extremely indebted to my Doctoral committee members, Dr. N. V. Chandra Shekar, Dr. Tom Mathews, Dr. Arup Dasgupta, and Dr. Awadhesh Mani. Their insightful comments regarding my work and constructive criticism have directed my thesis in a proper manner.

I gratefully acknowledge financial support given by Department of Atomic Energy, India.

I sincerely thank the present director of IGCAR, Dr. A. K. Bhaduri and the former directors Dr. P. R. Vasudeva Rao and Dr. S. A. V. Satyamurthy for allowing me to carry out my research work.

I would also like to extend my deep gratitude to the present Director of Materials Science Group, Dr. Shaju K. Albert and the former directors Dr. G. Amarendra, Dr. C. S. Sundar and Shri. M. P. Janawadkar for providing the conducive atmosphere for my smooth research.

I would like to thank Dr. R. Rajaraman, Dr. N. V. Chandra Shekar and Dr. B. V. R. Tata, present and past Dean, Physical Sciences for their support. I would also like to thank Dr. Lakshmi Narasimman and Dr. M. Saibaba for their academically supports and the wonderful hospitality during my stay at JRF Enclave. I want to thank the reviewers of my thesis and manuscripts for their valuable comments and suggestions which helped in the improvement of the research articles.

I would like to extend my sincere thanks to my collaborators, Dr. T. R. Ravindran and Dr. K. K. Madapu, for micro-Raman experiments, Dr. G. Mangamma, for AFAM experiments, Mr. N. G. Krishna, for XPS experiments, Dr. Niranjana Kumar, for Tribology experiments, Dr. S. Amirthapandian, for TEM and EELS experiments, Dr. R. Ramaseshan and Dr. P. Panda, for nano-indentation experiments, Dr. S. Ilango,

Mrs. Sunitha and Mr. Magudapathy, for GIXRD experiments, Dr. T. Sundari and Dr. M. Sahoo for contact angle measurements, Dr. A. Dasgupta, Dr. K. G. Raghavendra and Mr. Aji kumar, for FESEM and EDS experiments and analysis, A. Das for UV-Vis spectroscopy, experiments.

It is my pleasure to express my deepest gratitude to my M. Phil supervisor Dr. N.C. Mishra, Utkal University for his motivations and guidance for research, which influenced me a lot. I would like to extend my sincere thanks to Dr. G. Mangamma for fruitful discussions and motivations during the initial stage of my research.

I would like to thank my seniors, friends and juniors Mr. Shashwat Swain, Dr. Subrata Ghosh, Dr. Avinash Patsha, Dr. Dr. A. K. Sivadasan, Dr. K. Srinivasan, Dr. K. G. Raghavendra, Dr. Preethi, Dr. Kamali Kesavan, Mr. Ashok Bahuguna, Padmalochan, Nilakantha, Lakshmanan, Irshad, Radhikesh, Vairavel, Zaibudeen, Manoj, Shivang, Nidhin, Vikash, Santhosh, Sumathi, Santanu, Anil, Binaya, Bijaya, Alok, Pradosh, Madhav, Arpita, Alaka, Shradha, Ijee, Prajna for their suggestions, encouragement, friendship and co-operations during these years.

Special thanks to my junior Gopinath, for being there for me, at any professional situation. He is, always the go to person for me.

I would also like to thank all my well-wishers, all the members of the Materials Science Group and friends in the JRF enclave.

No words shall be enough to thank my family-friend Sulagna (Mama) for taking care of my daughter during the vital period of my research, when no-one from my family could help me.

*I am thankful to my beloved parents, siblings, other family members and my respected father in-law for their support, love, encouragement, blessings and belief in me. Especially, I am grateful to my elder brother (**MITU NANA**), who is the founder of my career, as well as my proponent at each and every worst situation. I thank my beloved daughter **TANU** being in my life, whose smile is a source of energy and inspirations for me to overcome all obstacles in my life. Last, but not least, I would like to thank my dear husband **HARA** who played a vital role in completion of this thesis. Without his support starting from personal to professional during each and every tough time, it was impossible for me to finish my PhD work successfully.*

*Lastly and most importantly I thank the Almighty.... **“Maa Tarini”***

CONTENTS

	Page No.
SUMMARY	i
LIST OF FIGURES	iii
LIST OF TABLES	vi
CHAPTER 1 INTRODUCTION	1
1.1. DLC	3
1.2. Properties and classification of DLC	4
1.3. Deposition techniques for non-hydrogenated DLC	5
1.4. Growth mechanism of DLC by PLD	7
1.5. Limitations for DLC growth by PLD with possible solutions	9
1.6. Motivation and Research objectives	15
CHAPTER 2 EXPERIMENTAL TECHNIQUES	19
2.1. Introduction	19
2.2. PLD Growth techniques	20
2.2.1. LASER	24
2.2.1.1. Nd: YAG LASER	25
2.2.1.2. KrF LASER	27
2.2.2. UHV Chamber	29
2.2.3. Target holder and automated target carousel controller (ATCC)	30
2.2.4. Beam steering optics	31
2.2.5. Target	32
2.3. Characterization Techniques	32
2.3.1. Thickness Measurement	33
2.3.2. Raman Spectroscopy	33
2.3.3. X-ray Photoelectron Spectroscopy (XPS)	36

2.3.4.	Scanning Probe Microscopy (SPM)	38
2.3.5.	Field Emission Scanning Electron Microscope (FESEM) and Energy Dispersive X-ray Spectroscopy (EDS)	42
2.3.6.	X-ray Diffraction (XRD)	44
2.3.7.	Transmission Electron Microscopy (TEM)	45
2.3.8.	Electron Energy Loss Spectroscopy (EELS)	46
2.3. 9.	Contact Angle Measurement	48
2.3.10.	Nano Indentation	49
2.3.11.	Tribometer	52
2.4.	Summary	53

CHAPTER 3 RAMAN INVESTIGATION OF PARTICULATE LADEN DIAMOND-LIKE CARBON FILMS GROWN BY ND: YAG LASER ABLATION. 55

3.1.	Introduction	55
3.2.	Characterizations	57
3.3.	Results and Discussion	57
3.3.1.	Thickness of DLC films	57
3.3.2.	Morphological Analysis	57
3.3.2.1.	FESEM Study	57
3.3.2.2.	AFM Study	59
3.3.3.	Influence of particulate on DLC surface studied by Visible Raman Mapping	59
3.3.4.	Multi-excitation Raman Analysis on Flat and Particulate regions	63
3.3.4.1.	Visible Raman Analysis	63
3.3.4.2.	UV Raman Analysis	67
3.4.	Summary	74

CHAPTER 4 INFLUENCE OF PARTICULATES ON SURFACE ENERGY, COMPOSITION AND MECHANICAL PROPERTIES OF DLC FILMS 75

4.1.	Introduction	75
------	--------------	----

4.2.	Characterizations	76
4.3.	Results and Discussion	77
4.3.1.	Surface energy determination	77
4.3.2.	Compositional Analysis	80
4.3.3.	Determination of Relative Stiffness Constant	83
4.3.4.	Nano-Indentation Hardness and Elastic Constant determination	87
4.4.	Summary	91
CHAPTER 5	INVESTIGATION OF DLC- AU NANO-COMPOSITE FILMS GROWN BY EXCIMER LASER ABLATION	93
5.1.	Introduction	
5.2.	Characterizations	94
5.3.	Results and Discussion	94
5.3.1.	Thickness of DLC- Au nano- composite films	94
5.3.2.	Morphological Analysis	
5.3.2.1.	FESEM Study	95
5.3.2.2.	AFM Study	96
5.3.3.	Structural Analysis	97
5.3.3.1.	XRD Study	97
5.3.3.2.	TEM Study	99
5.3.4.	Compositional Analysis	
5.3.4.1.	XPS Study	100
5.3.4.2.	EDS Study	104
5.3.5.	Vibrational Analysis	105
5.3.5.1.	EELS Study	105
5.3.5.2.	Raman Study	107
5.4.	Summary	110
CHAPTER 6	A STUDY ON MECHANICAL AND TRIBOLOGICAL PERFORMANCE OF DLC- AU NANO-COMPOSITES	111
6.1.	Introduction	111

6.2. Characterizations	112
6.3. Results and Discussion	113
6.3.1. Mechanical properties of DLC- Au nano- composites	113
6.3.2. Tribological study of DLC- Au nano- composites	115
6.3.3. Raman investigation of tribo-tracks	117
6.3.4. Raman investigation of ball scars	119
6.4. Summary	122
 CHAPTER 7 CONCLUSIONS AND FUTURE DIRECTIONS	 125
7.1. Conclusions	125
7.2. Future Directions	127
 REFERENCE	 129

SUMMARY

The present Thesis work is focused on the synthesis of particulate laden un-hydrogenated Diamond-like carbon (DLC) films and un-hydrogenated DLC-Au nano-composites by Pulsed laser deposition (PLD) with the prime objective to explore their mechanical and tribological properties at the optimum growth condition. A brief account on the present investigation and the key findings are listed below.

The number density and size of particulates are highly dependent on laser pulse energy. Thus, particulate laden un-hydrogenated DLC films were synthesized at various laser pulse energies (100-400 mJ), using an Nd: YAG laser (1064 nm) to study the influence of particulates on DLC properties. Morphological studies by Atomic Force Microscopy (AFM) and Field Emission Scanning Electron Microscope (FESEM), reveal that size and number density of particulates increases with increase in laser pulse energy. The vibrational investigation of these specimens was carried out by vis Raman mapping on DLC surface including particulate and multi- Raman excitation on flat and particulate regions separately. These studies concluded that the reason behind evolution of sp^3 content, sp^2 cluster size, bond length and angle disorder of sp^2 cluster with laser pulse energy on flat and particulate regions of DLC films are completely two different aspects.

The sp^3 content and sp^2 clusters play vital role in tuning the physical and mechanical properties of DLC specimens. In this regard, several characterization techniques such as contact angle measurement, X-Ray Photoelectron Spectroscopy (XPS), Atomic Force Acoustic Microscope (AFAM) and nano-indentation were employed on particulate laden DLC films to study the influence of particulates on surface energy, composition and mechanical properties of DLC films. It was found that evolution of surface energy of DLC films with laser pulse energy depend on particulate property

evolution, whereas relative stiffness and indentation hardness depend on sp^3 content. Thus, 300 mJ laser pulse energy was found as the threshold energy to obtain maximum sp^3 content with highest relative stiffness on flat region, indentation hardness (46 GPa) and indentation modulus (340 GPa).

. DLC-Au nano-composites have also been synthesized from a graphite-Au composite target by laser (KrF) ablation at various laser indexing angles (10^0 , 20^0 and 30^0). Structural characterizations by X-Ray diffraction (XRD) and Transmission Electron Microscopy (TEM) confirm the presence of Au nano-clusters and revealed that DLC-Au nano-composite (DLC-Au: 4.7%) synthesized at 30^0 indexing angle possess the smallest Au cluster (1.5 nm). The compositional analysis of these specimens ensured that DLC-Au: 4.7% possesses lowest Au content (4.7 at %) with highest number of Au^{+1} species and sp^3 content (41.4%). The Raman analysis confirmed maximum compressive stress reduction (7.9 GPa) in DLC-Au: 4.7% nano-composite films. .

Subsequently, the mechanical properties and tribological behavior of DLC-Au nano-composites were explored. It was found that DLC-Au: 4.7% exhibited maximum indentation hardness (28 ± 0.9 GPa) and elastic modulus (265 ± 14 GPa). It was also noticed that the tribological behavior of DLC-Au: 4.7% nano-composite showed ultralow CoF value of ~ 0.05 and high wear resistance with a gradual decrease in CoF to ultra-low value with sliding distance. A comprehensive micro-Raman spectroscopy investigation was carried out on tribo-track and ball scar to reveal the reason behind the gradual decrease in CoF to ultra-low value. The study confirmed that a graphitized (sp^2 rich) tribo- film formed on ball scar acted as a lubricant and governed the tribological behaviors.

LIST OF FIGURES

Figure No.	Figure Caption	Page No.
1.1.	A possible structure of DLC.	3
1.2.	Schematic diagram of Sub-plantation model.	7
1.3.	Schematic diagram of various film architectures.	13
2.1.	Schematic diagram of PLD set up.	23
2.2.	Photograph showing UHV deposition chamber with nanosecond pulsed Nd: YAG and KrF laser systems.	23
2.3.	Energy level diagram of a Nd: YAG laser	26
2.4.	Graphite-Au Target arrangement	29
2.5.	Photograph of target assembly and microprocessor based automatic target carrousel controller (ATCC).	30
2.6.	Photograph of beam steering optics with optical mount for Nd: YAG and KrF lasers.	32
2.7.	Schematic view of (a) scattering process in material with incident light, and (b) Raman spectrometer set up.	35
2.8.	Schematic diagram of XPS processes.	37
2.9.	A schematic representation of a) force displacement curve of tip and sample and b) Atomic Force Microscope (AFM)	39
2.10.	Schematic representation of X-ray diffraction process.	44
2.11.	Schematic illustration of indentation load-displacement curve with important measured parameters.	49
2.12.	Schematic illustration of the unloading process showing contact geometry parameters.	50
2.13.	(a). Schematic representation of ball on disc tribometer and (b) Experimental set up for tribological study.	53
3.1.	FESEM images of (a) DLC-1, (b) DLC-2, (c) DLC-3, and (d) DLC-4 films with particulate as inset.	58
3.2.	AFM images of (a) DLC-1, (b) DLC-2, (c) DLC-3, and (d) DLC-4 films.	58

3.3.	Visible Raman intensity mapping image for G-peak, D-peak and I_D/I_G of (a) DLC-1, (b) DLC-2, (c) DLC-3, and (d) DLC-4, respectively.	61
3.4.	Deconvoluted visible (514.5 nm) Raman spectra obtained from flat regions of (a) DLC-1, (b) DLC-2, (c) DLC-3, and (d) DLC-4 films.	63
3.5.	Deconvoluted visible (514.5 nm) Raman spectra obtained from particulate regions of (a) DLC-1, (b) DLC-2, (c) DLC-3, and (d) DLC-4 films.	64
3.6.	Deconvoluted UV (325 nm) Raman spectra obtained from flat region of (a) DLC-1, (b) DLC-2 (c) DLC-3, and (d) DLC - 4 films.	68
3.7.	Deconvoluted UV (325 nm) Raman spectra obtained from particulate region of (a) DLC-1, (b) DLC-2 (c) DLC-3, and (d) DLC - 4 films.	68
3.8.	G-peak Dispersion vs laser pulse energy for flat and particulate regions.	71
4.1.	Evolution of surface energy polar (P-SE), dispersive (D-SE) and total (SE)) and contact angle (water (W-CA) and diodo-methane (DM-CA)) of DLC specimens with laser pulse energy.	79
4.2.	De-convoluted XPS C1s peak of (a) DLC-1, (b) DLC-2, (c) DLC-3, and (d) DLC-4.	80
4.3.	AFM topography and AFAM (Mag) images (a) Si (111), (b) DLC-1, (c) DLC-2, (d) DLC-3, and (e) DLC-4 films.	83
4.4.	Indentation hardness as a function of penetration depth of Si (111) substrate and particulate laden DLC (DLC-1, DLC-2, DLC-3, and DLC-4) Films.	89
4.5.	Indentation Modulus as a function of penetration depth of Si (111) substrate and particulate laden DLC (DLC-1, DLC-2, DLC-3, and DLC-4) films.	89
4.6.	Evolution of H (GPa), E (GPa) values at 0.3 mN indentation load and sp^3 content of DLC-1, DLC-2, DLC-3, and DLC-4.	90

5.1.	FESEM micrographs of (a) DLC, (b) DLC-Au: 4.7%, (c) DLC-Au: 7.3%, and (d) DLC-Au: 12% specimens.	95
5.2.	AFM micrographs of (a) DLC, (b) DLC-Au: 4.7%, (c) DLC-Au: 7.3%, and (d) DLC-Au: 12% specimens.	96
5.3.	XRD patterns of (a) DLC, (b) DLC-Au: 4.7%, (c) DLC-Au: 7.3%, and (d) DLC-Au: 12% films.	97
5.4.	HRTEM micrographs of (a) DLC, (b) DLC-Au: 4.7% (c) DLC-Au: 7.3%, (d) DLC-Au: 12% films with corresponding diffraction patterns as insets (a ₁ , b ₁ , c ₁ , and d ₁).	98
5.5.	De-convoluted C 1s spectra of (a) DLC, (b) DLC-Au: 4.7% (c) DLC-Au: 7.3%, (d) DLC-Au: 12% specimens.	101
5.6.	(a) O 1s X-ray photoelectron emission lines, (b) Au 4f X-ray photoelectron emission lines and (c) De-convoluted Au 4f X-ray photoelectron emission lines.	102
5.7.	EDS spectra of (a) DLC, (b) DLC-Au: 4.7% (c) DLC-Au: 7.3%, (d) DLC-Au: 12% specimens.	105
5.8.	Carbon C (1s) K edge EELS spectra of (a) DLC, (b) DLC-Au: 4.7% (c) DLC-Au: 7.3%, and (d) DLC-Au: 12% specimens.	106
5.9.	De-convoluted Raman spectra of (a) DLC, (b) DLC-Au: 4.7% (c) DLC-Au: 7.3%, and (d) DLC-Au: 12% specimens.	108
5.10.	G-Peak position evolutions in DLC and DLC-Au nano composites specimens.	109
6.1.	Evolution of hardness (<i>H</i>) and elastic modulus (<i>E</i>) with Au content in DLC matrix.	113
6.2.	Micro tribo test carried out at ambient and unlubricated conditions on (a) Si(100), (b)DLC, (c)DLC-Au: 12%, (d)DLC-Au: 7.3%, and (e)DLC-Au: 4.7% specimen.	114
6.3.	Optical Image of Tribo-track and corresponding Raman spectra at various locations of (a) DLC -50000 laps, (b). DLC-Au: 4.7%-	117

	15000 laps, and (c) DLC-Au: 4.7% -50000 laps specimens.	
6.4.	Optical Image of scar on ball and corresponding Raman spectra at various regions of (a) DLC -50000 laps, (b). DLC – Au: 4.7% –15000 laps and (c) DLC – Au: 4.7% –50000 laps specimens.	118
6.5.	I_D - I_G determination from deconvoluted Raman spectra on tribo-track at various regions of (a) DLC-Au: 4.7%-15000 laps and (b) DLC-Au: 4.7%-50000 laps specimens.	120
6.6.	I_D - I_G determination from deconvoluted Raman spectra on ball scar at various regions of (a) DLC-Au: 4.7%-15000 laps and (b) DLC-Au: 4.7%-50000 laps specimens.	121
6.7.	I_D/I_G vs laps on track and ball scar.	122

LIST OF TABLES

Table No.	Table Caption	Page No.
3.1.	Deconvoluted data of visible (514.5 nm) Raman spectra obtained from flat regions of DLC films	65
3.2.	Deconvoluted data of visible(514.5 nm) Raman spectra obtained from particulate regions of DLC films	66
3.3.	Raman Deconvoluted Data obtained from Flat and Particulate region of DLC - 1, DLC- 2, DLC-3, and DLC-4 for UV (325 nm) excitation.	70
4.1.	XPS C 1s spectra de convolution results of particulate laden DLC films synthesized at various laser pulse energies.	81
4.2.	Contact resonance and relative stiffness value of particulate laden DLC films.	85
5.1.	Atomic % of different elements, sp^3 , and sp^2 bonding content as obtained from XPS.	100
5. 2.	Peak position and FWHM of various Au state.	103

CHAPTER 1

Introduction

“Life exists in the universe only because the carbon atom possesses certain exceptional properties”

James Jeans

Present time technology demands superior properties from the materials used in a variety of industrial applications, to take into account of wear and tear, chemical attack, high temperature corrosion, oxidation and other extreme environments. Friction and wear determine the efficiency and life time of any machinery. The interaction between the material and the environment initiates at the surface and hence, the surface of any engineering component plays a vital role in regulating its performance and longevity leading to economic benefits. However, many novel applications demand the bulk material properties such as:- composition and structure to be very different from that of the surface which is exposed to hostile atmosphere. Hence, the solution is to model a composite product, consisting of inner structural material with one set of properties and covered with a surface having different set of functional properties. Therefore, coated parts usually show a superior performance compared to uncoated work pieces.

In current technological development, carbon plays a major role with its many numbers of allotropes. Specifically, the extraordinary mechanical and tribological properties of Diamond- like Carbon (DLC) and DLC based nano-composites have drawn remarkable attention of academic and industrial community. One of the current demands in tribological

performance is to develop coatings with low coefficients of friction (*CoF*) for diverging environmental conditions. For example, in aerospace applications, the choice and design of materials for space satellites needs enormous attention, as it experiences extreme temperature fluctuations in addition to moisture during launch.^{1, 2} Generally, the low friction behavior of solid lubricants varies from one environment to another. For example, graphite exhibits low coefficients of friction value in humid air while high in vacuum. Hence, a composite coating with self-adaptive low coefficients of friction (*CoF*) as well as superior wear resistance is desirable for diversified environmental applications. A recent review by Pogrebnjak *et. al.* covers experimental research on nano-composite, multielement and multilayer protective coatings with various chemical compositions, specific phase composition, structure and substructure for adaptive behavior of such systems in tribological applications under extreme operating conditions.³ It is observed that decrease of the individual phase size to few nanometers in the composite coating provided a pathway to model adaptive or so called, smart tribological coatings. These coatings were designated as "chameleon" due to their potential to resist friction and wear simultaneously by modification of surface chemistry and microstructure with respect to variable environmental and loading conditions. A literature survey on chameleon nano-composite indicated that DLC acts as hard amorphous phase for lubrication under humid environmental conditions.^{1, 2, 4} Among various techniques used for synthesizing DLC based tribological coatings, Pulsed Laser Deposition (PLD) has been used extensively to synthesize single phase solid lubricants to complex hard and environmentally adaptive chameleon nano-composites.^{2, 4, 5}

This chapter presents an introduction to DLC, its properties and classification followed by a discussion on deposition techniques for un-hydrogenated DLC, growth

mechanism of DLC by PLD and limitations for DLC growth by PLD with possible solutions, finally motivation and research objectives of the thesis.

1.1. Diamond-like Carbon (DLC)

Carbon exhibits both crystalline and disorder structures. This unique nature of carbon arises owing to its ability to exist in multiple hybridization states viz., sp^3 , sp^2 and sp^1 . Graphite and diamond are the crystalline form of carbon. In graphite, one carbon atom is linked to four other carbon atoms. Three carbon atoms are in the basal plane by sharing 3 electrons via three σ bonds and the fourth electron forms π orbital perpendicular to the basal plane forming a three-fold coordinated sp^2 configuration.

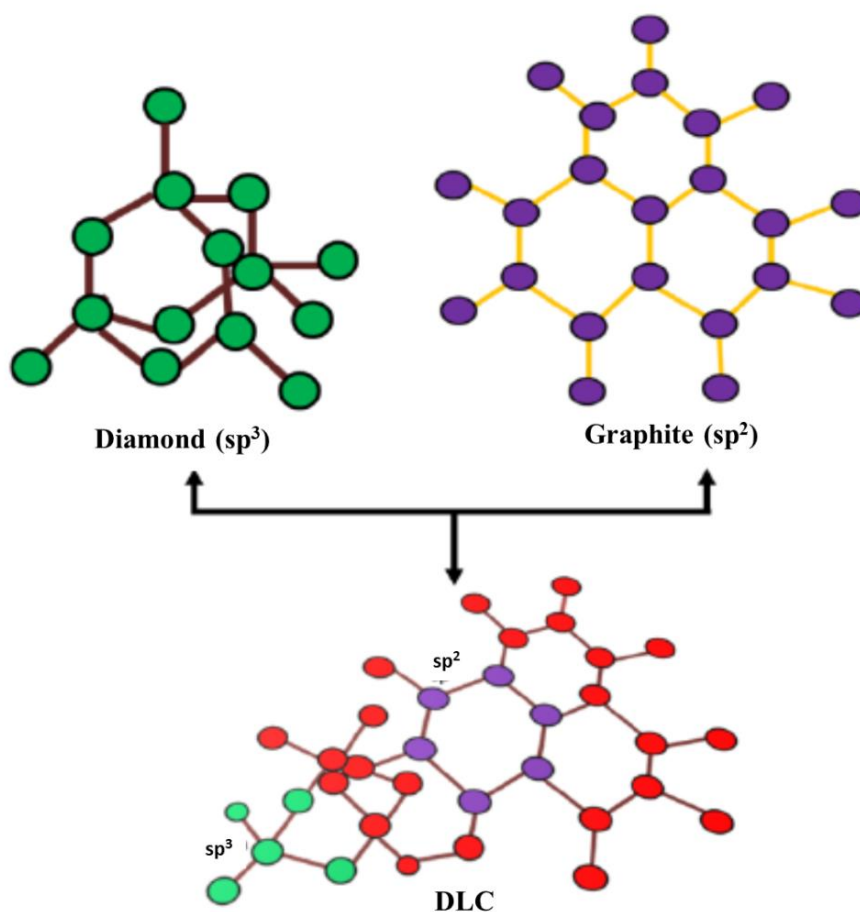


Figure 1.1. A possible structure of DLC.

However, in case of diamond, the four valence electrons of each carbon atom are linked by a tetrahedral sp^3 orbital, that leads to a strong σ bond with an adjacent atom. Apart from the crystalline forms, carbon also exists in disordered amorphous form. This metastable carbon phase consists of both sp^3 and sp^2 hybridized carbon atoms. In 1950's first DLC films were discovered by Heinz Schmellenmeier.⁶ However, the term “diamond- like” was first coined by Aisenberg and Chabot for hard, transparent, insulating amorphous carbon films, to signify that the properties of the synthesized carbon films are similar to those of diamond.⁷ This metastable amorphous carbon material is a mixture of sp^3 and sp^2 hybridized carbon atoms. **Figure 1.1.** represents a possible structure of DLC with sp^3 and sp^2 hybridized bonds.

1.2. Properties and classification of DLC

The DLC exhibit the intermediate properties of both graphite and diamond. They are extensively used for cutting tools, anticorrosive coatings in addition to tribological, electrochemical applications.⁸⁻¹⁰ In recent times, the DLC films have also drawn substantial attention from electronic industries, for protective layer coatings in magnetic storage devices as well as micro-electro mechanical systems (MEMS) due to its relatively higher hardness, elastic modulus, electrical resistivity, thermal conductivity, optical transparency, chemical inertness as well as good field emission properties.¹¹⁻¹⁷ Generally, the ratio of sp^3 to sp^2 bonds in DLC controls the properties of the film and classified as tetrahedral amorphous carbon (*ta-C*), DLC and amorphous carbon (*ac*) categories with sp^3 content > 70 %, 20-70% and < 20 %, respectively. In addition, depending on the hydrogen content, all the above mentioned categories can also be classified as hydrogenated and un-hydrogenated.¹⁴⁻¹⁷ The hydrogenated DLC film show better tribology property under vacuum and inert environment as compared to humid conditions due to hydrogen terminated dangling bonds, which exhibit

weak Van der Waals's force between the surfaces in contact.¹⁸⁻²⁰ In the humid environment this mechanism is hindered for the hydrogenated DLC films due to the presence of water molecules, which results in high coefficient of friction.²¹ Hence, un-hydrogenated DLC films exhibits low friction under humid conditions.²² In addition, graphitization sets in un-hydrogenated DLC films at 550 °C on exposure to oxygen atmosphere while hydrogenated DLC exhibit at 250 °C.²³ Generally, the temperature at the sliding contact during friction can reach around 500 °C easily. Hence, un-hydrogenated DLC film finds better tribological applications than hydrogenated DLC films under humid and high temperature conditions.

1.3. Deposition techniques for un-hydrogenated DLC

In the light of above discussion, the properties of DLC films highly depend on the ratio of the sp^3 to sp^2 and hydrogen content in the film which ultimately depend on the deposition technique as well as the deposition parameters. DLC growth can be done by both PVD (physical vapor deposition) and CVD (chemical vapor deposition) techniques. Deposition of DLC primarily needs two main entities:

- 1) A carbon source.
- 2) An energy source in order to create excited carbon species.

The deposition of DLC can be achieved through any one of the following processes:

- i) Sputtering which involves momentum transfer with sputtered species during collision.
- ii) Ion assisted depositions which involves bombardment with energetic species.
- iii) Laser ablation or electric arc discharge which involves electrostatic acceleration of carbon ions or energy transfer.

In these processes, the kinetic energies of the produced carbon species exist in the range 2.5-25 eV which is optimum for the deposition of DLC films with significant amount

of sp^3 content. The carbon species produced by thermal evaporation process possess 0.025 eV which is not sufficient to transfer $2s$ electron to the $2p$ orbital for the formation of the sp^3 hybridized carbon bond.²⁴ Hence, DC/RF Magnetron Sputtering (MS), Cathodic Arc Deposition, PLD, Plasma Enhanced Chemical Vapor Deposition (PECVD), Ion Beam Deposition (IBD), Filtered Vacuum Cathodic Arc Deposition (FVCA), Plasma Immersion Ion Implantation Deposition (PIIID) and Mass Selected Ion Beam Deposition (MSIB) can produce DLC films with greater sp^3 fraction.²⁵⁻²⁹ From the above mentioned deposition techniques, only the PLD, FVCA and MSIB can yield un-hydrogenated DLC films with greater sp^3 fractions.³⁰

PLD is a PVD process, carried out in a vacuum system. In this process a pulsed laser is focused on to a target material to be deposited. Each laser pulse with sufficient energy vaporizes a small amount of the target material forming the plasma plume. The ablation plume, consisting of ablated material expands mostly in forward direction irrespective of the angle of incidence of the laser beam and provides the material flux for film growth. The deposition of un-hydrogenated DLC film by PLD takes place by laser ablation of a high purity graphite target. The PLD technique can be optimized in order to obtain un-hydrogenated DLC film with highest C-C sp^3 contents. The other advantages of PLD over other techniques are:

- (1) DLC with high sp^3 content can be synthesized at room temperature.
- (2) Easy to control sp^3 to sp^2 ratio in order to tailor the properties of DLC for desired applications.
- (3) Control of film thickness and formation of complicated multilayers with different metal components without breaking the vacuum are possible in PLD.

(4) Feasibility of maintaining stoichiometry of target material in the film.

Thus, PLD enhances the quality of the DLC film with negligible impurity. The properties of un-hydrogenated DLC films grown by PLD were greatly influenced by the deposition parameters such as: laser fluence, substrate temperature, background environment and substrate biasing.^{14, 15}

1.4. Growth mechanism of DLC by PLD

PLD is a versatile technique where laser ablation of a graphite target produces energetic plasma species, which plays a vital role in the synthesis of un-hydrogenated film. The PLD process mainly involves the laser and target interaction which includes several systematic processes such as absorption of photon energy, target surface melting owing to the formation of Knudsen layer, vaporization, plasma emission and plasma heating by inverse Bremsstrahlung absorption and finally, expansion of the plume due to the pressure differences. The basic growth mechanism of DLC with significant sp^3 content is understood by the sub-plantation model proposed by Robertson.³¹

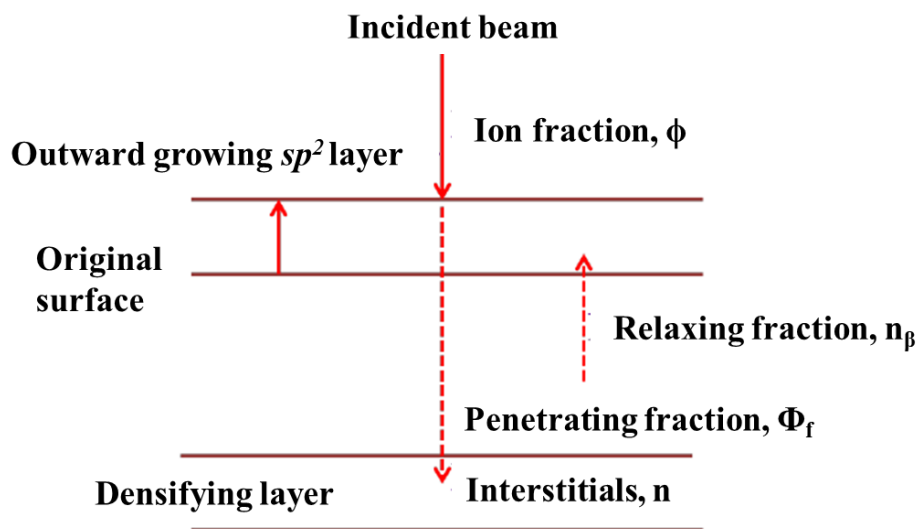


Figure. 1.2. Schematic diagram of Sub-plantation model.

The sub-plantation model provided in **Figure 1.2.** depicts the mechanism involved in the formation of sp^3 bond for the growth of DLC. From the incoming plasma species a fraction of ion having sufficient energy pass through the surface layer to occupy a subsurface interstitial site, which leads the film densification with the formation of sp^3 bonds. The fraction of ion having very high energy dissipates this excess energy in the matrix and leads to the sp^2 clustering due to stress relaxation. This phenomenon is known as thermal spike.

The property of DLC film deposited by pulsed laser deposition basically depends on the deposition parameters, as the deposition condition influences the dominating factors like kinetic energy of the carbon particles and its charge state in the plasma plume.³² The versatility of PLD lies behind the ease with which the physical properties of laser plasma are tailored by the optimization of process parameters such as laser pulse energy, pulse width, wavelength and repetition rate. Optimization of these parameters helps in tailoring the hybridization state of carbon atoms to enhance the tribological and mechanical properties.³³⁻³⁵ The effect of laser power density on the electrical property of the DLC film was studied by Levoska *et. al.*³⁶ It was observed that with increase in the laser power density the optical energy gap of the DLC films increased. Peeler and Murray investigated the influence of laser wavelength on the graphite ablation for $\lambda = 1064, 532, 248$ and 193 nm.³⁷ It was observed that the sp^3 content of the film deposited with excimer lasers increases with laser wavelength. The kinetic energy of the carbon species plays a vital role in determining the sp^3 content in the DLC film. Germain *et. al.* studied the plasma dynamics and observed that at low laser fluence, low K.E carbon dimer (C_2), trimers (C_3) and higher carbon clusters (C_n) are formed.³⁸ But at higher laser intensities, only C^+ ions are formed which is responsible for the formation of the sp^3 bond in DLC film. Yamagata *et. al.* suggested that a K.E of 90 eV

produces maximum fraction of sp^3 bonded carbon.³⁹ Beyond this upper limit graphitic phase formation takes place due to surface heating.

1.5. Limitations for DLC growth by PLD with possible solutions

In this section, two limitations for DLC growth by PLD will be discussed. First limitation is the presence of particulates in carbon plumes.⁴⁰ Target fragmentation and fragment ejection due to local heating and melting of the target lead to ~ 0.1 to ~ 10 μm graphitic micro-particles (particulates) embedment within the DLC film. As a result, the mechanical, optical, and electronic properties of DLC film are substantially degraded by the presence of these particulates. In particular, this process is highly detrimental in low melting target materials with low thermal conductivities under long laser wavelengths and high laser intensities.⁴¹

Both passive and active techniques can be adopted in order to minimize the size and number density of particulates produced during the laser ablation process. The passive techniques for minimizing particulate generation are: (a) using short-wavelength (e.g., ultraviolet) lasers and (b) pre-deposition conditioning of the target (e.g., few shots laser scanning). The reduction of particulates by using short-wavelength lasers is due to enhanced ablation through photon sputtering and less target surface overheating. In addition, target conditioning includes maintaining a smooth surface by laser beam scanning over the target surface. Similarly, active methods for reduction of particulate number density include plume filtration and ablation of novel target. The particulates from carbon plume can be filtered mechanically with the help of a rotating vane.⁴² The other methods like, off-axis ablation, two laser depositions, laser beam scanning, and target rotation can also be used to prevent target overheating.^{43, 44}

The second limitation associated with DLC is the high internal compressive stress (~ 10 GPa) developed during deposition, which prevents the growth of thicker DLC films (maximum film thickness to $0.1\text{--}0.2\text{ }\mu\text{m}$.).⁴⁵ The delamination of the DLC film occurs when the internal stress exceeds a certain critical value. The origin of the internal stress in DLC films has been explained by several theories. Bewilogua *et. al.* suggested that an ion cascade leads to a shock wave, which triggers the creation of sp^3 hybridized carbon atoms and in turn develops stress in DLC film.⁴⁶ Whereas, this model failed to explain the stress development process at higher ion energies. Another model proposed that the production of compressive stress due to ion bombardment results in relaxation of sp^3 hybridized bonds and transition from sp^2 to sp^3 hybridized bonds at a critical value of compressive stress (~ 4 GPa).^{47, 48}

The residual stress developed in thin films can be divided into three groups, such as:

- **Thermal stress:** This arises due to the dissimilar thermal expansion coefficient of the substrate and film.
- **Extrinsic stress:** This is induced by external factors like interactions between the deposited film and environment.
- **Intrinsic stress:** This type of stress arises during the deposition and the magnitude of this stress depends on various deposition parameters. Further, intrinsic stress is categorized as tensile and compressive intrinsic stress. Tensile intrinsic stress arises in the films due to non-energetic particles ($0.1\text{--}1\text{ eV}$), whereas compressive intrinsic stress develops in the film from energetic particles ($1\text{--}25\text{ eV}$).

Since DLC films are produced from higher energetic carbon species ($> 25\text{ eV}$), which develops mainly compressive stress in the film. The magnitude of this compressive stress

depends on total kinetic energy of ablated species impinging on the surface of the film resulting in the condensation and incorporation of the atom in the film.⁴⁹ This type of residual stress in DLC films results delamination/adhesion failures of the film from the substrate.

The residual compressive stress can be reduced in the DLC films by following methods:

- (i) Varying the deposition parameter.
- (ii) Doping metallic or non-metallic elements.
- (iii) Introducing metallic interlayer between the film and the substrate.

Mosaner *et al.* reported synthesis of DLC films of thickness $> 1 \mu\text{m}$ with reduced residual compressive stress ($\sim 2 \text{ GPa}$) by appropriate steps of thermal annealing upto 300°C which leads to chemical bond relaxation.⁵⁰ Bonelli *et al.* were able to synthesize DLC films with compressive stress $< 2 \text{ GPa}$, by using PLD technique with various laser pulse energies under vacuum.⁵¹ Arjunan *et al.* reported delamination free, micron thick DLC films with residual stress values of 2 GPa by MCPLD (Multi Cycle Pulsed Laser Deposition) as compared to 9 GPa in films deposited by conventional or Single Cycle Pulsed Laser Deposition (SCPLD).⁵² It is reported that non-metal (N, Si) doping resulted in DLC films with enhanced adhesion strength by increasing sp^2 bonds through subsequent relaxation of residual stress in the films.⁵³ They reported that the effect of concentration of nitrogen and Si doping in DLC film show improved adhesion and reduced stress while the mechanical property degraded. In addition, N-doping enhances the tribological performance of DLC films because the N incorporation in DLC films induces the graphitization of the films and brings down the friction of the films via the enhanced lubricating effect.⁵⁴ Gayathri *et al.* reported the influence of transition metal (Ag, Ti, and Ni) doping on the tribological

properties of pulsed laser deposited DLC films with the reduction of internal compressive stress.⁵⁵ They observed formation of nano-clusters and TiC phases in DLC/TM films. DLC film doped with nano-crystalline Ag exhibited enhanced tribological behavior due to the formation of copious amount of sp^2 lubricant phase. However, DLC film doped with Ni and Ti showed high coefficient of friction due to the presence of hard TiC and sp^3 phase in the DLC/Ti and DLC/Ni films, respectively. Menegazzo *et. al.* investigated the electrochemical properties of noble metal(Pt, Au)-DLC nano-composite thin films. They reported delamination free noble metal-DLC nano-composite thin films with enhanced conductivity compared to their metal-free counterparts.⁵⁶ Gayathri *et. al.* reported the tribological and scratch resistance properties of Diamond-Like Carbon (DLC) coatings with transition metal interlayers (TM = Cr, Ag, Ti, and Ni) synthesized by PLD.⁵⁷ They observed remarkably higher scratch resistance of DLC films deposited with Ni and Ti transition metal interlayer than Ag and Ni interlayers.

The metal or non-metal should be selected as dopant or interlayer in order to modify the property of the DLC film for desired applications. One should select the type of substrate before choosing the dopant or interlayer to enhance the adhesion of DLC film to substrate without affecting the mechanical and tribological properties, as addition of metals in DLC reduces its hardness significantly. Therefore, it is necessary to design the film structure to attain enhanced adhesion without affecting the mechanical properties of the DLC film. There are various types of coating architectures through which hardness and adhesion of the film can be improved. Hence, apart from the choice of metals, the film architecture also plays a vital role in deciding the overall property of the DLC film which is discussed in the following

paragraphs. **Figure 1.3.** shows schematic of various film architectures such as:- nano-composite film, bilayer film, multilayer film and functionally gradient film.

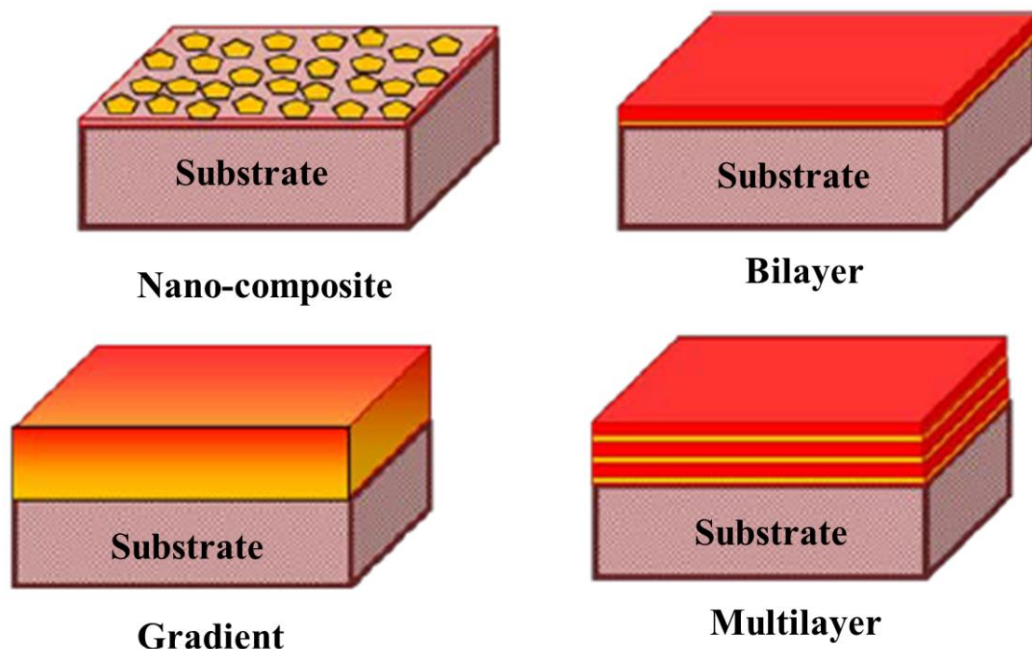


Figure 1.3. Schematic diagram of various film architectures.

A brief account is presented below.

- **Nano-composite film:** A Nano-composite film consists of a host material (or matrix) with another material uniformly distributed in it with a characteristic length scale of 1-100 nm. The yield strength, hardness, toughness increases with decrease in the grain size following the Hall-Petch relation.^{58, 59} The decrease in grain size resists dislocation propagation and enhances the hardness, whereas easy grain boundary sliding enhances the toughness. In this regard, a proper microstructure design is necessary to inhibit the grain boundary sliding, which can be achieved by enhancing the complexity and strength of grain boundaries in any nano-composite film.

- **Bilayer and multilayer films:** A larger lattice mismatch between the film and the substrate needs a sandwiched interlayer with intermediate lattice which bonds the film to the substrate.^{9, 57} Multilayered coatings are different from sandwiched layers (bilayer) by their periodically repeated lamellae of two or more materials. The thickness of the lamella varies from few nanometer to few tens of nanometer and these structure hinders the dislocation glide and crack propagation. The major drawback of this architecture is difficulty in uniform coating of a 3-D object.
- **Functionally Graded films:** It is a composite material synthesized by varying the composition and microstructure from one material to another material with a specific gradient.^{25, 60} The functionally graded design enhances the load bearing capability by providing easy transitions in mechanical properties from those of the hard coating to those of the soft and malleable substrate. This design helps in distributing the contact load over large areas which significantly lowers the stress at coating and film interface thereby increases the adhesion strength but the hardness of the film decreases.

Different film architectures have been adopted in order to enhance the mechanical and tribological properties of DLC using complicated hybrid techniques. Voevodin *et. al.* has used hybrid technique by combining magnetron sputtering and PLD to deposit functionally gradient DLC film to enhance hardness (up to 60 GPa) and adhesion strength (50 N).⁶⁰ From the literature survey it is clear that hybrid deposition techniques are mainly used to form multicomponent complex film structure to achieve better adhesion strength and mechanical properties. But these are economically costlier, tedious and time consuming methods. Therefore, simple film architecture by a simple and economic deposition technique is

required to enhance the hardness and adhesion strength of the material along with reduced internal stress. The laser ablation of a multicomponent target using PLD technique is such a method, which meets all the practical demands.^{55, 57}

1.6. Motivation and Research objectives

In last few decades, DLC has emerged as a major component of Chameleon nano-composites for diverse environmental tribology applications.¹⁻⁵ In addition, gold with amorphous yttrium stabilized zirconia (YSZ) in the form of binary nano-composite (YSZ-Au) hard coating is used as a component of YSZ-Au-MoS₂-DLC nano-composite.^{4, 5} This is a tribological coating with chameleon-like surface adaptive behavior for high temperature adaptive lubrication and contact thermal management. The high hardness value of YSZ-Au nano-composite is ~15 GPa with 20 atomic percent (at. %) of Au incorporation.⁵ The low value of hardness with high atomic % of Au in YSZ-Au binary nano-composite hard coating demands another binary nano-composite hard coating like DLC-Au, which can provide higher hardness value with low Au at.%. Although synthesis of un-hydrogenated DLC-Au nano-composite is readily available in literature,⁵⁶ but its extensive tribological study is rare. Not many studies are found in the areas of tuning the tribological properties of un-hydrogenated DLC-Au nano-composite with Au at.%. PLD is the versatile technique for synthesis of un-hydrogenated DLC-Au nano-composite films from graphite and gold multicomponent target. The PLD parameters need to be optimized to achieve superior tribological properties of DLC-Au nano-composite with optimum Au at.% content. Whereas the issue related to particulate generation by PLD should be investigated prior to the investigation on DLC-Au nano-composite films. Thus, the present study is mainly focused on two issues:

- First issue is concerned with the investigation of vibrational properties of particulate laden DLC films and the influence of particulates on morphology, composition, surface energy, CA, and mechanical properties of DLC films.⁶¹⁻⁶³
- Second issue is concerned with the growth of DLC-Au nano-composites with optimum gold content/ cluster size for superior mechanical and tribological applications.^{64, 65}

In this study, for the first issue particulate laden DLC films were grown by PLD at four different laser pulse energies (100-400 mJ) of an Nd: YAG laser. The morphological studies of particulate laden DLC films were carried out by AFM and FESEM.^{61, 62} Visible-Raman, visible Raman I_D/I_G mapping and UV-Raman study on flat surface and particulate regions of DLC films were employed separately to observe the evolution of vibrational and structural properties of particulates with laser pulse energy.⁶¹⁻⁶³ The sp^3/sp^2 content of DLC films were determined by XPS study.⁶¹ The effect of particulates on surface energy, CA, and mechanical property of DLC films were studied using contact angle measurement, AFAM, and nano-indentation study, respectively.^{61, 63}

For the second issue, DLC- Au nano-composites were grown at three different laser indexing angles (10° , 20° , and 30°) of a pulsed KRF laser on a graphite and gold foil composite target.^{64, 65} Morphological studies of DLC-Au nano-composite were carried out by AFM and FESEM, XRD and TEM for Au phase confirmation and related structural information in DLC-Au nano-composite.⁶⁵ The Au at.%, sp^3 content, and sp^2 content were determined from XPS and EDS studies.^{64, 65} The vibrational properties of DLC-Au nano-composites were studied by EELS and Raman studies.⁶⁴ The mechanical and tribological property of DLC-Au nano-composite films were investigated using nano indentation and

tribology techniques.⁶⁵ The structural transition study on tribo-track and ball scar were carried out by visible-Raman technique.⁶⁵

Finally, in particulate laden DLC films; the vibrational evolutions of particulates were correlated with the evolution of composition, CA, surface energy and mechanical property of DLC film with laser pulse energies. Similarly, in DLC-Au nano-composites the Au content/cluster size was optimized for superior mechanical and tribological property.

CHAPTER 2

Experimental Techniques

“A Theory can be proved by experiment; but no path leads from experiment to the birth of a theory”

Albert Einstein

Growth, characterization and application of thin film materials involve studies and investigations by several compatible experimental techniques. This chapter presents a brief report in two parts on experimental techniques used in this thesis work. The first part contains an extensive description of the experimental facility developed in the specimen synthesis lab to pursue research on PLD grown particulate laden DLC films and DLC-Au nano-composites. The second part describes the basic principle with experimental parameters of all the characterization methods that have been employed to characterize the specimens in the present work.

2.1. Introduction

The basic operation principles and details of the nanosecond pulsed Nd: YAG laser and KrF excimer laser are discussed in the following sections. This section also outlines the detailed PLD set up including laser, UHV Chamber and beam steering optics used for synthesis of DLC and DLC-Au nano-composite thin films from high purity graphite and graphite-Au composite targets, respectively. Growth rate is determined from thickness measurement of DLC films grown for a determined deposition time, using surface profilometer. The

morphological study is carried out by FESEM and AFM. Raman spectroscopy is extensively used for vibrational study of c-c bonding in particulate laden DLC films and DLC-Au nano-composites. XRD and TEM are employed for structural characterizations of DLC-Au films. Elemental analysis is carried out by XPS, EDS and EELS. Surface elasticity distribution of particulate laden DLC films are analyzed using point spectroscopy technique of Atomic Force Acoustic Microscopy (AFAM). Surface energy of particulate laden DLC films is determined using Contact angle measurement. Mechanical properties of particulate laden DLC and DLC-Au nano-composites are determined using Nano Indentation technique. Tribological response of DLC-Au nano-composites is determined using a micro-Tribometer.

2.2. PLD Growth techniques

Pulsed laser deposition (PLD) is a physical vapor deposition (PVD) process for thin film synthesis, which is performed in an ultra-high vacuum (UHV) chamber using a target and an outside laser source. The simplicity in implementation of this technique has largely upgraded its applicability and acceptance in thin-film research. During the last 20 years, PLD has emerged as one of the most prevalent techniques for depositing thin films of exciting novel materials. The inherent versatility in addition to its flexibility and speed of coating (metals, alloys, semiconductors, insulators, polymers and even biomaterials) over any substrate, convert it into an adorable technique over other traditional methods. In the late 1986, the PLD technique was resumed from the previous demonstration of the invention of high power lasers during mid-1960 with the advent of superconducting material.⁶⁶ Nowadays, this technique is being adapted to wide range of material synthesis starting from mono atomic layer to quasi-bulk crystalline materials of thicknesses more than 100 nm. It is also successfully used to synthesize several types of multicomponent thin films with very high

quality and stoichiometric composition.⁶⁷ This appears from the non-equilibrium nature of the ablation process itself due to absorption of high laser pulse energy by a small volume of material. For a particular laser wavelength, the laser pulse with low laser fluence and/or low absorption, would simply heat the target, and eject material due to thermal evaporation of the target. In this case, the vapor pressure of the constituents decides the evaporative flux from a multicomponent target. On increasing the laser fluence, an ablation threshold is reached where absorbed laser pulse energy is higher than that needed for material evaporation. The ablation threshold depends on the absorption coefficient of the target material and thus is wavelength dependent. Therefore, the selection of an appropriate laser wavelength is an essential criterion for the ablation process. The ablated volume of the non-equilibrium excitation is high at a temperature well above the required temperature for evaporation, this is necessary for efficient ablation of the target material. Basically this demands a short duration laser pulse with high energy density, which should be absorbed efficiently by the target material. Hence, lasers with shorter wavelengths i.e. operating in the ultraviolet range are suitable for ceramic targets, which can be achieved by excimer lasers or frequency-tripled or quadrupled Nd: YAG solid-state lasers.⁶⁸

In PLD, the kinetic energies of ions and neutral species in the ablation plume can vary in a range, starting from few tenths to several hundred electron volts. The kinetic energy of ablated species is largely dependent on laser pulse energy and gas-phase collisions in the plasma plume. These energies are sufficient for defect formation, which modify the specimens with respect to its stress state. The most common consequence of allowing deposition from a non- equilibrium energetic plume is the introduction of compressive stress. This compressive stress originates from the subsurface damage caused by the impinging

energetic species.⁶⁹ In this case; the energetic depositing atoms displace subsurface atoms to interstitial sites in the film. The compressive stress produced in this process is of the order of gigapascals. This compressive stress is sufficient enough to cause bowing of the thin substrates. However, some of the limitations such as particulates formation, incongruent ablation and deposition over large areas could be minimized by incorporating some modifications to the traditional PLD method. The plume substrate position is so adjusted to obtain uniform film thickness over large areas. Many methods have been deployed to address this drawback. One of the most straight forward approaches is to couple substrate rotation with rastering of the ablation beam over a large ablation target. While doing this one must be careful about the reduction in plume energies and variation in plume stoichiometry that occurs as one move to the edge of the plume region. Computational approaches normally aid in preserving plume configuration by adjustment of process variable.⁷⁰

The main limitation with PLD is the removal of micron size particles from target surface during ablation. It is a frequently encountered problem where the laser pulse penetrates deeply into the target material. These particulates when deposited onto the specimen, adversely affect the mechanical and friction behavior of the specimen surface. Nowadays, in-depth studies on particulates at Nano scale have fascinated the material science community.⁶¹ The usage of high density targets reduces the formation of particulates and using low wavelength lasers which are easily absorbed by the target also helps in minimizing the ejection of large particulates. Other techniques include usage of velocity filters, off-axis laser deposition and line of sight masks to reduce the particulate formation. Cross beam methods are also adopted for mitigating particulate deposition from dusty plume. The

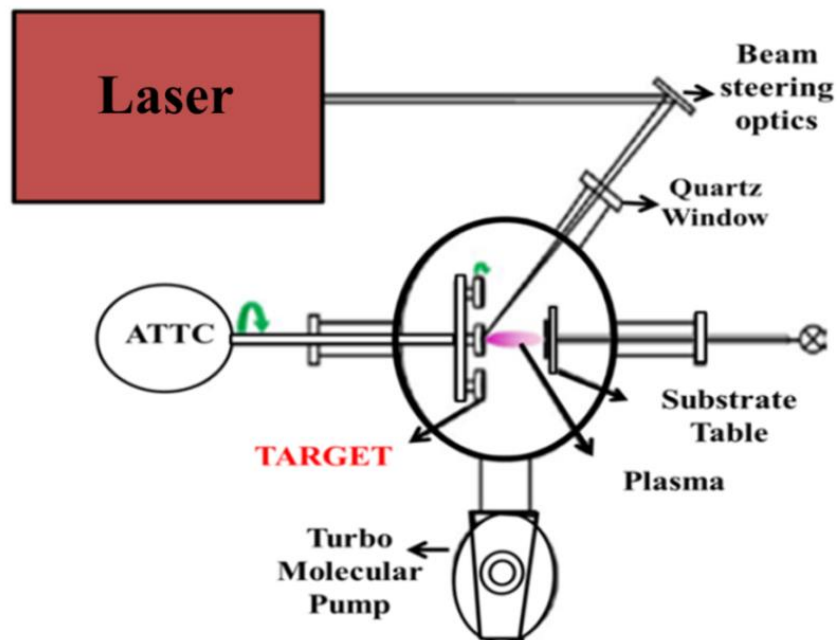


Figure 2.1. Schematic diagram of PLD set up.

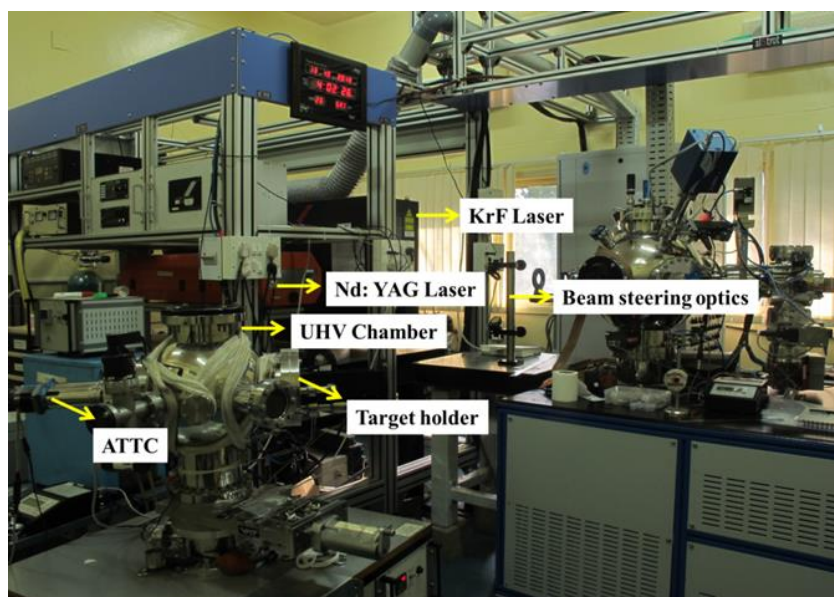


Figure 2.2. Photograph showing UHV deposition chamber with nanosecond pulsed Nd: YAG and KrF laser systems.

fundamental and experimental aspects of PLD process is discussed in this section. The schematic diagram of a typical PLD set up is shown in **Figure 2.1.**, in which a pulsed laser is focused onto a target of the material to be deposited on a substrate in an UHV chamber.

The major components of this system are (i) Laser, (ii) UHV chamber and (iii) Beam steering optics with associated vacuum pumping, target carousel and substrate heating system. **Figure 2.2.** shows the experimental set-up of the PLD system used to deposit DLC films and DLC-Au nano-composites in the present thesis. Each laser pulse with sufficient laser power density ablates certain quantity of the material producing the plasma plume. The ablated material from the target is ejected in a highly forward-directed plume.

2.2.1. LASER

Conventionally, a laser is a special type of light source that amplifies light and produces a highly directional, high-intensity beam that most often has a well-defined frequency or wavelength. The word **LASER** stands for **L**ight **A**mplification by **S**timulated **E**mission of **R**adiation. The laser makes use of processes that amplify light signals generated by other means. These processes include:-

- A) Stimulated emission, a natural effect that was deduced by considerations relating to thermodynamic equilibrium, and
- B) Optical feedback (present in most lasers) that is commonly contributed by mirrors.

Thus, in its elementary form, a laser is composed of a gain or amplifying medium (where stimulated emission takes place), and a set of mirrors to feed the light back into the amplifier for gradual growth of the developing beam.⁷¹

2.2.1.1. Nd: YAG laser

The Nd: YAG laser is a four level energy system based optically pumped solid-state laser. The four level energy systems are denoted by E_1 to E_4 as shown in **Figure 2.3.**⁷² The Neodymium (Nd) ions, doped in the Yttrium-Aluminium-Garnet (YAG) matrix, have two absorption bands (E_3 & E_4) and are excited by optical pumping using flash lamps. From these excited energy levels, the Neodymium ions move into the upper laser level (E_3) by a non-radiative transition. Then stimulated emission occurs from the upper laser level to the lower laser level (E_3 to E_2) with the wavelengths of the emitted photons being around 1064 nm, in the IR region. Again, from the lower laser level, a non-radiative transition occurs to the ground level denoted by E_1 . Nd: YAG lasers are capable of producing very high-power emissions and they are used for several applications, ranging from medical, materials processing to military.

Nd: YAG lasers operate in both pulsed and continuous wave modes. Pulsed Nd: YAG lasers are typically operated in the Q-switching mode, which is nothing but an optical switch which is inserted in the laser cavity waiting for a maximum population inversion in the Neodymium ions before it opens. Then the light wave can run through the cavity, depopulating the excited laser medium at maximum population inversion. In the Q-switched mode, maximum output powers of 20 MW with pulse durations of less than 10 ns are achieved.

In this study, an Nd: YAG laser (M/s. Quanta Systems, Italy) operating at 1064 nm wavelength with a maximum pulse energy of 900 mJ, pulse width of 5 ns and repetition rate of 10 Hz was used for synthesis of particulate laden DLC films. The laser beam, having 8 mm diameter at the output port, is steered into the PLD chamber using anti-reflection coated

BK7 mirrors with optical mounts and focused using a 3-mirrored telescope having focal length of approximately 50 cm. Finally, the beam is focused to a circular spot having ~ 1.0 mm diameter.

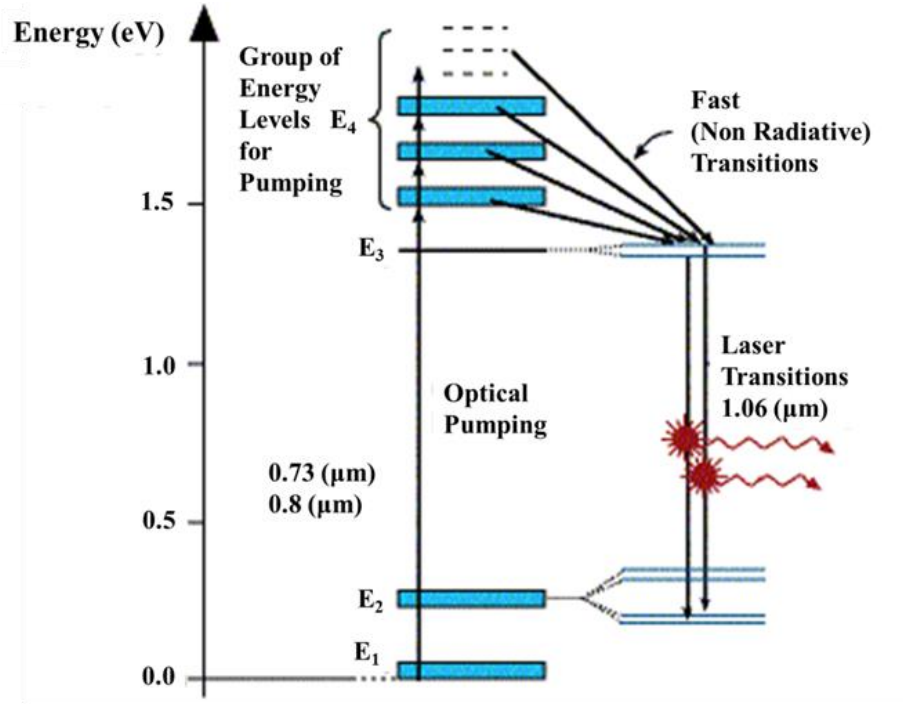


Figure 2.3. Energy level diagram of a Nd: YAG laser.⁷²

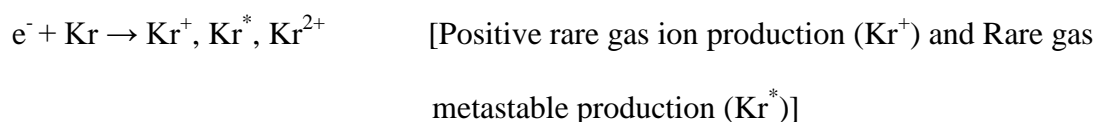
Particulate laden DLC films were grown on silicon (111) substrates of $10 \times 10 \text{ mm}^2$ dimensions by pulsed laser ablation of a high pure 2" diameter pyrolytic graphite target (with purity close to 99.99%) in the UHV chamber using the above mentioned Nd: YAG laser. The Si substrates were cleaned properly to remove impurities from the surfaces using lukewarm soap solution, deionised water, acetone and ethyl alcohol, successively in an ultrasonicator bath for 10 minutes per each solvent. The cleaned Si substrates were loaded into the UHV chamber with 40 mm substrate to target distance. The deposition process was carried out at a base pressure and deposition pressure of 4.5×10^{-6} mbar and 6×10^{-6} mbar, respectively. The laser ablation was carried out with 5 ns pulse width, 10 Hz repetition rate, 0.7 mm^2 laser spot

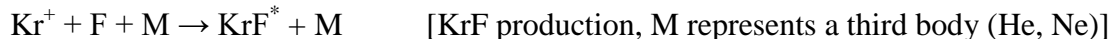
area and varying the laser pulse energy in a range 100-400 mJ at an interval of 100 mJ for 10,000 shots. The laser fluencies corresponding to the laser pulse energies 100, 200, 300 and 400 mJ are as 2.85×10^8 , 5.71×10^8 , 8.57×10^8 and 1.14×10^9 $\text{W} \times \text{cm}^{-2}$, respectively. According to the laser pulse energies, the films were labeled as DLC-1, DLC-2, DLC-3, and DLC-4 specimens, respectively. The graphite target was subjected to rotate continuously in order to expose fresh surface and to check pinhole formation. Four set of specimens were synthesized under identical condition for statistical analysis.

2.2.1.2. KRF laser

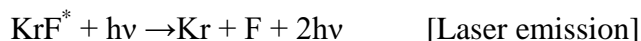
The excimer lasers are capable of producing UV laser light and have long life. The term Excimer stands for a molecular complex of two excited atoms which is stable only in an electronically excited state. These lasers are pulsed lasers with an ultraviolet wavelength output. Several excimer lasers with desired wavelengths are ArF ($\lambda=193$ nm), KrF ($\lambda=248$ nm), KrCl ($\lambda=222$ nm), XeCl ($\lambda=308$ nm) and XeF ($\lambda=351$ nm). Although KrCl and ArF lasers are having lower λ than that of the KrF lasers, still KrF lasers are the most commonly used lasers for deposition process, due to its highest gain.⁷³ The formation of Excimer molecules happen in the mixture of component gases and the external energy is pumped in to the gas through electrical stimulation (electric discharge excitation). As a result, the electronically excited species and ions react, leading to the formation of Excimer molecules. These excited molecules are the source of laser. The processes involved in producing Excimer molecules for suitable laser action are as follows:

Pumping:





Stimulated emission:



The excited KrF^* molecules will decay into Kr and F via spontaneous emission of a photon. Thus the components Kr and F are again available for another excitation cycle.⁷⁴ The important laser parameters that affect the film quality and microstructure are spot size, beam homogeneity, laser pulse energy and repetition rate.

In this study, a KrF excimer Laser (COMPex Pro 205, M/s. Coherent, Germany) operating at 248 nm wavelength with maximum pulse energy of 700 mJ, pulse width of 25 ns and repetition rate of 1-50 Hz was used for synthesis of DLC-Au nano-composites. The laser beam, having an area of $24 \times 10 \text{ mm}^2$ at the output port, is steered into the PLD chamber using UV enhanced aluminium mirrors with optical mounts and focused using a 3-mirrored telescope having focal length of approximately 50 cm. The beam is focused to a rectangular spot having $2 \times 5 \text{ mm}^2$ size.

Un-hydrogenated DLC-Au nano-composite films on silicon (100) substrates ($10 \times 10 \text{ mm}^2$) were grown at room temperature under high vacuum ($5 \times 10^{-6} \text{ mbar}$) by PLD technique using the KrF Excimer Laser at 300 mJ laser pulse energy for 10,000 shots. The growth of DLC and DLC-Au films were performed by the ablation of a 2" diameter pure pyrolytic graphite (purity of 99.99 %) and pyrolytic graphite-Au composite targets, respectively. The graphite-Au composite target contains a 1" diameter and 2 mm thick gold foil (purity of 99.99 %) off-centrally placed on the pure pyrolytic graphite target as shown in

Figure 2.4. The laser beam was rastered (10° - 30°) on the rotating pure graphite target for DLC films, while for DLC-Au films was fixed at indexing angle (10° , 20° , 30°) on the rotating graphite-Au composite target. The laser beam was incident on the rotating targets (with 10 rpm) through the beam steering optics. The fractions of the time (or laser shots) on Au segment to the graphite segment for indexing angles 10° , 20° and 30° are 7:5, 1:2 and 5:13, respectively.

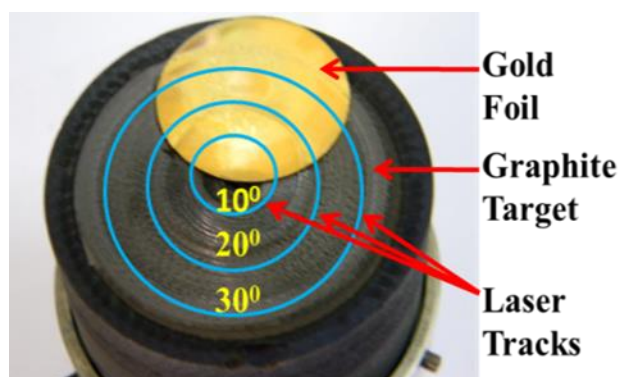


Figure 2.4. Graphite-Au Target arrangement

The deposition parameters, such as base pressure (3×10^{-6} mbar), deposition pressure (5×10^{-6} mbar), target to substrate distance (5 cm), substrate temperature (RT), laser pulse energy (300 mJ), no. of shots (10,000) and repetition rate (10 Hz) were kept constant throughout the deposition process. The specimens were labeled as DLC– Au: 12%, DLC– Au: 7.3% and DLC– Au: 4.7% depending on the gold contents.

2.2.2. UHV Chamber

The ultra-high vacuum deposition chamber is a bake able stainless steel spherical chamber (M/s. Excel Instruments, India) attached to a turbo molecular pumping unit (550 l/sec, M/s. Leybold, Germany) and backed by a rotary vane pump (330 l/sec, M/s. Leybold, Germany). The turbo molecular pumping system arrangement ensures an oil free vacuum environment

inside the chamber. This pumping system also helps removal of inert carrier gases with high pumping speed. It operates at a base pressure of $\sim 2 \times 10^{-7}$ mbar. This ultra-high vacuum environment ensures low background pressure with minimal contamination and better reproducibility. This chamber houses a multitarget (6 nos.) carousel with micro-processor based automatic target carousel controller (ATCC) and substrate heating assemblies. Apart from gadgets such as Pirani and Penning gauges for vacuum measurement, the laser port, target, and substrate assembly are configured as shown in **Figure 2.1.** such that the laser falls on the surface of the target at an oblique incidence of 45° to provide maximum ablation yield. Substrates are positioned just in front of the target.

2.2.3. Target holder and automated target carousel controller (ATCC)

The target holder is a six-target turret mounted on a flange with a DC motor and a 0 to 360° graduated rotatable positioner as shown in **Figure 2.5.** The DC motor helps the rotation of the targets about their own axis. It also rotates the targets all together about a central axis. Initially the targets (upto a maximum of six numbers) can be fixed in the target holder and indexed through the calibrated rotatable positioner.

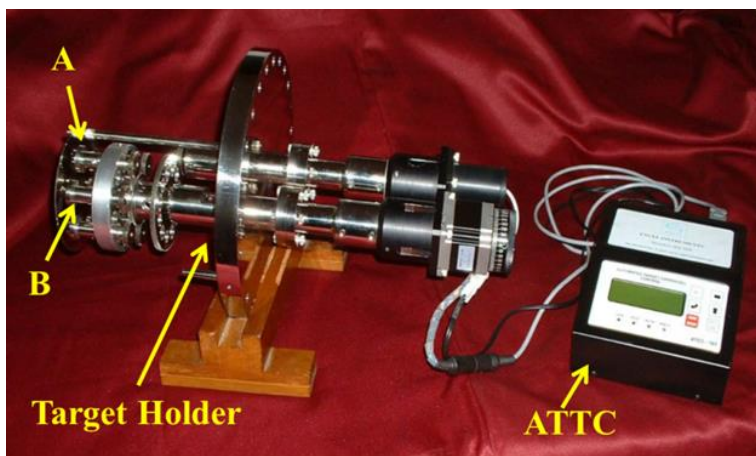


Figure 2.5. Photograph of target assembly and microprocessor based automatic target carousel controller (ATCC).

The desired target can be brought to the focus of laser beam by rotating the targets about the central axis. Rotation of a target about its own axis prevents development of deep craters on the target surface during laser ablation and exposes a fresh target surface for ablation. The target holder also houses a target contamination shield to prevent the contamination of other targets due to the plume generated during the ablation of one target. The automated target carousel controller (ATCC) is a microprocessor based controller, which controls the motion of DC motor.

This target assembly supports growth of multilayers by carrying out the following functions:

- (i) Brings the desired target (A) to the focus of laser beam
- (ii) Rotates the target about its own axis with uniform speed to prevent crater formation.
- (iii) Exposes for predetermined number of shots.
- (iv) Pauses the laser during target changeover and brings another target (B) to laser focus.
- (v) Repeats the procedure by a preset number of times that helps in growing multilayers of A and B.

2.2.4. BEAM STEERING OPTICS

The beam steering optics assembly (**Figure 2.6.**) steers the laser beam from the laser output into the UHV chamber. In this study two different types of beam steering optics assembly are used for two different lasers, respectively. These are given as follows:-

1. Anti-reflection coated BK7 mirrors with optical mounts for Nd: YAG Laser.
2. High-reflection (> 85%) coated UV enhanced aluminium mirrors with optical mounts for KrF Laser.

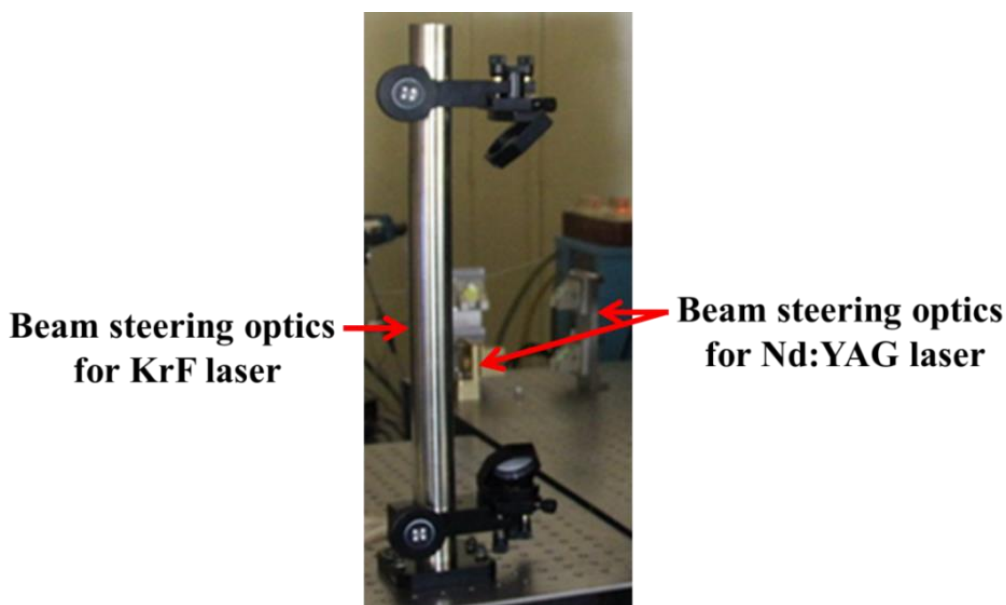


Figure 2.6. Photograph of beam steering optics with optical mount for Nd:YAG and KrF lasers.

2.2.5. Target

In this study, Diamond like carbon (DLC) films are synthesized for particulate investigation from the ablation of a 2” diameter pyrolytic graphite target (purity of 99.99 %) using the Nd:YAG laser and for DLC-Au nano-composite investigation the same graphite target with a 1” diameter and 2 mm thick gold foil (purity of 99.99 %) placed off-axis on it as a mask (**Figure 2.4.**) is ablated using the KrF laser for synthesis of DLC-Au nano-composites with various Au content.

2.3. Characterization Techniques

The characterization techniques used in this study are selectively chosen so as to follow the role of process parameters on the thickness, morphology, vibrational, structure and composition of the coatings with their mechanical and tribological properties. Raman spectroscopy is used as the primary non- destructive characterization tool in the present work

for qualitative determination of the sp^3 content and evaluation of residual stress modulation in the DLC and DLC-Au nano-composite films. In addition, Raman spectroscopy on the wear track and ball scar gives an insight to the understanding of the chemical changes that occur during tribology study.

2.3.1. Thickness Measurement

To measure the thickness of a film there are several thickness measurement methods such as weight gain, profilometer, spectroscopic reflectometer and ellipsometer etc. In the present work, thickness of both DLC and DLC-Au nano-composite films are measured using a stylus profiler (Dektak 6M, M/s. Veeco, USA).^{61, 65} A spherical diamond tip with diameter 12 μm was line scanned on the specimen surface with a predefined contact force at a speed of 15 $\mu\text{m/s}$ for a specified distance to obtain the thickness.

In the present work the normal load on the tip and scanning length used for each measurement are 10 mg and 2000 μm , respectively. The height position of the diamond stylus generates an analog signal which is converted into a digital signal and stored, analyzed and displayed. A particular region of the substrate is masked during deposition. Hence after deposition, this region is devoid of coating. The surface profilometer, while laterally scanning the sample picks up this surface variation (variation between the coated region and the region devoid of coating) and gives us the thickness value.

2.3.2. Raman Spectroscopy

Raman spectroscopy is a well-established and powerful non-destructive technique used for structural characterization. The Raman spectrum emerges from the interaction of low wavelength radiation with the electron that involve in the formation of chemical bonds. This interaction responds to the type, length and arrangement of bonds in a material which in turn

gives information about elemental chemical composition of the material.⁷⁵ In Raman spectroscopy, a monochromatic light beam is incident on the sample. This electromagnetic radiation interacts with the electron cloud involved in the bond formation and results in the loss or gain of energy. The light wave also causes the distorted electron assemblies to relax back by radiating the energy. This stored energy is emitted with a frequency identical to that of the source frequency. This radiation signal is called as the Rayleigh scattering and occupies central line in the spectrum. Though, a part of the incident energy is used to excite the vibrational modes in the sample, which results in weak side bands with frequencies smaller than the source beam. Such lines are termed as Raman lines and are known as Stokes lines. The separation between the Rayleigh and Raman line gives the measure of vibrational frequencies of the specimen and is generally plotted as intensity versus the difference in wavenumber between the incident beam and scattered beam. An inverse process also takes place where existing vibrations are annihilated by combining with the source beam which results in addition of energy to the source. These bands arise at greater frequencies and are known as anti-Stokes scattering. The two spectra lie on either side of the Rayleigh line. The schematic representation of the Raman scattering process is given in **Figure 2.7. (a)**. A general thumb rule is that molecules having polarizability are only Raman active.

The micro-Raman spectrometer (inVia, M/s. Renishaw, UK) extensively used for particulate laden DLC films in this thesis work is comprised of the following major components (**Figure 2.7. (b)**):

- **Excitation Source:** Lasers: Ar⁺ laser with 514.5 (Total power ~ 150 mW) and He-Cd Laser (UV - 325 nm, Power 10 mW).

- Sample illumination through Leica microscope equipped with 10×, 20×, 50× and 100× objective lenses.
- **Diffraction gratings:** 1800 grooves / mm for the monochromatization of scattered signal
- Thermoelectric cooled CCD for detecting the signal in backscattering configuration

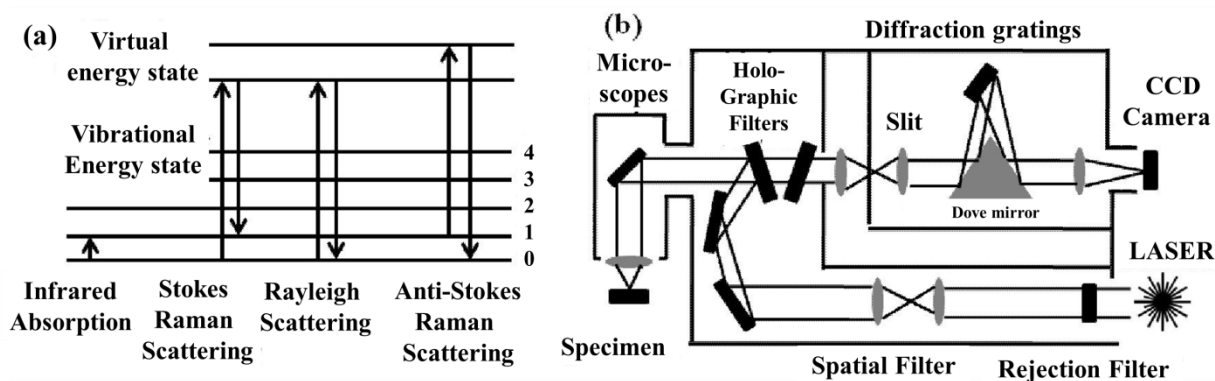


Figure 2.7. Schematic view of (a) scattering process in material with incident light, and (b) Raman spectrometer set up.

As far as DLC is concerned Raman spectroscopy is mainly used for structural characterization along with vibrational disorderness of carbon films. Raman spectra of a DLC film reveals a lot of information such as clustering size of the sp^2 phase, bond-length and bond-angle disorder, presence of sp^2 rings or chains, the sp^2/sp^3 ratio, the magnitude of the residual stress in the film and chemical composition on wear track. In the present study:-

- (1) Chemical structure on flat and particulate regions of the particulate laden DLC films were analyzed by using visible (514.5 nm) and uv (325 nm) laser Raman spectroscopy.⁶¹⁻⁶³
- (2) Visible (514.5 nm) Raman intensity mapping at a particular wavenumber was used to observe the influence of particulates on chemical structure of the flat region of particulate laden DLC films.⁶¹

(3) Micro-Raman spectroscopy (SR-500i-C-R, M/s. Andor, Russia) of wavelength 532 nm, was employed for detailed vibrational study in DLC-Au nano-composite films leading to residual stress analysis and on its tribo-track and ball scar for investigation of post tribological effect.⁶⁵

The laser power, throughout the thesis work, was kept below 3 mW to avoid sample heating and specimen decomposition. WIRE 3.2 software was utilized for fitting and extracting the data from Raman spectra. The Raman bands are fitted with Gaussian peaks after background subtraction.

2.3.3. X-ray Photoelectron Spectroscopy (XPS)

XPS is a surface sensitive quantitative technique to determine chemical composition of the material based on photoelectric effect. It is also known as Electron Spectroscopy for Chemical Analysis (ESCA) analyzes elemental composition, chemical bonding state and electronic state of the materials. The depth resolution of this technique is 0.5-5 nm. The basic principle is that the binding energy of an electron in a molecular orbital of the molecule will be affected by the nature of its chemical environment (chemical shift). XPS measurement is based on the photo-ionization and kinetic energy distribution analysis of the photoelectrons emitted from the sample which gives the information of relative elemental composition and bonding state prevailing in the surface of the sample. The specimen is focused with soft X-rays (0-1400 eV) under ultra-high vacuum. The X-ray photon is absorbed by an atom or molecule (initial state effects) leading to ejection of core shell electrons (final state effects). The kinetic energy of the photoelectrons is given by:-

$$K.E = h\nu - B.E - \phi \quad \dots\dots\dots (2.1)$$

where, K.E is the kinetic energy of the photoelectrons, $h\nu$ the energy of the incident photon, B.E is the binding energy of the electron and ϕ the work function of the material.

The photon absorption is fast and takes place within 10^{-16} s. If $h\nu$ is less than $B.E + \phi$, no photoemission process will be initiated. As the B.E decreases the K.E energy of the photoelectron increases. The intensity of the photoelectron emission is proportional to the intensity of photons. By analyzing the kinetic energies of the photoelectrons, the binding energy of the photoelectrons and corresponding energies of the electronic orbitals can be calculated.⁷⁶ Since the energies of various orbitals are characteristic of an element, one can identify the elements present in the material, based on the binding energies of the emitted photo electrons. Binding energy reflects the strength of interaction between the electrons and the positively charged nucleus and it contains information on the initial and final state of the atoms.

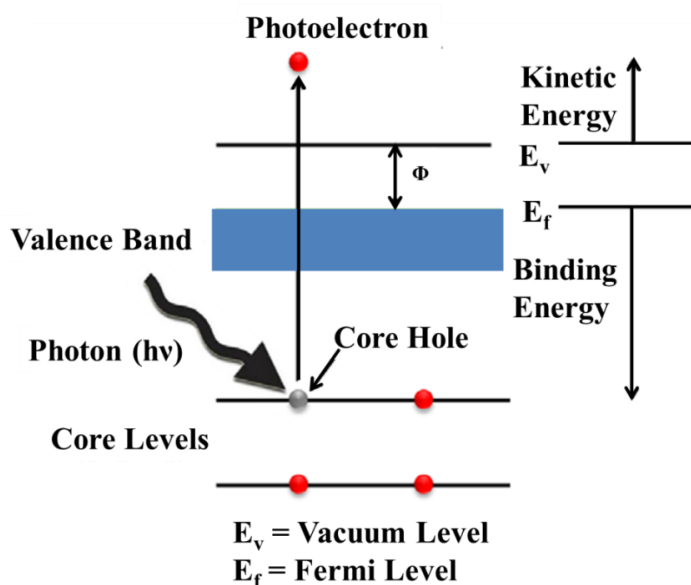


Figure 2.8. Schematic diagram of XPS processes.

The initial state accounts for the core level binding energy shifts and is used for obtaining chemical state information. The chemical surrounding of an atom decides the

effective charge on the core electron. With the change in the chemical surrounding, this effective charge is altered. Thus a change in binding energy is caused. This manifests as a chemical shift or surface core level shift and is indicative of the oxidation state of the atom. More the binding energy, more tightly will be the electron bound to the nucleus and therefore in the case of high Z elements, the binding energy will be high.

The schematic of the XPS process is depicted in **Figure 2.8.** Generally, an electron in an orbital possesses orbital angular momentum due to coupling between magnetic fields of spin (s) and angular momentum (l). The B.E of the electrons not only depends upon the level from which it is ejected, but also on the formal oxidation state and local chemical coordination environment of the atom. Therefore, one can identify the oxidation states as well as the chemical environments from the observed B.E values.

In the present study, the composition, chemical state and relative intensity of different element present in the DLC and DLC-Au nano-composite films were determined using XPS (ESCA, M/s. SPECS, Germany,) system with a monochromatic Al K_{α} (1.4866 KeV) X-ray source at a relatively low power of 350 W and a PHOIBOS 150 MCD-9 analyzer with a resolution of 0.67 eV for 656 keps at band pass energy of 10 eV.^{61, 65} The spectrometer was calibrated using a standard silver sample. SpecsLab2 software was used to analyze the data. Curve fitting analysis was based on Shirley back-ground subtraction and application of Gaussian–Lorentzian line shapes.

2.3.4. Scanning Probe Microscopy (SPM)

Scanning Probe Microscopy (SPM) has emerged as a useful and non-destructive imaging tool with sub nanometric spatial resolution since its invention.⁷⁷ It works on the principle of the force distance relation between the probe and specimen surface. This is a versatile technique

with multiple modes like electrical, magnetic, friction force and acoustic force.⁷⁸ It can also be used to probe insulators, semiconductors and conducting materials. Atomic force microscope (AFM) probes materials surface (morphology) with a sharp tip of few micron length and 30 to 50 nm radius of the curvature. The tip is attached to a free end of a cantilever with few hundred microns length and fixed at the other end. A micro fabricated cantilever with optical lever detection makes it possible to measure the applied force in terms of deflection. As the tip approaches close to the sample surface the interaction of forces between tip and sample cause deflection of the tip. The schematic drawing for force as a function of distance shown in **Figure 2.9. (a)** indicates range of attractive to repulsive force regime experienced by the tip when brought in contact with the sample surface with a constant load.

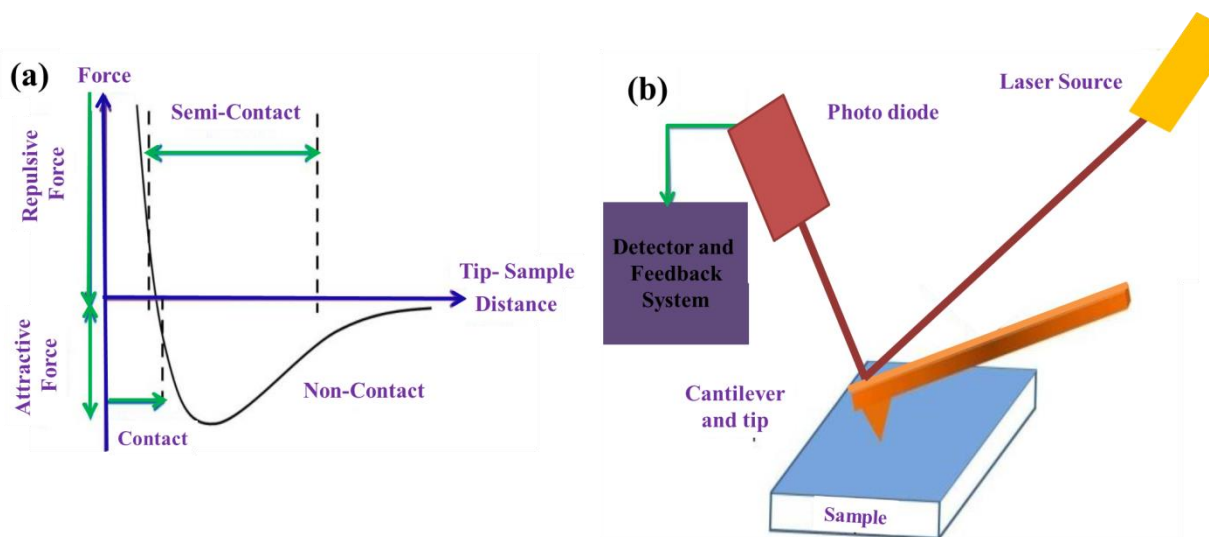


Figure 2.9. A schematic representation of a) force displacement curve of tip and sample and b) Atomic Force Microscope (AFM)

In AFM measurements vertical/lateral elastic forces, adhesion force and friction force operate between tip and sample.⁷⁹ The deflection of the cantilever, which is proportional to

force between tip and sample is measured by detecting a focused laser beam deflection from the back side of the cantilever by a segmented photodiode. A schematic representation is shown in **Figure 2.9.(b)**. The tip deflections are further processed to generate the topography map of sample surface. Acoustic Force mode is used to map the variation in local elastic modulus (E) at nano scale.

In the present work, elasticity mapping is carried out using a high resolution Scanning Probe Microscope (SPM) (NTEGRA Prima, M/s. NT-MDT, Russia) with several advanced modes.⁶¹ A stiff cantilever with a stiffness constant of 30 N/m and dimension as $125 \times 30 \times 5 \mu\text{m}^3$ is used in contact mode for AFAM study of particulate laden DLC films along with Si as the reference. To observe the uniformity and local structure of each film, several scans are carried out on both large ($5 \times 5 \mu\text{m}^2$) and small ($2.5 \times 2.5 \mu\text{m}^2$) areas, respectively. The resonance frequency of the cantilever is ~ 330 kHz. In AFAM, an ultrasonic transducer is attached beneath to the specimen stage, which vibrates in the frequency range of 0-5 MHz. The specimen surface is scanned by the cantilever in contact mode through the tip. In this technique, the mechanical boundary conditions are influenced by two kinds of interactions. First interaction is nonlinear contact mode function of distance, which is due to mutual interaction between the tip and the film surface without vibration. It becomes attractive and repulsive depending on the tip position at larger distances and in contact with the specimen surface, respectively; again it increases rapidly with further pressing of the tip against the specimens. The second interaction is between the longitudinal acoustic wave emitted from the transducer and the specimen which causes out-of-plane vibrations on the specimen surface leading to variation in the mechanical boundary conditions. Thus, the sensor tip helps in transmission of the surface vibrations into the cantilever. Photo diode and a lock-in-

amplifier are used to estimate and evaluate the cantilever vibrations. Coupled modes of vibration specific to surface elasto-mechanical response are measured and a spatial elasticity map is eventually generated. The expression for stiffness (K^*) of the coupled oscillator system can be written as; ⁸⁰⁻⁸⁴

$$K^* = \sqrt[3]{6RF_C E^{*2}} \quad \dots\dots\dots (2.2)$$

where, F_C , R and E^* are the applied static force, radius of the sensor tip and the reduced elastic constant of the tip and the specimen, respectively. E^* is given as follows:-

$$\frac{1}{E^*} = \frac{1}{E_{\text{tip}}^*} + \frac{1}{E_{\text{Specimen}}^*} \quad \dots\dots\dots (2.3)$$

$$\text{where, } E_{\text{tip}}^* = \frac{E_{\text{tip}}}{(1-\nu_{\text{tip}}^2)} \quad \text{and} \quad E_{\text{Specimen}}^* = \frac{E_{\text{Specimen}}}{(1-\nu_{\text{Specimen}}^2)}$$

Here, “ ν_{tip} ” and “ ν_{specimen} ” represent Poisson’s ratios of tip and specimen, respectively.

The AFAM principle is based on contact resonance spectroscopy. The interactions of the cantilever tip with the stiff region of the specimen surface; enhances the frequency and amplitude of contact resonance curve a decrease in FWHM. In addition, the reverse result is observed in case of the tip and softer region interactions. Hence, the appropriate contrasting features to be exhibited completely depend on the selection of the operating frequency. For e.g. operating frequency with higher value than the resonance frequency represents the stiffer and softer regions as bright and dark regions, respectively. However, if the operating frequency is lower than resonance frequency, a contrast inversion exists causing stiffer region to appear as dark and vice versa. This AFAM principle is useful for discrimination of hard and soft regions.^{61, 83} In our study, presence of particulates (~ micrometers) hinders the spatial elasticity mapping with accuracy so we’ve conducted the AFAM study by mapping with magnitude of the coupled oscillation. Point spectroscopy technique is implemented to

estimate the relative stiffness of flat and particulate regions on DLC surface with respect to Si (111). In addition to AFAM, AFM images are also obtained between the tip and the film surface without any vibration.

2.3.5. Field Emission Scanning Electron Microscope (FESEM) and Energy Dispersive X-ray Spectroscopy (EDS or EDX)

The field emission scanning electron microscope (FESEM) is a versatile tool used for morphology analysis of nano-materials and nanostructures. In principle, a primary electron beam is generated by external voltage application to the electron emitting filament.⁸⁵ When the electron beam with very fine spot size of ~5 nm and energy ranging from a few hundred eV to 30 KeV interacts with specimen, it undergoes either elastic or inelastic scattering. The scattered electrons with energy of <30 eV is known as secondary electron (SE). The elastically scattered electrons with angle > 90° are referred as back scattered electrons (BSE). When the energy of the emitted electron is > 50 eV, is termed as BSE.⁸⁶ Generally, SE and BSE carry information of z-contrast and topography. This information is detected in corresponding detectors. This technique has a resolution of about few nm and can operate at wide range of magnifications (10 to 500,000 X). The technique is considered to be non-destructive excluding the electron beams radiation induced surface damage. The electron beam produced by the field emission is 1000 times narrower than that produced in a conventional SEM and produces cleaner images with much less electrostatic distortions and high spatial resolution (< 2 nm). This high spatial resolution permits one to image nanoscale topography.

The electrons ejected from the specimen surface (SEs and BSEs) are collected by appropriate detectors. The detector output regulates the brightness of a cathode ray tube

(CRT) through one to one correspondence of each point on the specimen surface to each point on the screen. The secondary electrons are the most common signal of the SEM for multiple applications e.g. morphological analysis; particles size measurements, fracture analysis, microstructural homogeneity and determination of coating thickness from cross section. In addition to secondary electrons imaging, energy dispersive X-ray (EDX) analysis is also a useful tool for elemental compositional analysis. The collision of primary electrons with electrons of the atom helps in ejection of core electrons. Hence, the excited atom relaxes to ground level by either emitting a characteristic X-ray photon or an Auger electron. The X-rays signals emitted can be sorted by either energy or by wavelength using an EDX detector or by a wavelength spectrometer electron probe micro analyzer (EPMA). The distributions reveal about the type of element and also give the information about its spatial distribution in the sample. The output signal from the detectors corresponds to the amount of X-ray photons from the area subjected to electron bombardment. In EDX equipment the output data is in the form of a histogram of counts versus X-ray energy. The characteristic X-rays are known as the fingerprints which provide the elements present in the samples.

In the present work FE-SEM (SUPRA55, M/s. Carl Zeiss, Germany)⁶¹ and SEM (Helios NanoLab-600i dual beam field emission, M/s. FEI) were used to study the morphology and size of DLC and DLC-Au nano-composite films, respectively. Semi-quantitative elemental analyses were carried out by Energy Dispersive Spectroscopy (EDS) microanalysis using an Apollo X Silicon Drift Detector attached to the SEM (Helios NanoLab-600i dual beam field emission). The detailed morphology and semi-quantitative elemental composition studies are discussed in chapter-3 and 5.

2.3.6. X-ray Diffraction (XRD)

When an electromagnetic radiation of wavelength λ incident on a crystalline material having periodic structures in the length scale of λ ; diffraction event takes place. Since X-rays have wavelength comparable to interatomic spacing in a crystal, it can interact with the solid and scatter to produce a diffraction pattern.⁸⁷

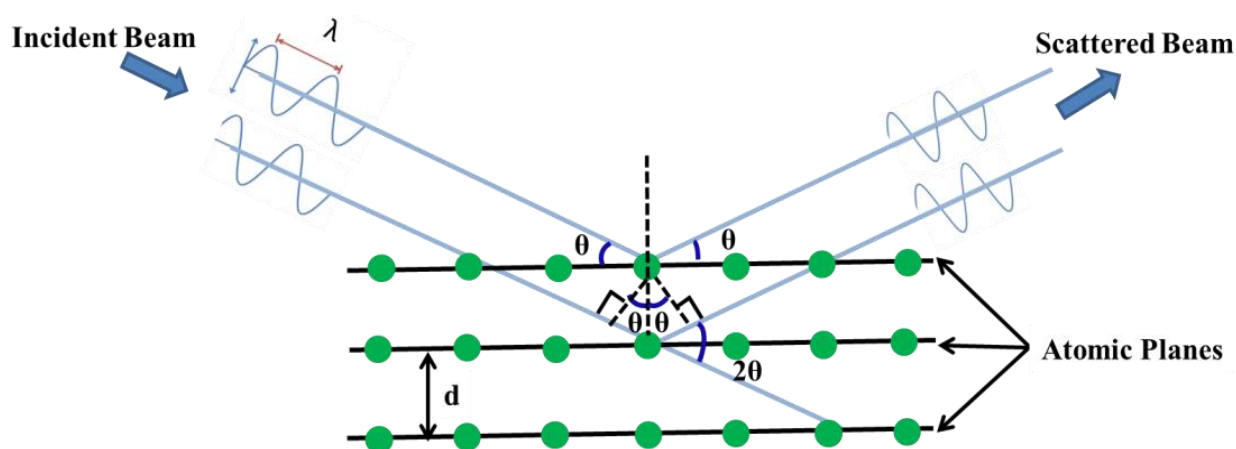


Figure 2.10. Schematic representation of X-ray diffraction process.

This happens when the interaction satisfies the Bragg's diffraction criterion given as follows:

$$n\lambda = 2d \sin \theta \quad \dots\dots\dots (2.4)$$

where, n is an integer representing the order of diffraction, λ is the wavelength of the electrons, d is the inter-planar spacing for the family of diffracting planes and θ is the diffracting angle. The wavelength of the X-ray used is normally $\text{Cu K}\alpha = 1.54056 \text{ \AA}$. Each peak in the diffraction pattern can be correlated to a set of planes in a crystal lattice. Different set of planes have different inter-planar spacing and according to Bragg's condition θ must vary with d variation. A schematic view of the X-ray Diffraction (XRD) process is shown in

Figure 2.10..

In the present study, grazing incidence X-ray diffraction (GI-XRD) (Equinox 2000, M/s. Inel diffractometer, USA) was used to reveal the structural information of DLC-Au nano-composite films.⁶⁵ DLC is an amorphous material with no long range order therefore; no sharp peak was obtained in the diffraction pattern. In this study, parallel beam optic with global mirror, K_{β} filter (Ni) and Cu K_{α} radiation was used to obtain the diffraction pattern of the DLC films. The angle of incidence was kept at $\theta = 0.5^{\circ}$.

2.3.7. Transmission Electron Microscopy (TEM)

The transmission electron microscopy (TEM) is such an advanced technique, which can provide the morphological, compositional and crystallographic information of a very thin film. In this technique an accelerated electron beam from electron gun with high voltage of the range of 100-400 kV moves towards a thin specimen, which follows (1) scattering from specimen, (2) transmission through specimen and (3) absorption by the specimen. The specimen needs to be thin enough for easy electron transmission. Generally, in TEM the nanostructured materials are usually loaded on Cu grid for analysis. The SAED patterns of single crystal, polycrystalline and amorphous material exhibit spot, sharp ring and diffused like ring patterns, respectively.⁸⁸

- **Electron Diffraction:** The diffraction pattern formation in the back focal plane is formed due to forward scattered and transmitted electrons. The electron diffraction pattern obtained from the atoms plane space follows Bragg's law of equation (2.4). Crystalline phase, crystalline size, nature of defects, etc can be determined from the diffraction pattern.
- **Dark Field Imaging:** This image forms with specified diffracted electron beams. It reveals the phase differentiation.

- **Bright Field Imaging:** The bright field image is formed from unscattered transmitted electrons. The contrast of this image provides thickness and density variation.
- **High Resolution Imaging:** It is a combination of diffraction and bright field imaging. It determines the lattice parameters, grain orientation and information of individual defects.

TEM analysis can provide Selected Area Electron Diffraction (SAED) patterns, bright field images, dark field images; high resolution images (HRTEM) and Fast Fourier Transform (FFT) images. The major components of TEM are as follows:-

- **Illumination system:** Electron gun, condenser lenses, condenser apertures
- **Objective lens/stage:** objective lenses, sample stage/holder
- **Imaging system:** Intermediate and projector lenses, fluorescent viewing screen or computer display via a detector, CCD, or TV camera.

In this present study, TEM high resolution imaging was performed for DLC-Au nano-composites. A High Resolution TEM instrument (Libra 200FE, M/s. Carl Zeiss, Germany), equipped with in-column energy filter with the energy resolution of 0.7 eV was used to analyze diffraction patterns for different phases and distribution of the Au nano-clusters present in DLC-Au nano-composite films.⁶⁵

2.3.8. Electron Energy Loss Spectroscopy (EELS)

EELS is an analytical technique based on the change in K.E of inelastically interacted electrons with a specimen. EELS in a TEM instrument provide structural and chemical information of the specimen, with a low spatial resolution. The physics involved in EELS is that, when electrons travel through a sample, they are subjected to elastic or inelastic

scattering after interacting with the atoms of the specimen.⁸⁹ Electrostatic forces play a key role in causing the collision of the incident electron and the atomic components which are charged particles. The elastic scattering occurs due to the interaction of an incident electron with an atomic nucleus. Since, there is a large difference between the mass of the atomic nucleus and rest mass of an electron, the energy exchange is small and therefore, restricts the measurement by using TEM-EELS system. Inelastic scattering involves columbic interaction between the incident electron and atomic electrons of the specimen which are in similar mass and therefore allows appreciable exchange of energy (loss). The energy loss could be generally a few eVs up to hundreds of eVs which are in the measurable range of the TEM-EELS system. An EEL spectrum comprises of signals:

- **Zero loss peak:** This is an intense signal and arises due the elastic interaction (no loss of energy) of the incident electron with the specimen.
- **Low loss region:** It occupies the region between the zero loss peak and ~100 eV. Peak intensity indicates thickness of the sample. Plasmons are the main feature in this region.
- **High loss region:** These are well defined peak that appears at energy loss >100 eV and are weak signals. The ionization edge refers to the energy required to transfer core electron from ground state to the lowest unoccupied state. The energy loss is a finger print for a particular element which leads to qualitative analysis of the material.

In the present study, HRTEM-EELS (Libra 200FE, M/s. Carl Zeiss, Germany), equipped with in-column energy filter with the energy resolution of 0.7 eV was used to analyze the DLC-Au nano-composite films. It is four magnetic prisms that bends the beam

into the shape of omega ' Ω ' and therefore called as omega filter. The spectrum is formed just down the filter and the HRTEM lenses project it onto the electronic detector, a CCD camera. The bonding state and sp^3 content in the DLC films were determined using this technique.

2.3.9. Contact Angle (CA) Measurement

The contact angle is defined as the angle between the liquid-solid and liquid-vapor interface. Geometrically it is measured as the angle between the tangent to the liquid/air interface and the tangent to the solid/air interface.⁹⁰ The measurement can be used for investigating the surface wettability of the material of interest by a specific liquid. When the drop completely wets the surface, it indicates high surface energy. Depending on the value of contact angle, the wetting nature of the surface is further sub classified into four categories: hydrophilic, superhydrophilic, hydrophobic and super hydrophobic. The term is referred as superhydrophilicity, i.e.; the CA is $\sim 0^\circ$ ($< 10^\circ$).⁹⁰ There exist surfaces, in which the CA will be more than 10° but less than 90° . This condition is known as hydrophilicity. When the CA will be $\sim 180^\circ$ and the state is called superhydrophobic state. When the CA ranges occur in between 90° to 150° the state is referred to hydrophobic surface.

In the present study, contact angle experiments of the samples were carried out in ambient environment using a contact angle meter (DSA100M, M/s. KRÜSS, Germany) provided with a CCD camera.⁶⁵ The sessile drop method was used for the contact angle measurements. The surface energy and contact angle of all particulate laden DLC films were obtained using two liquids (water and diiodo-methane). The amount of water and diiodo-methane droplets released was ~ 1 - $2\ \mu\text{l}$. CCD camera was used to get the droplet image. The KRÜSS ADVANCE 1.6.2.0 software was used for data analysis.

2.3.10. Nano Indentation

Nano-indentation is a novel and versatile depth sensing indentation technique to investigate the local mechanical properties of bulk materials and thin films. This technique is capable of characterizing coated surfaces of size down to 100 nm across and thin films of thickness < 5 nm. The load used in nanoindentation technique falls in the range 100 μN to a few mN. The indenter is moved at a controlled rate and applied a maximum force in order to pierce into the specimen to reach particular depth and again it is withdrawn from the surface.

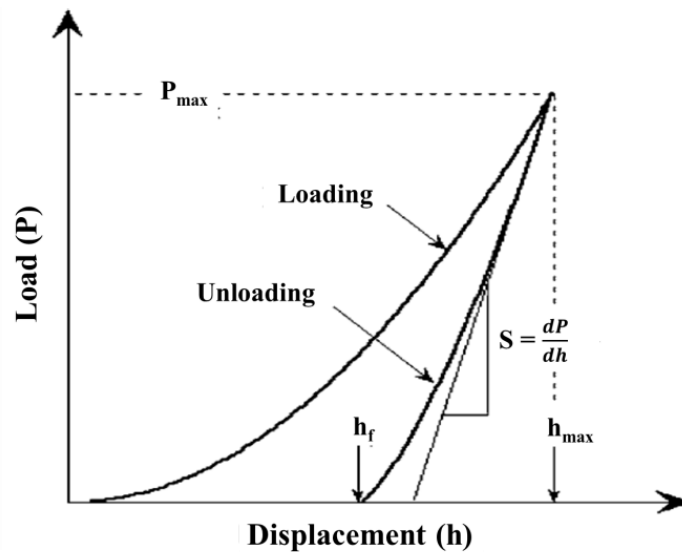


Figure 2.11. Schematic illustration of indentation load-displacement curve with important measured parameters.

Generally, it measures the hardness, modulus and stiffness of a material and also allows the depth resolved indentation from a surface to sub-surface. The hardness of the material can be defined as the load divided by residual indentation area and the indentation impression is only a few nanometers in depth. In this experiment the mechanical properties can be determined directly from indentation load and displacement measurements without the need to image the hardness impression.

The nano-indentation system consists of a precision loading arrangement and accurate measurement of displacement having high thermal stability. The precision loading could be accomplished by electromagnetic deflection of a spring and the displacement could be measured by a capacitance gauge or Linear Variable Differential Transformer (LVDT). In nano-indentation, the most commonly used tip is the Berkovich tetrahedral diamond with sharp three sided point like tip. The hardness (H) and elastic modulus (E) are calculated from load displacement profile of indentation test using Oliver and Pharr formalism.⁹¹

A schematic representation of a typical load displacement curve set obtained with a Berkovich indenter is presented in **Figure 2.11.**, where the P and h are the load and displacement of the indenter. Deformation during loading is assumed to be both elastic and plastic in nature as the permanent hardness impression forms. During unloading, it is assumed that only the elastic displacements are recovered. From the $P - h$ curve, the maximum load (P_{max}) and the maximum displacement (h_{max}) must be measured. The slope of the upper portion of the unloading curve during the initial stages of elastic unloading is called stiffness, which is defined by $S = dP/dh$. The parameter h_f is the final permanent depth of penetration after the indenter is fully unloaded.

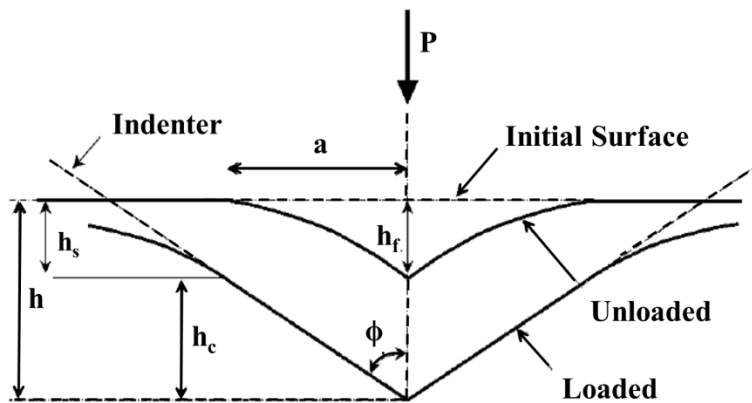


Figure 2.12. Schematic illustration of the unloading process showing contact geometry parameters.

The exact procedure used to measure H and E is based on the unloading processes shown schematically in **Figure 2.12**. During the indentation, the specimen surface is displaced at the contact perimeter from the initial surface and given by $h_s = \epsilon (P_{max}/S)$ which is a constant that depends on the geometry of the indenter. The vertical displacement of the contact periphery i.e. the depth along which contact is made between the indenter and the specimen is denoted by h_c ($h_c = h_{max} - h_s$) and is related by the following;

$$h_c = h_{max} - \epsilon \frac{P_{max}}{S} \quad \dots\dots\dots (2.5)$$

Assuming $F(d)$ be an area-function that describes the cross sectional area of the indenter at a distance d back from its top of the tip, the contact area (A) is defined as $A = F(h_c)$. From the contact area, the hardness is estimated from the below relation.

$$H = \frac{P_{max}}{A} \quad \dots\dots\dots (2.6)$$

The measured stiffness is related to contact area as $= \sqrt{\frac{4\pi}{A}} E_{eff}$, where “ E_{eff} ” is the effective elastic modulus defined by the below equation.

$$\frac{1}{E_{eff}} = \frac{1-\nu^2}{E} + \frac{1-\nu_i^2}{E_i} \quad \dots\dots\dots (2.7)$$

The indentation modulus E can be extracted by giving the elastic constants of indenter (E_i), Poisson’s ratio value of specimen (ν) and indenter (ν_i) as input in above relation. In this study, the nano-mechanical properties of DLC⁶³ and DLC-Au nano-composite films were carried out by a compact platform Ultra Nano-indentation Tester (M/s. Anton Paar, Switzerland) equipped with a three sided pyramidal diamond (Berkovich) tip with an end radius of 30 nm. Indentation was performed at different linear loads following

the standard process i.e. the loading and unloading rates are maintained at twice of the peak load.

2.3.11. Tribometer

Tribology is defined as the science and technology of interacting surfaces in relative motion. It consists of three independent fields such as friction, lubrication and wear.⁹² The micro tribometer is used to study the friction and wear resistant behavior when two materials slide on each other. This instrument consists of a spherical probe of known geometry which is placed on the specimen to be tested with a constant load as depicted in **Figure 2.13. (a)**. The sample is either rotating or reciprocating in a linear track with constant speed. The resulting frictional forces acting between the probe and the specimen are measured. The friction coefficient (μ) is determined during the test by measuring the deflection of the elastic arm. Wear coefficients for the pin and disk materials are calculated from the volume of material lost during the test. This simple method facilitates the study of friction and wear behavior of almost every solid state material combination with or without lubricant. Furthermore, the control of the test parameters such as speed, frequency, contact pressure, time and environmental parameters (temperature, humidity and lubricant) allows simulation of the real life conditions of a practical wear situation.

The linear tribometer reproduces the reciprocating motion, typical of many real world mechanisms. The instrument measures (**Figure 2.13. (a)**) a friction coefficient for both the forward and backward displacement of the stroke and the software generates data on Hertzian pressure, static partner and sample wear rates. The reciprocating technique is also very useful for studying the variation over time of the static coefficient of friction.

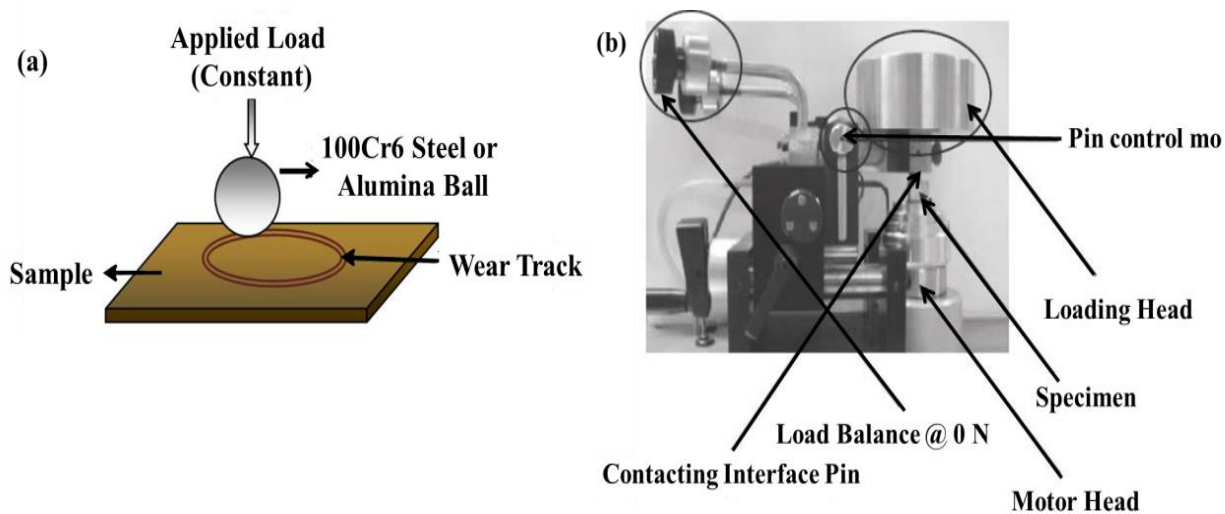


Figure 2.13. (a). Schematic representation of ball on disc tribometer and (b) Experimental set up for tribological study.

In the present study, a ball on disk micro tribometer (M/s. CSM Instruments, Switzerland) was used to perform the tribological tests.⁶³ Steel ball of spherical shape having diameter, 6 mm and a surface roughness of 0.06 mm was taken as the counter body (DLC-Au nano-composites) to determine the coefficient of friction. Both normal load and sliding speeds were kept constant at 1 N and 2 cm/s, respectively. All measurements were carried out at ambient (dry and unlubricated) condition. The measurements were carried out following ASTM standards (ASTMG133-95).

2.3.12. Summary

This chapter summarizes the salient features and capabilities of the experimental set-up built to carry out pulsed laser deposition of diamond-like carbon and DLC-Au nano-composite coatings. Various solid state analytical techniques used for the characterization and evaluation of the DLC and DLC-Au nano-composite thin films were also briefly explained along with the rationale behind the selection of each technique.

CHAPTER 3

Raman Investigation of Particulate Laden Diamond-like Carbon Films Grown by Nd: YAG Laser Ablation

“If you want to find the secretes of the universe, think in terms of energy, frequency and vibration”

Nikola Tesla

This chapter starts with a brief introduction to particulate, one of the limitations of diamond-like carbon (DLC) growth by pulsed laser deposition (PLD) followed by synthesis of particulate laden DLC film and its vibrational investigation through multi-excitation Raman characterizations.

3.1. Introduction

PLD has emerged as an effective deposition technique for synthesis of un-hydrogenated DLC films at room temperature following the sub-plantation growth mechanism. In this technique, growth of DLC film completely depends on the kinetics and energetic of the plasma species generated by the laser ablation of the graphite target and quality of the DLC film evolves with kinetic energies and charge states of the ablated carbon particles in the plasma plume.^{15,}

⁹³ Research groups like Tabbal *et. al.*, and Ruiz *et. al.* have investigated the DLC growth by PLD for parametric effects on its structural, optical, electrical and mechanical properties, with an aim to synthesize high quality DLC films for the desired applications. At optimized conditions, PLD produces better quality DLC films as compared to Filtered Cathodic Vacuum Arc (FCVA) deposition and Mass Selected Ion Beam (MSIB) deposition

techniques.^{33, 94, 95} However, the limitation of PLD is appearance of particulate (macro size) on the film surface due to molten state of the target surface during ablation. In the case of low atomic mass elements like carbon-based targets, existence of liquid state is uncertain, and hence, the most probable reasons for the formation of particulates (droplets) are:

i) explosive dislocation of the substance during plasma plume expansion and ii) coalescence of species in plasma plume during the target-to-substrate flight.^{95, 96} The appearance of particulate on the DLC film surface influences morphology, optical energy gap, surface energy, composition, vibrational property and surface mechanical properties of the films.

The Nd: YAG laser (1064 nm) generates more number of particulates during ablation than excimer lasers (UV wavelength) pertaining to its higher wavelength, which enhances its penetration depth into the target surface. The majority of literature reports suggest the idea of incorporation of elements such as N, F, Si or metal at nanoscale (nano-particles and nano-crystallites) to enhance the physical, mechanical and tribological properties of DLC for diverse applications.^{18, 94, 97-99} At the same time, presence of particulates (sp^2 rich) on the DLC surface hinders the proper analysis for element incorporated DLC films. To get rid of this problem, methods like application of magnetic field and mechanical kinetic energy filter are used in recent times during synthesis in the deposition system.^{100, 101} Though the effect of particulates is known, a systematic investigation is lacking. This motivate us to carry out proper investigation of particulate influence on DLC properties before incorporating such elemental nanoparticles in DLC by common PLD systems, which doesn't have facilities for filtering particulates. Hence in this chapter, we report a detailed vibrational investigation of particulate laden DLC films grown at few selected laser pulse energies of an Nd: YAG laser (1064 nm) using multi-excitation Raman characterization followed by thickness

measurement and morphology studies using surface profilometer, FESEM and AFM, respectively.

3.2. Characterizations

Particulate laden DLC films were grown on silicon (111) substrates at four different laser pulse energies (100-400 mJ) with an interval of 100 mJ, using an Nd: YAG laser (M/s Quanta Systems, Italy). The specimens were labeled as DLC-1, DLC-2, DLC-3 and DLC-4. The detailed synthesis parameters with procedure have been described in the section 2.2.1.1. of chapter-2. Film thickness was measured using stylus profiler. AFM and FESEM were used for morphological analysis. Visible (514.5 nm) Raman mapping was used to observe the influence of particulates on chemical structure of the flat region of DLC films. Individual vibrational investigations on flat as well as particulate regions of the DLC films were carried out by using visible (514.5 nm) and UV (325 nm) laser Raman spectroscopy.

3.3. Results and Discussion

3.3.1. Thickness of DLC films

The average thickness of the DLC films (DLC-1, DLC-2, DLC-3 and DLC-4) measured by a surface profilometer were 105 (± 3), 120 (± 5), 144 (± 12) and 169(± 13) nm, respectively.⁶¹ It is observed that thickness value increases monotonically with rise in laser pulse energy. This can be attributed to the ejection of larger material flux at higher pulse energy.

3.3.2. Morphological Analysis

3.3.2.1. FESEM

Figure 3.1. (a-d) shows the FESEM micrographs of the particulate laden DLC films deposited at selected laser pulse energies (100, 200, 300, and 400 mJ) with the particulate as inset.⁶¹ It is clear from **Figure 3.1. (a-d)** that there are number of small irregular particulates

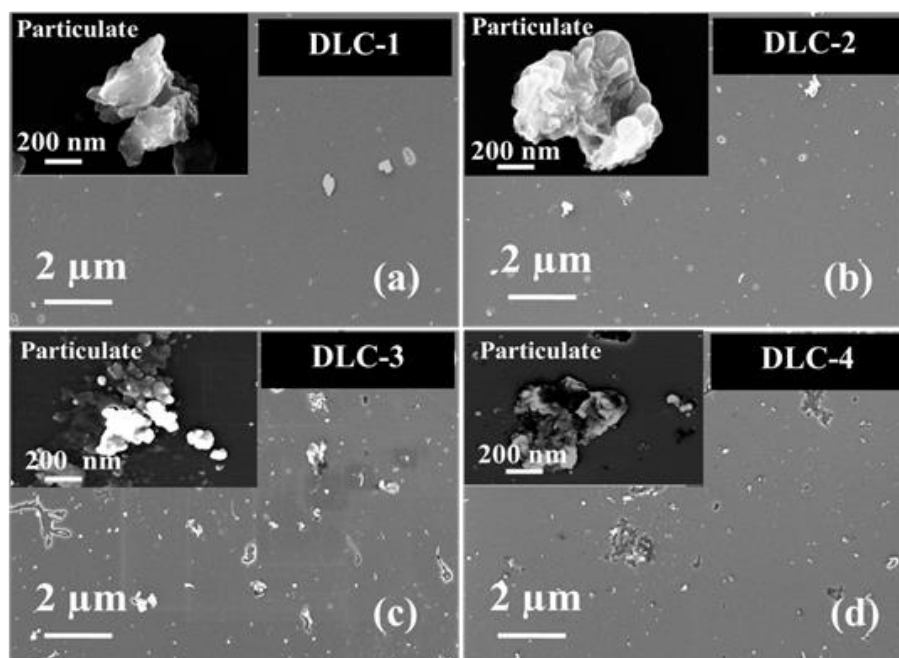


Figure 3.1. FESEM images of (a) DLC-1, (b) DLC-2, (c) DLC-3, and (d) DLC-4 films with particulate as inset.

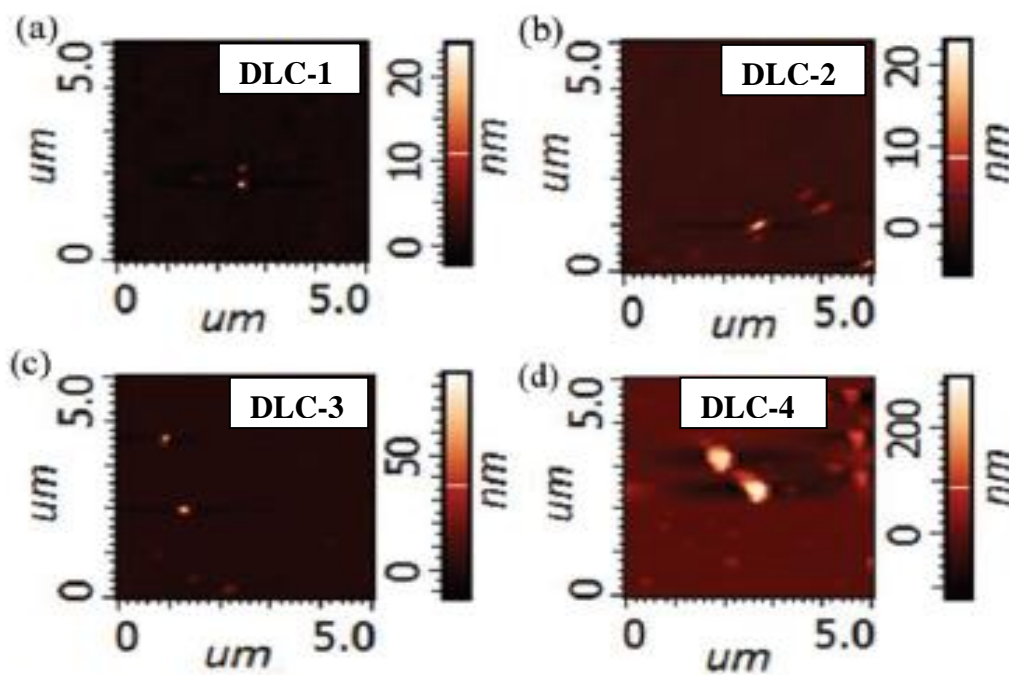


Figure 3.2. AFM images of (a) DLC-1, (b) DLC-2, (c) DLC-3, and (d) DLC-4 films.

present throughout the surface of the films. In addition, the number density of particulates is also found to increase with increase in laser pulse energy.⁶¹

It is also interesting to note that, that DLC-3 and DLC-4 films contain more number of larger size particulates (**Figure 3.1. (c, d)**). This surface modification with the increase of laser pulse energy can be attributed to the fact that the high energy density of longer wavelength (1064 nm) of Nd: YAG laser ejects higher number of particulates with modified chemical structure and size due to the kinetics of associated plasma.¹⁴

3.3.2.2. AFM

AFM images are shown in **Figure 3.2. (a-d)**.⁶² The topographical analysis of DLC specimens was carried out by tapping mode of AFM over an area of $5 \times 5 \mu\text{m}^2$. It is observed that at lower pulse energies (100 and 200 mJ), the height of particulate from flat surface is ~ 20 nm, whereas it increases to ~ 80 and ~ 260 nm with increase in laser pulse energies (300 and 400 mJ), respectively.

The surface roughness on flat regions of DLC films with laser pulse energy measured by AFM were $1.5 (\pm 0.5)$, $2.7 (\pm 0.5)$, $3.3 (\pm 0.5)$ and $4.5 (\pm 0.5)$ nm, respectively. It is observed that the surface roughness values of DLC films monotonically increases with increase in laser pulse energy. At higher laser pulse energy, the probability of particulate emission is more, which causes rise in surface roughness.⁶²

3.3.3. Influence of particulate on DLC surface studied by Visible Raman Mapping

The visible Raman intensity mapping for G and D peak along with the I_D/I_G ratio mapping on all particulate laden DLC surfaces are shown in **Figure 3.3. (a-d)**.⁶¹ The G and D-peaks were obtained from de-convolution of the Raman spectra obtained from the particulate regions. The intensity distribution on flat and particulate regions for all DLC films is clearly observed

from G, D and I_D/I_G ratio mapping. In this study, we emphasize on I_D/I_G ratio map of all DLC films to obtain the information about the presence of aromatic rings/chain type structures of sp^2 bonding in clusters. In addition, qualitative analysis of sp^3 content and DLC film density evolution in the particulate region with various laser pulse energies is also deduced from I_D/I_G ratio mapping.

The I_D/I_G ratio mapping in **Figure 3.3. (a)**, shows that particulate region of DLC-1 specimen possesses I_D/I_G ratio in the range 0.54–0.64, whereas the flat region shows a lower range 0.54–0.58. This result indicates that, the particulate and flat regions of DLC-1 films possess similar compressive stress as, which ensures similar densification as well as enhancement in sp^3 content.^{101, 102}

Figure 3.3. (b) reveals that the I_D/I_G ratio mapping in the particulate region of DLC-2 specimen exhibit similar contrast as compared to the particulate region of DLC-1. In fact, the particulate region has a variation in the wider range 0.50–0.65. As the flat region of DLC-2 specimen has lower I_D/I_G value (0.50–0.58) with respect to the particulate region, this indicates larger sp^2 bonded aromatic carbon clusters in these particulate regions compared to the flat region. I_D/I_G ratio mapping on both the regions reveals a random distribution pattern, which indicates that the regions on DLC-2 specimen are under non-uniform compressive stress but with non-identical values.^{102, 103} As a result densification and sp^3 content varies accordingly.

Figure 3.3. (c) depicts the I_D/I_G ratio mapping of DLC-3 specimen, which reveals that particulate and flat region possesses an I_D/I_G ratio values in the range 0.42–0.46 and 0.38–0.44, respectively. A gradual decrease of I_D/I_G ratio is observed from the center of the particulate region towards the flat region which indicates presence of uniform compressive

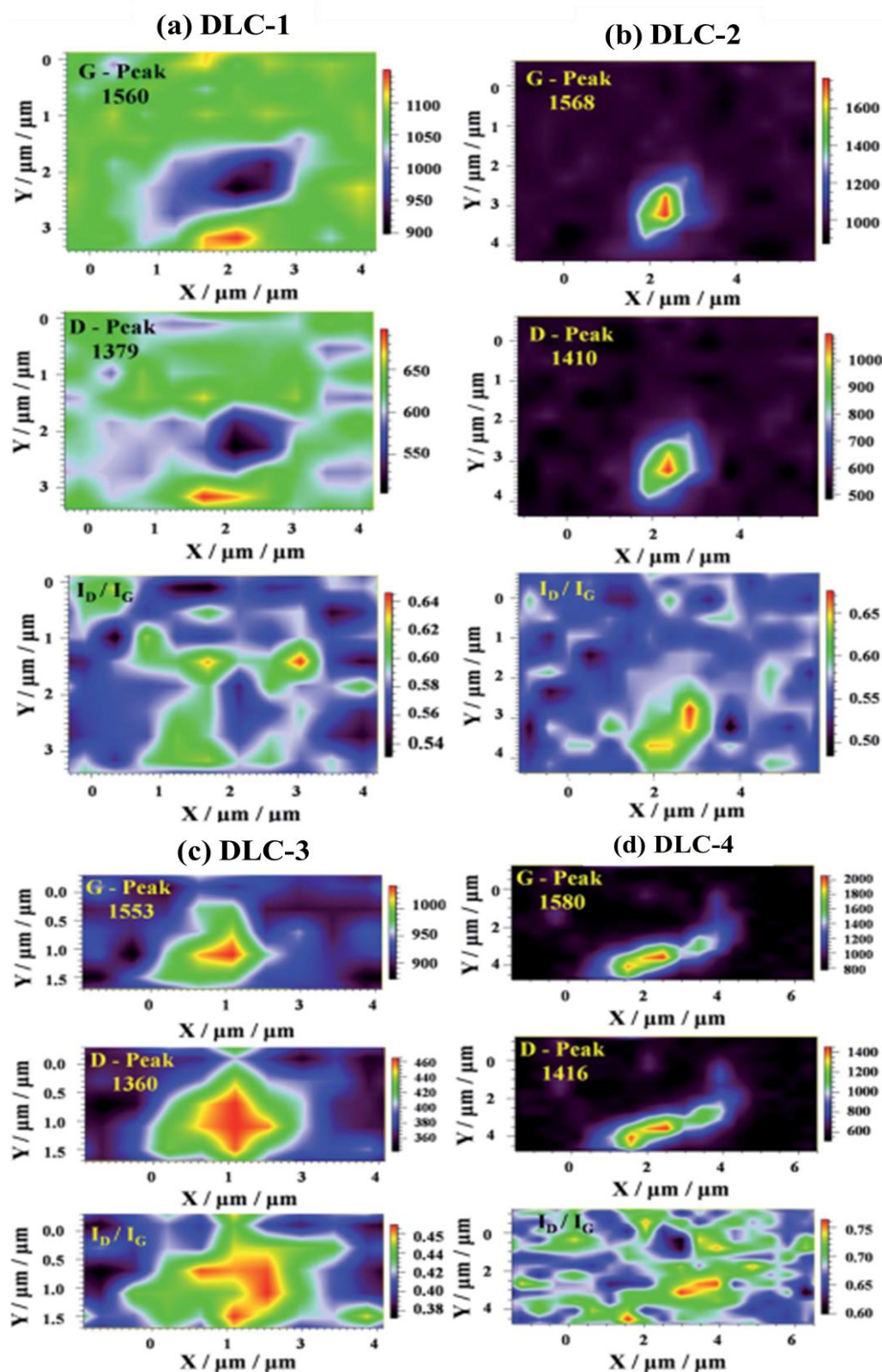


Figure 3.3. Visible Raman intensity mapping image for G-peak, D-peak and I_D/I_G of (a) DLC-1, (b) DLC-2, (c) DLC-3, and (d) DLC-4, respectively.

stress and densification.^{102, 103} Though in DLC-3 the particulate regions have also higher I_D/I_G ratio value than the flat region, but it is less as compared to DLC-1 and DLC-2 specimens. This indicates that although the particulate region of DLC-3 specimen possesses larger aromatic clusters than the corresponding flat region, but it is smaller than DLC-1 and DLC-2 specimens. Thus, the I_D/I_G ratio in flat and particulate regions of DLC-3 reveal that sp^3 content is relatively more as compared to DLC-1 and DLC-2 specimens.

The I_D/I_G ratio mapping of DLC-4 specimen presented in **Figure 3.3. (d)**, indicates that the intensity contrasts of the particulate and flat region lies in the range 0.65–0.75 and 0.60–0.72, respectively. The flat region shows identical pattern like DLC-2 specimen having lowest I_D/I_G value (0.60–0.72). The very high values of I_D/I_G on both the regions indicate that DLC-4 has higher aromatic sp^2 clusters with less sp^3 content and density as compared to DLC-1, DLC-2 and DLC-3.

From the above discussion, it can be concluded that both flat and particulate regions of DLC-3 possess smallest sp^2 clusters with highest sp^3 content. It is well known that visible Raman spectroscopy has higher sensitivity (50–230 times) towards sp^2 bonding compared to UV Raman spectroscopy. So, it is used as an indirect probing tool for sp^3 content. Hence, UV-Raman technique is used for detailed investigation on flat and particulate region of DLC films, as a suitable non-destructive technique to determine sp^3 content by probing just the topmost region (5–15 nm) of the samples.¹⁰⁴ In addition, the G-peak dispersion determined from both the excitations provides additional information regarding the evolution of disorder as a function of laser pulse energy. A detailed discussion is presented in subsequent section.

3.3.4. Multi-excitation Raman Analysis on Flat and Particulate regions

3.3.4.1. Visible Raman Analysis

The Visible-Raman spectra (**Figure 3.4, (a-d) and 3.5. (a-d)**) obtained from flat and particulate regions of DLC-1, DLC-2, DLC-3, and DLC-4 films are background subtracted and deconvoluted into two Gaussian peaks, such as G and D peak, respectively.^{61, 62} These two peaks correspond to two vibrational modes, such as G peak (stretching mode) around 1550–1600 cm^{-1} and the D peak (breathing mode) around 1355 cm^{-1} are assigned to zone centre phonons of E_{2g} symmetry and K-point phonons of A_{1g} symmetry, respectively.^{17, 103, 105}

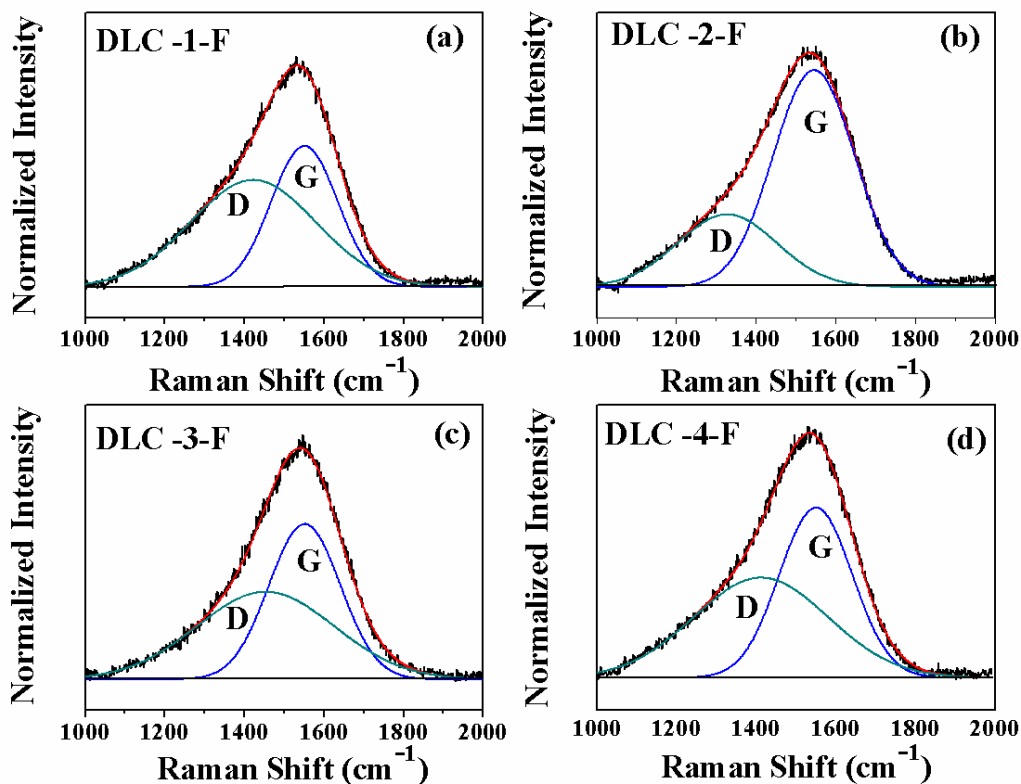


Figure 3.4. Deconvoluted visible (514.5 nm) Raman spectra obtained from flat regions of (a) DLC-1, (b) DLC-2, (c) DLC-3, and (d) DLC-4 films.

The G peak is the graphitic phase with the in-plane bond-stretching vibration of sp^2 bonded pair carbon atoms. This mode exists in all sp^2 sites without the need of six fold ring. The G band in the range of $1500\text{--}1630\text{ cm}^{-1}$ corresponds to sp^2 sites in both aromatic and olefinic molecules. The blue shift of G peak takes place due to smaller aromatic clusters having higher modes or decrease in number of ordered aromatic rings during transition from nano-crystalline graphite to $a\text{-C}$. It also reduces D peak intensity due to softening of the vibrational density of states. The deconvoluted Visible-Raman spectra of flat and particulate regions of all DLC films are presented in **Figure 3.4. (a-d)** and **3.5. (a-d)**, respectively.⁶¹

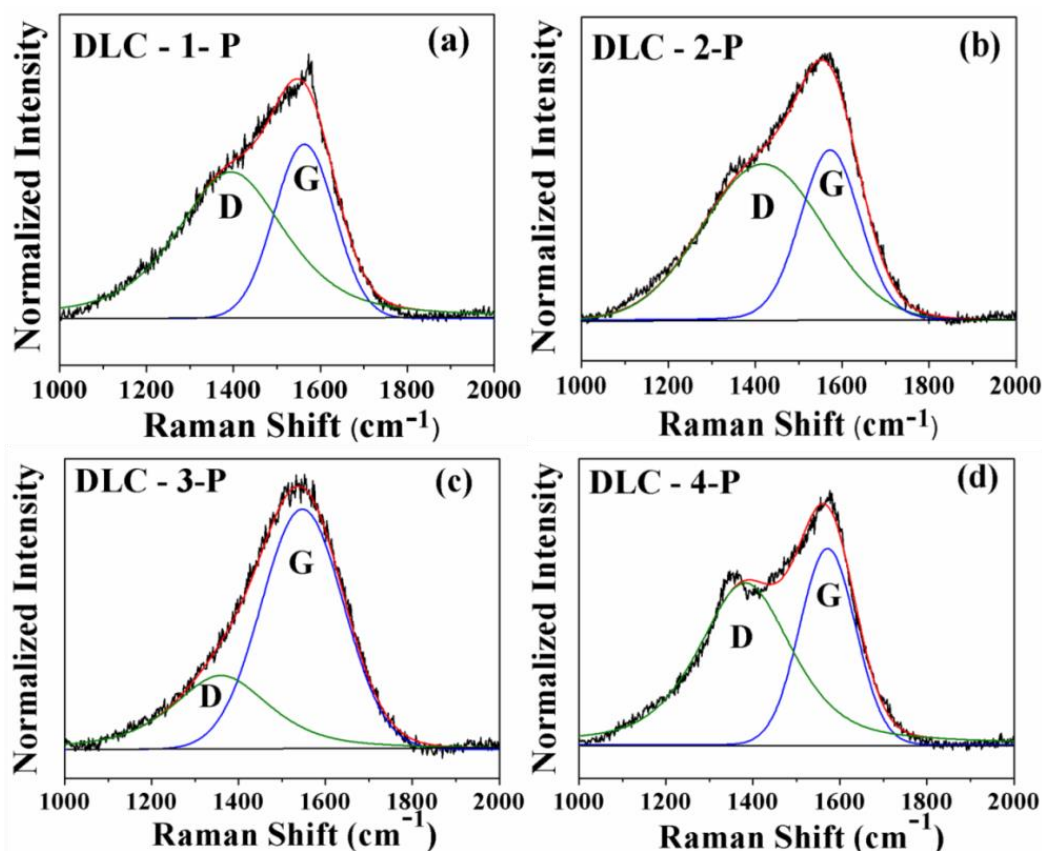


Figure 3.5. Deconvoluted visible (514.5 nm) Raman spectra obtained from particulate regions of (a) DLC-1, (b) DLC-2, (c) DLC-3, and (d) DLC-4 films.

The Peak positions, FWHM of G and D peaks, and I_D/I_G ratio (calculated from integrated intensity) determined from the deconvoluted Raman spectra obtained from flat region of DLC-1, DLC-2, DLC-3, and DLC-4 are tabulated in **Table 3.1.**⁶¹ The D and G-peak shifts along with their full width at half maxima (FWHM) and I_D/I_G are directly related to the density, size and structure of sp^2 clusters and indirectly to sp^3 content.¹⁰³ It is clear from **Table 3.1.** that I_D/I_G ratio decreases from DLC-1 to DLC-3 and rises sharply for DLC-4 whereas FWHM(G) follows reverse trend and G peak position increases from DLC-1 to DLC-2, and then decreases gradually. The I_D/I_G and G-peak position values indicate that, the flat regions of all DLC films are amorphous with higher sp^3 content and belong to the second/third stage of amorphization trajectory.¹⁰³ The sp^3 content of hydrogen free DLC was calculated from FWHM of G-peak of Raman spectra obtained from flat region of DLC films, using **equation (3.1)**¹⁰⁶

$$[C_{sp^3}] = -2.05 + 1.9 \times 10^{-2}W - 3.01 \times 10^{-5}W^2 \pm 0.08 \quad \dots\dots\dots (3.1)$$

where, “W” is the FWHM of G-peak and the last term is the standard deviation of the quadratic model.

Table 3.1. Deconvoluted data of visible (514.5 nm) Raman spectra obtained from flat regions of DLC films

Specimen	G-Peak Pos ⁿ (cm ⁻¹)	D-Peak Pos ⁿ (cm ⁻¹)	FWHM(G) (cm ⁻¹)	FWHM(D) (cm ⁻¹)	I_D / I_G	sp^3 Content
DLC – 1-F	1553	1396	211	351	1.06	62
DLC – 2-F	1557	1414	219.5	343	0.79	67
DLC – 3-F	1555	1398	223.7	357	0.66	69
DLC – 4-F	1552	1437	219	374	0.92	67

The calculated sp^3 content of DLC films are tabulated in **Table 3.1.**, which depicts that the variation of I_D/I_G values with laser pulse energy indicates a reverse trend of sp^3 content evolution, which is in concurrence with Ferrari's model.¹⁰³

Similarly, Visible Raman analysis on particulate region of DLC films is also carried out. The deconvoluted Raman spectra parameters, such as Peak positions, FWHM of G and D peaks, and I_D/I_G ratio (calculated from integrated intensity) obtained from particulate region of DLC-1, DLC-2, DLC-3, and DLC-4 are tabulated in **Table 3.2.** It is observed from **Figure 3.5. (a, b, and d)** that D-peak appears at 1379, 1410 and 1416 cm^{-1} for DLC-1, DLC-2 and DLC-4 films, respectively, with skewness associated with the G-peak. It is reported by Mapelli *et. al.* that the upward shift of D-peak and occurrence of intense D-peak as a prominent shoulder in DLC-2 and DLC-4 specimen indicate presence of large number of aromatic rings entrained in the particulate regions.¹⁰⁷ This observation needs appropriate information on cluster sizes. Hence, I_D/I_G ratio of Raman spectra obtained from the particulate region was used in Tuinstra and Koenig (TK) equation for second stage (nanocrystalline graphite to a -C) of amorphization trajectory to calculate the cluster size (L) in the DLC films.¹⁰³

Table 3.2. Deconvoluted data of visible(514.5 nm) Raman spectra obtained from particulate regions of DLC films

Specimen	G-Peak Pos ⁿ (cm^{-1})	D-Peak Pos ⁿ (cm^{-1})	FWHM (G) (cm^{-1})	FWHM (D) (cm^{-1})	I_D / I_G	Cluster size (nm)
DLC – 1-P	1560	1379	190	325	0.7	1.13
DLC – 2-P	1568	1410	180	360	0.9	1.28
DLC – 3-P	1553	1360	213	287	0.4	0.85
DLC – 4-P	1580	1416	135	338	1.1	1.41

The TK relations for second stage of amorphization trajectory are given as follows:

$$\frac{I_D}{I_G} = C(\lambda) \times L^2 \quad \text{..... (3.2)}$$

Where, $C(\lambda)$ is a constant but depends on the laser wavelength used for excitation (514.5 nm) and is 0.55 nm^{-2} . The cluster size calculated using above relation is tabulated in **Table 3.2**. **Figure 3.5.(c)** depicts the decrease of D-peak intensity in the shoulder region and lower wave number shift for particulate region of DLC-3, which indicates that this region possesses either reduced number of ordered aromatic rings or more number of olefinic carbon chains consisting of sp^2 bonds, which is in agreement with the results of Beeman *et. al.*¹⁰⁸ In addition, **Table 3.2** shows that particulate region of DLC-3 possesses the smallest sp^2 cluster (0.74 nm), which indicates that the sp^2 bonding of carbon atom in this region is more of chain type. However, particulate region of DLC-1 (1.23 nm), DLC-2 (1.28 nm) and DLC-4 (1.34 nm) possess higher cluster sizes, which indicates that the sp^2 bonding of carbon atom in these regions are in aromatic ring form. It is observed from **Table 3.2** that FWHM(G) and I_D/I_G ratio show reverse trends of evolution, which is completely different from the flat region. Hence, the sp^3 content evolution in the particulate region is also different from the flat region. The slight fall of sp^3 content for DLC-2 could be due to bigger size particulates than DLC-1.⁹³ To interpret the sp^3 content in details, UV-Raman study of particulate laden DLC films were carried out, which is presented in the succeeding section

3.3.4.2. UV Raman Analysis

The UV-Raman (325 nm) spectra obtained from flat and particulate regions of DLC-1, DLC-2, DLC-3, and DLC-4 films are background subtracted and deconvoluted into three Gaussian peaks such as G, D and T peak centered at 1580 cm^{-1} , ~ 1355 and 1060 cm^{-1} , respectively.⁹⁴

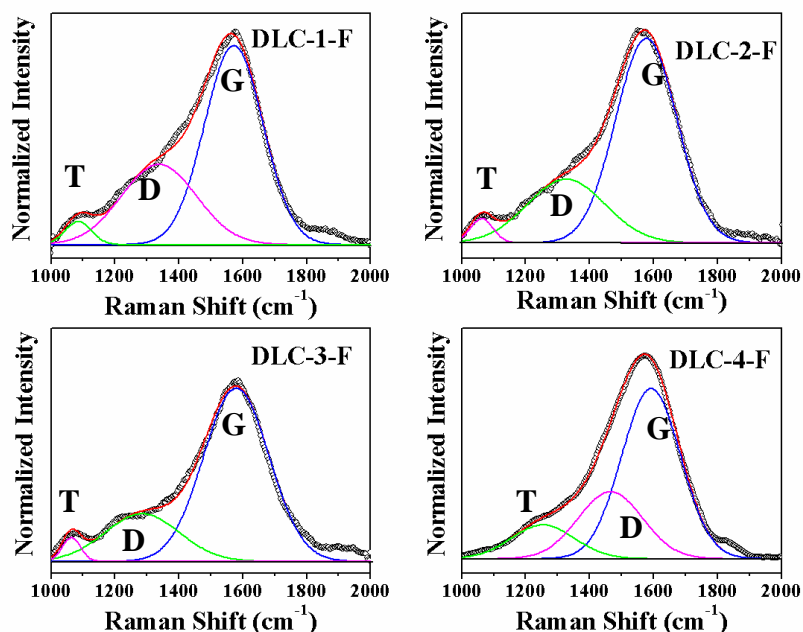


Figure 3.6. Deconvoluted UV (325 nm) Raman spectra obtained from flat region of (a) DLC-1, (b) DLC-2 (c) DLC-3, and (d) DLC - 4 films.

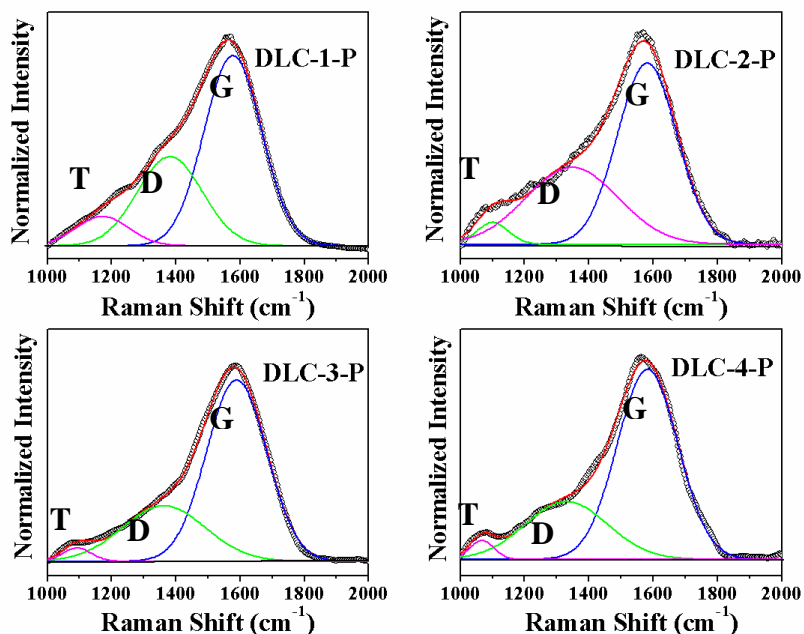


Figure 3.7. Deconvoluted UV (325 nm) Raman spectra obtained from particulate region of (a) DLC-1, (b) DLC-2 (c) DLC-3, and (d) DLC - 4 films.

Figure 3.6. and 3.7. represent the deconvoluted UV-Raman spectra for all particulate laden DLC films for flat and particulate regions respectively. As the laser light penetration depth for UV-Raman excitation is less, the corresponding T-peak is weak.¹⁰⁹ The T peak arises due to the C-C sp^3 vibrations.¹⁰³ **Table 3.3.** contains all the UV-Raman spectra deconvoluted parameters. The values of I_D / I_G and I_T / I_G are determined from the ratio of corresponding peak intensity.⁹⁴ The $\text{pos}^n(\text{G})$ at 514.5 nm for flat and particulate regions of particulate laden DLC films presented in **Table 3.1. and 3.2.** are used for the G peak dispersion ($\text{Disp}(\text{G})$) determination.

The G peak dispersion ($\text{Disp}(\text{G})$) is calculated from $\text{pos}^n(\text{G})$ at 325 nm and 514.5 nm using the following formula:^{106, 110}

$$\text{Disp}(\text{G}) = \left| \frac{\text{Pos}(\text{G})\lambda_2 - \text{Pos}(\text{G})\lambda_1}{\lambda_2 - \lambda_1} \right| \left[\text{cm}^{-1} / \text{nm} \right] \quad \text{..... (3.3)}$$

where λ_1 and λ_2 take values of 325 nm and 514.5 nm, respectively. The G peak dispersion is directly proportional to the degree of disorder of the sp^2 clustering.^{104, 109, 111} **Figure 3.8.** represents the evolution of $\text{Disp}(\text{G})$ with laser pulse energies on flat and particulate regions. It is clear from **Figure 3.8.** that both the regions show similar trend of evolution of $\text{Disp}(\text{G})$ with laser pulse energies. On the other hand, the $\text{Disp}(\text{G})$ value obtained from particulate region is less than the flat region, which indicates that sp^2 clusters of the particulate region are in less disorder state than the flat region. Hence, particulates are dominated by sp^2 clusters, which decrease its density. This may occur due to the higher stress developed in the flat region due to the interactions of the higher energetic carbon ions (lower mass) than the particulates (heavy mass).

**Table 3.3. Raman Deconvoluted Data obtained from Flat and Particulate region of DLC
DLC- 2, DLC-3, and DLC-4 for UV (325 nm) excitation.**

Specimen	G-Peak Pos ⁿ (cm ⁻¹)	D-Peak Pos ⁿ (cm ⁻¹)	T-Peak Pos ⁿ (cm ⁻¹)	I _D / I _G	I _T / I _G	FWHM(G) (cm ⁻¹)	Disp(G) (cm ⁻¹ /nm)
DLC – 1-F	1572	1338	1085	0.4	0.12	216	0.052
DLC – 2-F	1577	1327	1062	0.3	0.12	226	0.047
DLC – 3-F	1580	1285	1064	0.3	0.14	242	0.143
DLC – 4-F	1593	1465	1254	0.4	0.2	217	0.069
DLC –1-P	1577	1382	1171	0.5	0.16	211	0.127
DLC – 2-P	1582	1348	1100	0.4	0.12	219	0.132
DLC – 3-P	1589	1363	1092	0.3	0.08	220	0.18
DLC – 4-P	1583	1330	1067	0.3	0.1	223	0.164

In case of flat region of DLC-1 and DLC-2 show apparently identical Disp(G) values; this is less than the apparent identical values of DLC-3 and DLC-4 films. In other words it can be concluded that a transition in disorderness is observed at 300 mJ in the flat region, which remains constant for 400 mJ laser pulse energy. This result follows the subplantation model for DLC growth. It is also observed that in the particulate region the Disp(G) values of DLC-1, DLC-2, and DLC-4 are apparently constant and less than the value of DLC-3. In this study, the prominent transition in disorderness at 300 mJ and 400 mJ for flat and particulate regions can be attributed to the higher kinetic energy (K.E.) of carbon ions and structural modification of particulates in the plasma, respectively. At 400 mJ the Disp(G) value indicates that above the threshold laser pulse energy (300 mJ), the excess energy in the plasma is used for structural modifications of particulates, which dominates the higher K. E value.

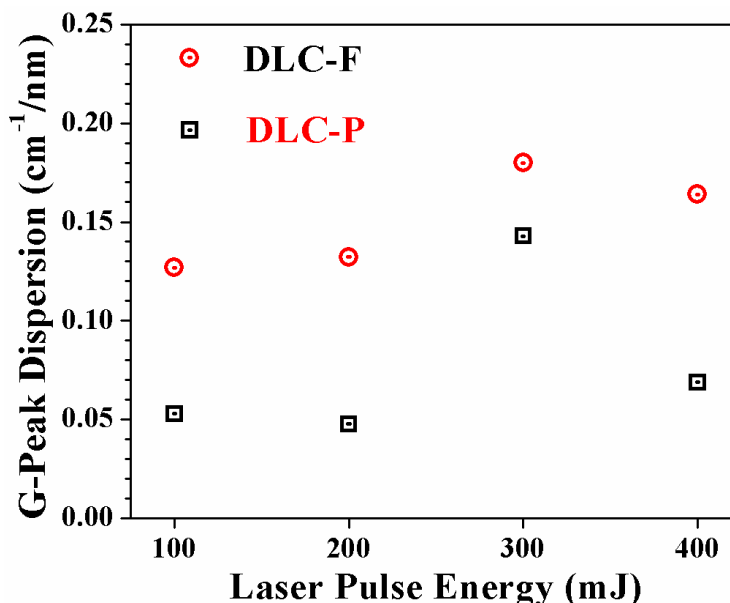


Figure 3.8. G-peak Dispersion vs laser pulse energy for flat and particulate regions.

The following sections contain a detailed comparative discussion on the evolutions of UV-Raman parameters (I_T/I_G , I_D/I_G , T-Peak position and FWHM(G)) as obtained from flat and particulate regions of particulate laden DLC films. The T-peak appears only in UV excitation due to the vibrations of c-c sp^3 bonding, which directly probes the sp^3 bonding.^{103,}
¹¹² According to Gilke *et. al.*, I_T/I_G determines sp^3 content directly in absence of D-Peak, whereas the presence of D-peak in UV Raman hinders the quantitative determination of sp^3 content.¹¹² In this case, the intensity of the D-peak dominates the T-peak intensity, henceforth in such situation I_T/I_G can be used for qualitative determination of the sp^3 content. In such cases, the intensity of D-peak depends more on order of sp^2 clusters than sp^2 fractions, such as the sp^2 sites in chains and with graphitic order leads to the absence of D-peak, whereas the sp^2 sites in disordered rings leads to the residual D peak survival in UV Raman spectra. In these cases interpretation of I_D/I_G , shifting of T-Peak position and FWHM(G) provide

additional information for sp^3 - sp^2 bond interactions in DLC such as the cluster size (number of aromatic rings), sp^3 content (sp^3 - sp^2 bond), bond length and angle disorder of sp^2 cluster, respectively.^{106, 109, 113}

From **Table 3.3.** the evolution of I_T/I_G and I_D/I_G with laser pulse energy in the flat and particulate regions of DLC films can be interpreted. I_D/I_G is a measure of sp^2 cluster size/number of aromatic rings in sp^2 clusters. According to Wasylok *et. al.*, sp^2 cluster size decreases with decrease in I_D/I_G .¹⁰⁹ It is clear from **Table 3.3.** that in the flat and particulate regions the cluster size (number of aromatic rings in sp^2 cluster) shows a transition at 300 mJ and 400 mJ irrespective of the nature of evolution. In the flat region the results can be explained on the basis of sub-plantation and thermal spike model, whereas on the particulate region, it can be attributed to the structural modification of particulate in the plasma due to the excess energy at 400 mJ.

Table 3.3. also depicts that in the flat region I_T/I_G rises with rise in laser pulse energy which is indicative of an increase in sp^3 content, whereas in case of particulate region it falls at 200 mJ and remains constant for higher laser pulse energies (300 and 400 mJ). This observation indicates that sp^3 content in the particulate region of DLC-2, DLC-3, and DLC-4 are almost constant and less than DLC-1. In the flat region, the observed result can be attributed to the DLC growth mechanism following sub plantation model, whereas in the particulate region it corresponds to the structural modification of the particulate in the plasma.⁹⁴ However evolution of T-peak position with laser pulse energy (reliable parameter in the presence of D-peak in UV Raman) will confirm the sp^3 content in flat and particulate region of all DLC films.

In **Table 3.3.** the evolution of T-peak position and FWHM(G) with laser pulse energy show reverse trend for flat and particulate regions, respectively. In the flat region, the T-peak position representing sp^3 content indicates that it decreases up to 300 mJ and shows a transition at 400 mJ, so sp^3 content increases up to 300 mJ and then decreases at 400 mJ. Similarly, the evolution of FWHM(G) shows an increase in bond length and angle disorder of sp^2 cluster up to 300 mJ and falls at 400 mJ in the flat region. In addition, the evolution of T-peak position and FWHM(G) with laser pulse energy in the particulate region indicates that the sp^3 content along with bond length and angle disorder of sp^2 cluster monotonically increase with laser pulse energy.

A detailed systematic analysis for various UV Raman parameters (I_D/I_G , I_T/I_G , T-Peak position and FWHM(G)) for flat and particulate region of all DLC specimens, it can be concluded as follows:-

- In the flat region: the evolution of sp^3 content, sp^2 cluster size, bond length and angle disorder of sp^2 cluster follow sub-plantation model up to 300 mJ. The transition observed at 400 mJ is attributed to the dissipation of the extra energy in the DLC matrix (Thermal spike model). According to thermal spike model the excess energy than the threshold energy promotes sp^2 clustering and hence size of ordered sp^2 clusters increases.
- In the particulate region, the evolution of sp^3 content, sp^2 cluster size, bond length and angle disorder of sp^2 cluster follow the structural modification of particulates in the plasma with laser pulse energy.
- Although sp^3 content increases with laser pulse energy for the particulate region, the disorderness and distortion in sp^2 cluster is relatively less than the

Flat region as observed from Disp(G) and FWHM(G), respectively. Hence, sp^3 content is more in the flat region than particulate regions.

3.4. Summary

The morphology of particulate laden DLC films studied by FESEM and AFM indicate that the number density and size of particulates on DLC surface increase with increase in laser pulse energy. Raman spectroscopy was implemented for vibrational investigations of particulate laden DLC films. The visible Raman I_D/I_G mapping on particulate laden DLC surfaces indicates variation in I_D/I_G value from particulate to flat surface, which is attributed to variation in compressive stress and corresponding densification leading to the formation of sp^3 bonds. Hence, qualitative studies of sp^3 content on flat and particulate regions were deduced from multi-excitation Raman spectroscopy. The evolution of sp^3 content on the flat surface of DLC films follows the sub-plantation model up to DLC-3 and fails for energies beyond it due to dissipation of extra energy on the DLC surface in the form of thermal energy. Whereas on the particulate region the evolution of sp^3 content, sp^2 cluster size, bond length and angle disorder of sp^2 cluster follow the structural evolution of particulates in the plasma plume with laser pulse energy. From above results, it can be concluded that the reason behind evolution of sp^3 content, sp^2 cluster size, bond length and angle disorder of sp^2 cluster with laser pulse energy on flat and particulate regions of DLC films are completely two different aspects.

CHAPTER 4

Influence of Particulates on Surface energy, Composition and mechanical Properties of DLC Films

“Crystals are like people, it is the defects in them which tend to make them interesting!”

Colin Humphreys

This chapter deals with the particulate influence on surface energy, composition and mechanical properties of particulate laden diamond-like carbon (DLC) films grown by pulsed laser deposition (PLD). Contact angle, XPS, AFAM and nano-indentation techniques have been used extensively for the characterization of DLC films.

4.1 Introduction

The ejection of particulates by Nd: YAG laser (1064 nm) during ablation is a common factor due to its higher wavelength, which penetrates more into the target surface.⁹⁴⁻⁹⁶ It is also found that as the pulse energy goes on increasing, the number density and size of particulates increase on DLC surfaces. As a result, the morphology and vibrational properties of DLC films gets modified, as discussed in chapter -3.^{61- 63} It is also discussed that visible (514.5 nm) and UV (325 nm) Raman study on flat and particulate regions of DLC films grown at various laser pulse energy follow two different kinds of growth mechanisms. Visible and UV Raman study on the flat surface of DLC films depict that the evolution of sp^3 content with laser pulse energy follows sub-plantation model up to 300 mJ and above it sp^2 clustering takes place due to dissipation of extra energy in DLC matrix as thermal energy. Ruiz *et.al.* has also reported similar results.⁹³ In addition, visible and UV Raman study on particulate

region of DLC films predicted that the evolution of sp^3 content, sp^2 cluster size, bond length and angle disorder of sp^2 cluster follow the evolution of structural and vibrational modification of particulates in the plasma plume. The visible Raman I_D/I_G mapping on DLC surfaces including particulates indicate variations in I_D/I_G value obtained from particulate to flat surface, which is attributed to the variation in compressive stress and corresponding densification leading to the formation of sp^3 bonds. It is reported that the features like; (a) sp^3 content, (b) sp^2 cluster phase, (c) sp^2 cluster size, (d) number density of sp^2 cluster, (e) sp^2 cluster phase orientation and (f) any cross-sectional structure influence the DLC properties due to interaction among sp^2 and sp^3 bonded carbon atoms.^{93, 103, 104} In the light of above discussion, a fundamental understanding of the influence of particulates on surface energy, composition and mechanical properties of particulate laden DLC films is highly essential. This issue has been taken up in the present chapter.

The present chapter describes AFAM measurements on the DLC surfaces to determine the relativistic stiffness on flat and particulate regions using the point spectroscopy method. In addition, surface energy, composition and mechanical properties of the DLC films are also determined using contact angle measurement, XPS and nanoindentation techniques, respectively.

4.2. Characterizations

The particulate laden DLC specimens grown by Nd: YAG laser at four different laser pulse energies are labeled as DLC-1, DLC-2, DLC-3, and DLC-4. The details of characterization procedures and conditions for investigation of surface energy, composition and mechanical properties of the particulate laden DLC films are discussed in the corresponding sections of chapter-2.^{61, 63}

4.3. Results and Discussion

4.3.1. Surface Energy determination

The surface energy can be obtained from contact angle (CA) measurement by establishing the tangent angle of a sessile liquid drop on the solid surface. The surface energy affects adhesion and wettability like surface related processes.¹¹⁴⁻¹¹⁶ The mechanical equilibrium of the drop should be maintained under the action of three interfacial tension solid-vapor (γ_{SV}), solid-liquid (γ_{SL}) and liquid-vapor (γ_{LV}). The evaluation is done using the computer with integrated software. The contact angle and surface free energy of a solid and liquid interface are related as follows⁹⁰:-

$$\gamma_{SV} - \gamma_{SL} = \gamma_{LV} \cos \theta \quad \dots\dots\dots (4.1)$$

where, γ_{SV} and γ_{LV} are the solid/vapor and liquid/vapor surface energy, respectively; γ_{SL} stands for the solid/liquid interfacial energy and θ is the contact angle. In the above mentioned equation the contact angle (θ) and the solid/liquid surface energy (γ_{SL}) are the measurable parameters. In principle, at least two equations need to be solved in order to determine two unknown parameters. This requires the use of two liquids with known total surface energies (γ_{LV}) and their dispersive (γ^d_{LV}) and polar (γ^p_{LV}) components. In this study, two liquids such as:- demineralised water (polar) and diiodo-methane (non-polar) liquids have been used at 25 °C to serve the purpose. Although, several theoretical models are available to determine the surface energy of the DLC films through the measurement of the contact angle in terms of interfacial energy γ_{SL} (f (γ_{SV} , γ_{LV})), but their results are qualitatively same for a specific selected combination of material and liquid.¹¹⁷ In this report we used the Owens–Wendt–Rabel–Kaelble (OWRK) model (**Eq. (4.2)**) (most frequently used model in

literature) for the determination of surface energy determination of particulate laden DLC specimens, ^{63, 117, 118}

$$(1 + \cos\theta)\gamma_L = 2 \left(\sqrt{\gamma_{SL}^d \gamma_{LV}^d} + \sqrt{\gamma_{SL}^p \gamma_{LV}^p} \right) \quad \dots \dots \dots (4.2)$$

Where, γ_L = total surface tension (mN/m)

γ_{LV}^d = dispersive component of surface tension (mN/m)

γ_{LV}^p = polar component of surface tension (mN/m)

γ_{SL}^d = dispersive component of surface energy (mJ/m²)

γ_{SL}^p = polar component of surface energy (mJ/m²)

γ_{SL} = total surface energy (mJ/m²)

It is reported in literature that a higher CA corresponds to a lower surface energy pertaining to a hydrophobic surface.^{119, 120} The dangling bonds available on the film surface influence the surface energy of a film, such as the film surface with less number of dangling bonds possesses lower surface energy.

Figure 4.1. represents the evolution of polar (P-SE (γ_{SL}^p)), dispersive (D-SE (γ_{SL}^d)), total surface energy (SE (γ_{SL})) and contact angles of particulate laden DLC surfaces with laser pulse energies for water (W-CA) and diodo-methane (DM-CA).⁶³ **Figure 4.1.** indicates that the polar component of surface energy (P-SE (γ_{SL}^p)) on the DLC surfaces dominates the total surface energy (SE (γ_{SL})). In addition, it is observed that the dispersive surface energy (D-SE (γ_{SL}^d)) and diodo-methane (DM-CA) contact angle show a transition at 200 mJ, which remains constant for higher laser pulse energies. Similarly, water contact angle (W-CA), polar (P-SE (γ_{SL}^p)) and total surface energy (SE (γ_{SL})) show a transition at 400 mJ. The

observed transitions for diodo-methane (DM-CA) and water (W-CA) contact angle are similar to the transition of I_T/I_G and I_D/I_G on particulate region (**Table 3.3.**) of particulate laden DLC films, respectively. These results indicate that dispersive (D-SE (γ_{SL}^d)) and polar (P-SE (γ_{SL}^p)) surface energies of particulate laden DLC films are affected by sp^3 content and sp^2 cluster size present in the particulates, respectively. Hence, it can be concluded that the particulates on the DLC film surfaces directly influence the surface energies of DLC films.

Litreature reports indicate that, the sp^2 -rich carbon surface reveals a larger CA than sp^3 -rich carbon surface,¹²⁰⁻¹²² such as the contact angle value of graphite (78°) is higher than natural diamond (35°).¹²³ The hydrophobicity of the graphite surface due to lower surface energy of graphite planes is attributed to the absence of dangling bonds on the surface.¹²³

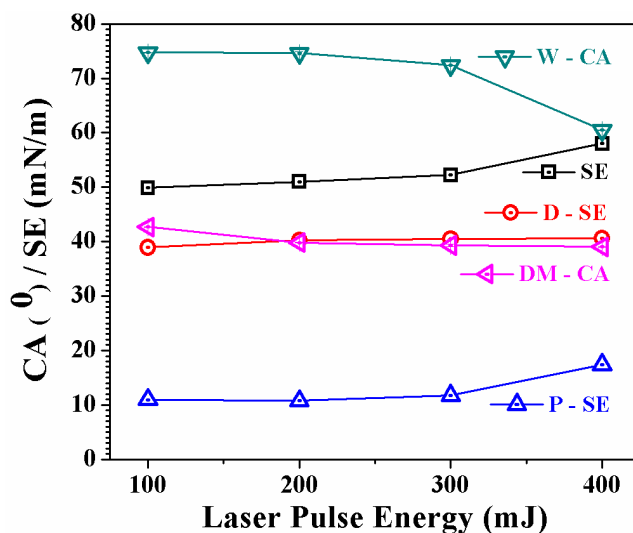


Figure 4.1. Evolution of surface energy polar (P-SE), dispersive (D-SE) and total (SE) and contact angle (water (W-CA) and diodo-methane (DM-CA)) of DLC specimens with laser pulse energy.

In the present study, it is noticed that the evolution of total surface energy (SE (γ_{SL})) of particulate laden DLC films with laser pulse energy follows the reverse trend of (I_D/I_G)

obtained from particulate region. This observation indicates that particulates with highest sp^3 content and sp^2 cluster of smallest size, higher bond length and angle disorder in DLC-4 film generates maximum surface energy.

4.3.2. Compositional Analysis

In order to obtain the sp^3 content of the particulate laden DLC films, XPS investigation were carried out. The C1s XPS peaks were de-convoluted into three distinct Gaussian–Lorentzian peaks after shirley background correction (**Figure 4.2. (a-d)**) to estimate the sp^3 , sp^2 and C–O bonding contents in the particulate laden DLC films.⁶¹ The three peaks observed at 284.4 ± 0.1 eV, 285.2 ± 0.1 eV and 286.2 ± 0.1 eV as shown in **Figure 4.2. (a-d)** correspond to sp^2 , sp^3 hybridized state of carbon atoms and C–O (or C=O) bonding, respectively.¹²⁴

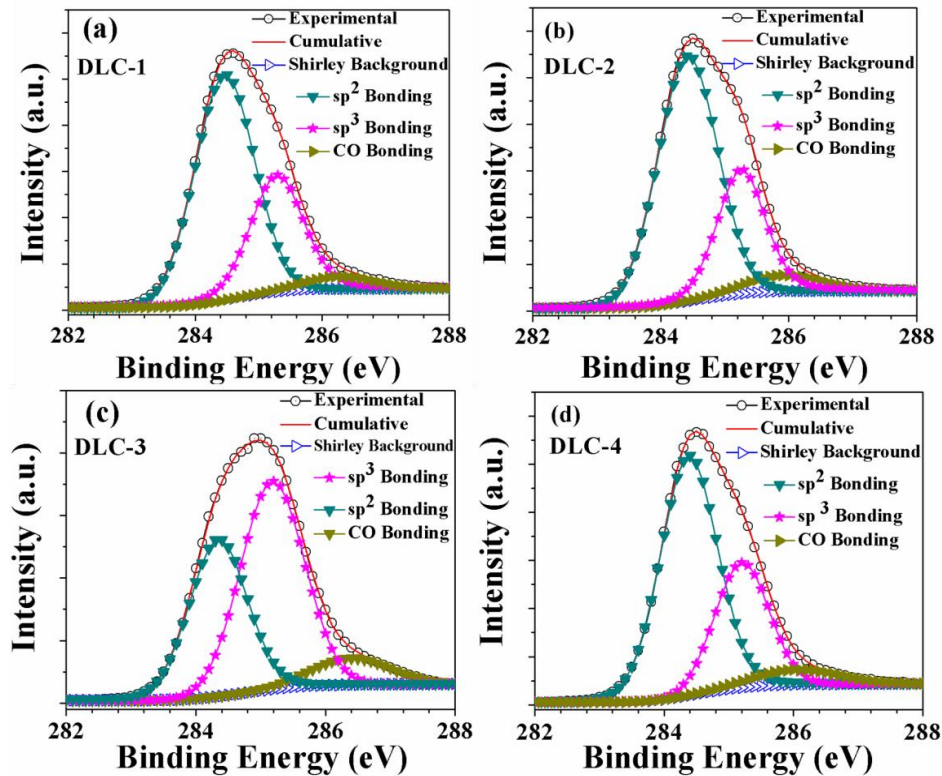


Figure 4.2. Deconvoluted XPS C1s peak of (a) DLC-1, (b) DLC-2, (c) DLC-3, and (d) DLC-4.

The presence of C–O (or C=O) is due to the exposure of the specimen surfaces to the ambient environment.¹²⁵ The sp^2 and sp^3 fractions of DLC films are determined from the ratio of the corresponding peak area to the total C1s peak area and tabulated in **Table 4.1**.⁶¹ The relatively low sp^3 content of the coatings found in this study indicates the growth of graphitic films and availability of particulates emitted during laser ablation by a 1064 nm Nd: YAG laser. The highest sp^3 content (53.5%) of DLC-3 films declares 300 mJ laser pulse energy ($8.57 \times 10^8 \text{ W} \times \text{cm}^{-2}$ laser fluence) as the threshold energy for DLC film growth. This threshold value is similar to the threshold laser fluence value ($7.03 \times 10^8 \text{ W/cm}^2$) obtained by Tabbal *et. al.*.¹⁵

Table 4.1. XPS C 1s spectra de convolution results of particulate laden DLC films synthesized at various laser pulse energies.

Specimen Name	sp^3 Band Position (eV)	sp^3 FWHM (eV)	sp^2 Band Position (eV)	sp^2 FWHM (eV)	sp^3 (%)	sp^2 (%)
DLC-1	285.3	0.98	284.5	1.1	32.3	63.7
DLC-2	285.2	0.88	284.4	1.1	29.1	65.4
DLC-3	285.2	1.1	284.3	1.0	53.5	38.5
DLC-4	285.2	0.98	284.4	1.0	30.5	63.9

Table 4.1., indicates that DLC-1 and DLC-2 specimens possess higher sp^2 phase fraction. This can be attributed to the less densification on DLC surfaces due to less kinetic energy of carbon ions in the plasma than the threshold energy. However in DLC-3 specimen, the sp^2 content shows a great fall to 38.5% and rise of sp^3 to 53.5%. The sp^3 content value in

DLC-4 specimen is similar to that of DLC-1 and DLC-2 specimens. This result can be attributed to the dissipation of the extra energy to the threshold energy in the DLC matrix as thermal energy, which enhances the sp^2 clustering.

In addition, from the literature survey on PLD grown DLC films it is observed that the charge state and kinetic energy of carbon ions in the plasma plume determine the carbon coordination in DLC films.^{14, 126} The unexpected increase in sp^3 content for DLC-3 specimen can be explained on the basis of sub-plantation model as discussed in Chapter-3.⁶¹ According to this theory, higher kinetic energy of carbon ions in the plasma penetrate deeper into the thin film surface and leads film densification with substantially higher sp^3 content.¹²⁷ In this study, the lower sp^3 content value for DLC-1 and DLC-2 specimens can be attributed to the less densification of film due to lower energetic carbon ions in the plasma plume, which sticks to the surface without penetrating into the film thereby contribute more sp^2 bonding on the film surfaces. On the other hand, DLC-4 specimen deposited at highest laser pulse energy shows similar sp^3 -content to that of DLC-1 and DLC-2 specimens. This observation indicates that it does not follow the sub-plantation theory.^{61, 126} Hence, it can be concluded that the total kinetic energy of carbon ions in DLC-4 corresponding to laser fluence $1.14 \times 10^9 \text{ W/cm}^2$ is not completely used for subsurface implantation of the carbon ions in the DLC film as in case of DLC-3. A fraction of the kinetic energy of carbon ions is used for local heating due to dissipation of excess energy in the DLC matrix, following the thermal spike model leading to sp^2 clustering.^{15, 93} Another fact is that at higher laser pulse energies the more particulate generation takes place, which hinders evolution of sp^3 phase as the graphitic matrix is retained as sp^2 phase on the film surface.¹²⁷ Hence, it can be concluded that both the above mentioned phenomena have synergetic effect on the DLC film deposition at 400 mJ. In this

study, the XPS results are in concurrent with qualitative compositional analysis on flat and particulate regions of DLC films by multi excitation Raman spectroscopy as discussed in chapter-3.

4.3.3. Determination of relative stiffness constant

The detailed procedure for elasticity mapping of DLC films using AFAM has been discussed in Chapter-2.⁶¹ In the present study Si (111) is used as reference and AFAM mapping was carried out on it prior to the experiment on particulate laden DLC films. **Figure 4.3. (a-e)** represent the AFM morphology and AFAM image (Mag) of Si (111), DLC-1, DLC-2, DLC-3 and DLC-4 specimens, respectively.⁶¹

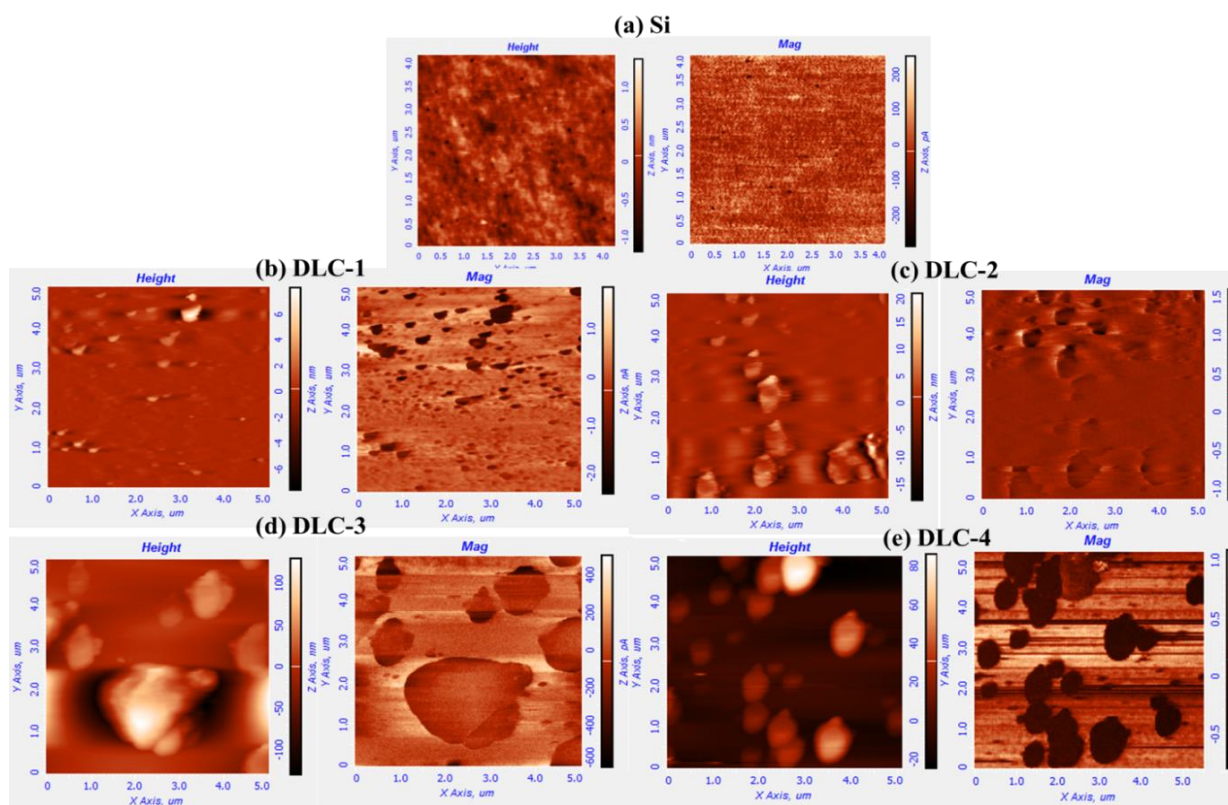


Figure 4.3. AFM topography and AFAM (Mag) images (a) Si (111), (b) DLC-1, (c) DLC-2, (d) DLC-3, and (e) DLC-4 films.

The magnitude variation is reflected as dark and bright regions in **Figure 4.3. (a-e)**.⁶¹ The distinct variation in the Mag image is mainly due to different kinds of particulate regions with different mass, size and shape distribution on the DLC film surface. This can be attributed to the variation in elasticity among different particulate regions due to various nano- structures entrained within them. The purpose of this study is to determine surface elastic forces on flat surface and particulate region of particulate laden DLC films. The AFAM formalism to differentiate soft and hard region depending on the operating frequency in terms of color is already discussed in chapter-2. The numerical equations for the estimation of stiffness (K^*) of the coupled oscillator system is also mentioned in **eqⁿ (2.2 and 2.3)** in chapter-2.

Mag image of **Figure 4.3. (a-e)** represents elasticity contrast, where the softer regions are dark and the stiffer regions are bright. The contrasting features in Mag image of **Figure 4.3. (b)** for DLC-1 specimen reveal that smaller particulates and bigger particulate regions show contrasts due to distinct relative stiffness values. This can be assigned to the variation in densities and entrained subspecies. Thus, AFAM image can provide information even on very small variation in mechanical properties within local areas. Mag image of DLC-2 specimen shown in **Figure 4.3. (c)**, indicates that DLC-2 possess softer regions than DLC-1, which can be attributed to the bigger size particulates at higher laser pulse energy. **Figure 4.3. (d) and (e)** indicate the presence of larger extent of soft zones with higher number density, whereas DLC-4 possesses more number of soft zones than DLC-3.

Now the influence of particulates on relative stiffness constant of particulate laden DLC films will be discussed. The contact resonance frequency of the reference Si (111) with known elastic constants and Poisson ratio was measured prior to the measurements on the

particulate laden DLC specimens, using point spectroscopy method to avoid hindrances in set values during measurement of contact resonance frequency. We followed the above mentioned method to avoid any hindrance in relative stiffness determination due to the presence of particulates in DLC films. The mathematical expression used for measuring for the contact resonance frequency of the coupled oscillator system is given by eqⁿ (4.3),^{61, 80, 83}

$$f = f_0 \sqrt{\frac{K^* + K_c}{K_c}} \quad \dots\dots\dots (4.3)$$

where f_0 is free oscillation frequency of the cantilever, K^* and K_c are stiffness of coupled oscillator system and the tip, respectively. The relative stiffness of DLC-1, DLC-2, DLC-3, and DLC-4 specimens with respect to Si (111) was estimated from the contact resonance frequency of cantilever.

Table 4.2. Contact resonance and relative stiffness value of particulate laden DLC films.			
Specimen	Selected Region	Relative stiffness	Resonance frequency shift (kHz)
Si	-	1.02	1025.8
DLC-100	Flat	1.8	1116.1
	Particulate	2.3	1120
DLC-200	Flat	2.2	1108.74
	Particulate	1.7	1093.05
DLC-300	Flat	4.6	1165.0
	Particulate	1.0	967.43
DLC-400	Flat	0.5	957.13
	Particulate	0.4	953.0

The contact resonance frequency on various regions of particulate laden DLC films was measured each time after calibrating the cantilever with respect to Si (111). These estimated relative stiffness values are listed in **Table 4.2.**⁶¹ The relative stiffness and contact resonance frequency of each film have been determined with respect to reference specimen Si (111). **Table 4.2.** depicts the difference in relative stiffness values on particulate regions and flat regions of particulate laden DLC films. The tabulated relative stiffness values on flat region of all DLC films except DLC-4 specimen has a higher value than that of Si (1.02). It is observed that flat region of DLC-3 possesses the maximum relative stiffness (< 4.6) value; this is 4.5 times higher than that of Si (111). The particulate regions (2.3) of DLC-1 exhibit higher relative stiffness than that of flat region (1.8); this is nearly double with respect to Si. It is also observed that the flat region (2.2) of DLC-2 specimens possess higher relative stiffness value than the particulate region (1.7). Again the flat and particulate region of DLC-4 indicates lower relative stiffness value as compared to Si. These results can be attributed to the presence of bigger particulates resulting in high density of defects as reported by Mangamma *et. al.*⁸³ In general, particulates are mostly composed of loosely packed sp^2 clusters with various disorders which make it softer than the flat region of the DLC specimens. In addition, the density variation of particulate also influences its stiffness. It is observed that, as the particulate size increases from DLC-1 to DLC-4, the measured relative stiffness decreases in the similar trend indicating the decrease of density. AFAM results of DLC films are similar to that of Raman mapping data discussed in chapter-3.⁶¹ Relative stiffness of particulate and flat regions can be explained on the basis of aromaticity of sp^2 bonded carbons, cluster size, sp^3 content and density, as supported by Raman mapping, multi-excitation Raman spectroscopy and XPS studies. It is observed that the thickness of

DLC film increases with increase in laser pulse energy, which in turn increases the density of DLC films, which increases stiffness with laser pulse energy.¹⁰¹ However, AFAM study of flat surface of DLC films reveals that the relative stiffness increases up to 300 mJ and above this, it shows a decrease. XPS study also shows that DLC-3 specimen has highest sp^3 content (53%) and DLC-4 film having 30% sp^3 content shows a deviation from sub-plantation model. In addition, the evolution of I_D/I_G ratio (chain type/aromatic rings) and shift in G-peak position (cluster size) with laser pulse energy as discussed in chapter-3, follow the similar trend in line with the findings from AFAM and XPS.^{61, 63}

Figure 3.7. reveals that, the I_D/I_G ratio mapping for all DLC specimens, except DLC-4, follow the sub-plantation theory.¹²⁶ In addition, except DLC-1 specimen all others possess higher I_D/I_G ratio for particulate region than flat surface. This result is in concurrent with the AFAM result that particulate regions of DLC-1 specimen are stiffer than its flat surface, whereas the flat surfaces of other specimens are stiffer than their particulate regions. This result can be attributed to the synergetic effect of density (size dependent), entrained substructures (clusters) and disorderness (chain type or aromatic rings of sp^2 cluster) within

The stiffness depends on the fraction of C–C sp^3 sites, since only the sp^3 sites contribute significantly to the hard zones. Hence, higher C–C sp^3 fraction in DLC makes the material with superior mechanical properties as revealed by XPS, Raman spectroscopic and AFAM studies. Both density and stiffness of films can be explained in terms of phase fraction of sp^3 bonding, size and aromaticity of sp^2 clusters.

4.3.4. Nano-Indentation Hardness and Elastic Constant determination

A number of studies on evolution of hardness with penetration depth are available in literature to explain the sub-plantation model for DLC growth.^{128, 129} In this study, nano-

indentation is performed on particulate laden DLC films as a function of penetration depth (P_d) (10 nm to 85 nm) at different linear load to understand the deformation behavior of particulate laden DLC specimens.

The evolution of indentation hardness (H) and the indentation modulus (E) of Si (111) substrate and particulate laden DLC films (DLC-1, DLC-2, DLC-3 and DLC-4) with penetration depth (P_d) are shown in **Figure 4.4.** and **Figure 4.5.**⁶³ respectively for the sub layer mechanical information,. It is observed that the H and E value of Si (111) remain constant throughout the penetration depth (P_d) at around 14 and 200 GPa, respectively. In this case, the Si (111) substrate is softer than particulate laden DLC films. The indentation hardness (H) of all particulate laden DLC films increases up to ~20 nm indentation depth and after that decreases with the increase in penetration depth (P_d) due to the substrate effect. Similarly, the indentation modulus (E) values of all particulate laden DLC specimens except DLC-3 decreases with increase in indentation depth (P_d). The indentation hardness (H) and modulus (E) should be determined without substrate effect by performing the nano-indentation at penetration depth (P_d) below the one-tenth ($1/10^{\text{th}}$) of the total film thickness.¹³⁰

In this study, particulate laden DLC specimens are harder than Si (111) substrates, therefore according to one-tenth ($1/10^{\text{th}}$) depth rule penetration depth (15 - 20 nm) at 0.3 mN applied indentation load is considered for estimation of H and E values of particulate laden DLC films. In general, H and E value of DLC films mostly vary with $sp^3:sp^2$ bonding ratio.⁹⁴ The estimated H values at 0.3 mN applied indentation load for DLC-1, DLC-2, DLC-3, and DLC-4 specimens are 26, 30, 46, and 39 GPa, respectively. In addition, the determined E values at 0.3 mN applied indentation load for DLC-1, DLC-2, DLC-3, and DLC-4 specimens are 220,

270, 340, and 330 GPa, respectively. The mechanical parameters obtained at a depth of ~20 nm from the indentation experiment are plotted in **Figure 4.6.**⁶³

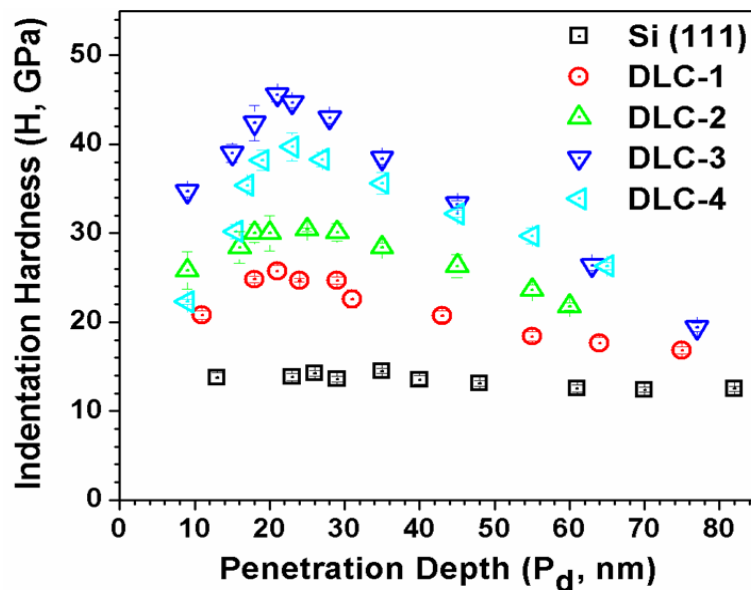


Figure 4.4. Indentation hardness as a function of penetration depth of Si (111) substrate and particulate laden DLC (DLC-1, DLC-2, DLC-3, and DLC-4) Films.

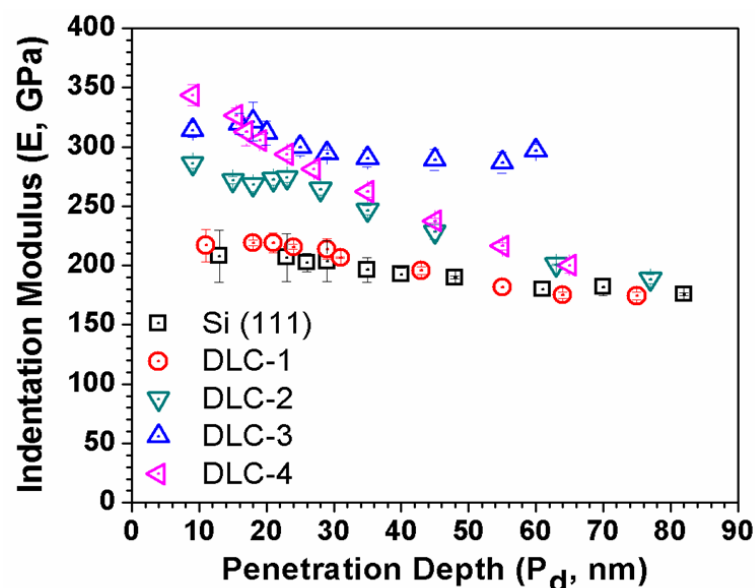


Figure 4.5. Indentation Modulus as a function of penetration depth of Si (111) substrate and particulate laden DLC (DLC-1, DLC-2, DLC-3, and DLC-4) films.

Figure 4.6. shows the evolution of H (GPa), E (GPa) values at ~ 20 nm penetration depth (P_d) and sp^3 content (XPS) of particulate laden DLC films grown at various laser pulse energies (100 – 400 mJ). It can be concluded that the H and E value of DLC film at ~ 20 nm penetration depth (P_d) follow the evolution of sp^3 content on flat region of DLC specimens. Again it is also observed that on the top surface (above ~ 20 nm penetration depth (P_d)), H value follows sp^3 content trend on flat region whereas E value follows the evolution of sp^2 cluster size, bond length, angle disorder of sp^2 cluster on particulate regions of DLC films as observed from UV-Raman study (presented in chapter-3).

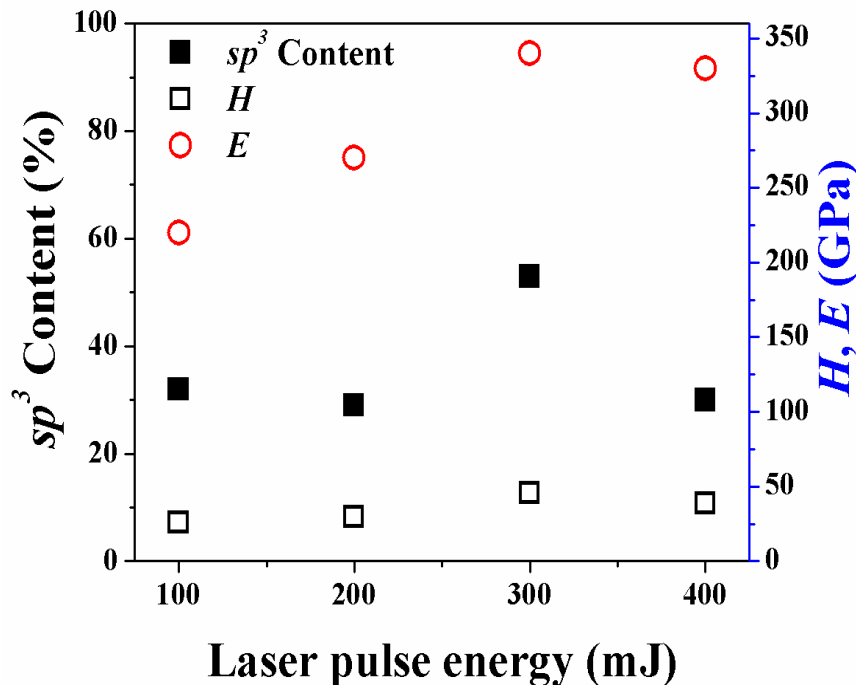


Figure 4.6. Evolution of H (GPa), E (GPa) values at 0.3 mN indentation load and sp^3 content of DLC-1, DLC-2, DLC-3, and DLC-4.

This observation concludes that H value is only dependent on sp^3 : sp^2 bonding ratio, This observation concludes that H value is only dependent on sp^3 : sp^2 bonding ratio, whereas

E value depends on all properties related to bonding including the $sp^3:sp^2$ bonding ratio. It is important to mention here that, the H and E value of DLC films above ~ 20 nm penetration depth (P_d) is not discussed much in the present study in order to avoid the substrate effect.

4.4. Summary

The evolution of surface energy with laser pulse energies and transition in contact angle at 400 mJ can be attributed to the sp^2 cluster size, sp^3 content, bond length and angle disorder of sp^2 clusters found in the particulate regions of the DLC films. The compositional analysis by XPS study revealed that DLC-3 possesses maximum sp^3 content ($\sim 53\%$), whereas other DLC films possess a sp^3 content of $\sim 30\%$. In this study, it is observed that the evolution of sp^3 content follows the sub-plantation model up to DLC-3 and fails for energies beyond it due to dissipation of extra energy on the DLC surface in the form of thermal energy causing sp^2 clustering. The relative stiffness constants of all particulate laden DLC films (except DLC-4) are higher than Si. This indicates that DLC-4 is very soft and DLC-3 exhibits maximum relative stiffness. The relative stiffness of DLC-3 is ~ 4.5 times higher than Si but with larger and very soft particulate regions. It is observed that 300 mJ laser pulse energy is the threshold energy to obtain highest relative stiffness due to maximum sp^3 content. In addition, DLC-3 film is found as the hardest film from nano-indentation study with indentation hardness (H) and indentation modulus (E) values as 46 and 340 GPa, respectively.

CHAPTER 5

Investigation of DLC-Au Nano-composite Films Grown by Excimer Laser Ablation

“Alone we can do so little; together we can do so much”

Helen Keller

This chapter starts with a discussion on advantages of diamond-like carbon (DLC)-metal nano-composites, followed by deposition of DLC-Au nano-composites films and investigation of its morphology, structure, composition and vibrational properties.

5.1. Introduction

Metal incorporation in DLC is preferable in order to achieve multifunctionality with enhanced quality of the coatings with respect to pure DLC films through modulation of its high intrinsic residual compressive stress.^{131, 132} The transition metal dopants like Ti, Cr, and W are mostly compliant in the DLC matrix through covalent bonds. These transition metal dopants accommodate the strain in carbon rigid network by distorting the electron clouds, since these elements can readily lose their valence electrons. Thus the metal nanoparticles in DLC based nano-composites can accommodate the huge compressive stress and enhance the adhesion strength of the specimen.¹³² The doping concentration and distribution of metals in DLC can alter the physical and mechanical properties to suit various optical, mechanical and tribological applications.¹³³⁻¹³⁶ One of the superior illustrations is DLC based Chameleon nano-composites (YSZ-Au-MoS₂-DLC) for tribology applications under diverse environmental conditions.^{4, 5, 60} This is a tribological coating with chameleon-like surface

adaptive behavior for potential applications in high temperature adaptive lubrication and contact thermal management. In this nano-composite, gold with amorphous yttrium stabilized zirconia (YSZ) in the form of binary nano-composite (YSZ-Au) hard coating is used as a component. The hardness value of YSZ-Au nano-composite is ~ 15 GPa with 20 atomic percent (at. %) of Au incorporation.⁴ The low value of hardness with high atomic % of Au in YSZ-Au binary nano-composite hard coating demands another binary nano-composite hard coating like DLC-Au, which can provide higher hardness value with low Au at.%. Although reports on un-hydrogenated DLC-gold (DLC-Au) nano-composite grown by PLD are readily available in literature,⁵⁶ its tribological property is not studied extensively. In view of this, the present chapter provides an investigation on morphology, structure, composition and vibrational properties of PLD grown un- hydrogenated DLC-Au nano-composite films prior to its tribological application.

5.2 Characterizations

The DLC-Au nano-composites specimens grown by Excimer laser at three different laser indexing angles are labeled as DLC–Au: 12%, DLC–Au: 7.3% and DLC–Au: 4.7% depending on the gold contents.⁶⁵ Morphology, structure, composition and vibrational properties of these films were determined using FESEM, AFM, XRD, TEM, XPS, EDS, EELS and Raman Spectroscopy, respectively.⁶⁵ The details of synthesis and characterization procedures and parameters are discussed in the corresponding sections of chapter-2.

5.3. Results and Discussion

5.3.1. Thickness of DLC-Au nano-composite films

The thickness of pure DLC and DLC-Au films were measured by profilometer and found as ~ 160 nm and ~ 100 nm, respectively. It is observed that pure DLC is thicker than

DLC-Au films for same laser pulse energy as well as number of shots due to the higher ablation rate of graphite target compared to the gold foil.⁶⁵

5.3.2. Morphological Analysis

5.3.2.1. FESEM Study

The FESEM micrographs of DLC and DLC-Au nano-composites are presented in **Figure 5.1. (a-d)**. It is observed from the **Figure 5.1. (a)** that, the DLC surface shows randomly distributed irregular shaped particles of various size distributed randomly throughout the matrix. These are particulates formed during synthesis.⁵⁶

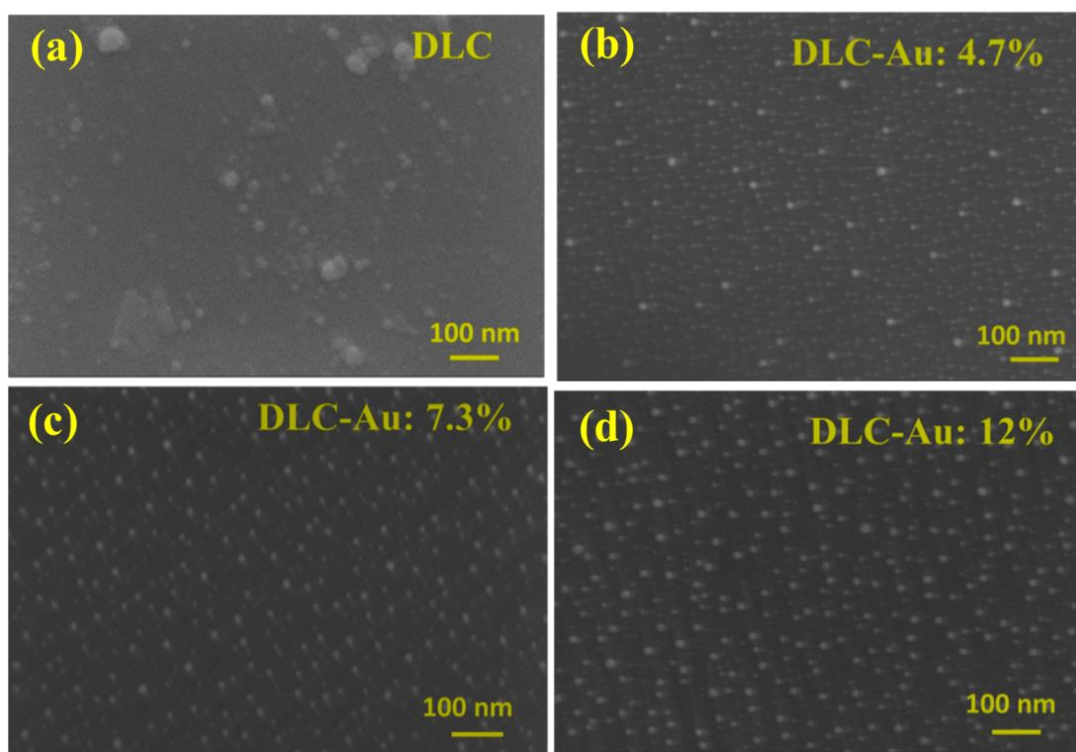


Figure 5.1. FESEM micrographs of (a) DLC, (b) DLC-Au: 4.7%, (c) DLC-Au: 7.3%, and (d) DLC-Au: 12% specimens.

Figure 5.1. (b-d) presents the morphology of DLC-Au nano-composites at various Au content. It is observed that the surface of DLC-Au nano-composites possess uniformly distributed round shaped Au nano-particles of average diameter 10 nm. The number density

of Au nano-particles increases with increase in Au content for obvious reasons. XPS analyses are carried out to obtain Au content as discussed in the succeeding text.

5.3.2.2. AFM Study

The morphology study on DLC and DLC-Au nano-composites is also carried out by AFM in support to FESEM study. **Figure 5.2.** (a-d) presents the AFM micrographs of DLC and DLC-Au nano-composites over $3 \times 3 \mu\text{m}^2$ scanned area.

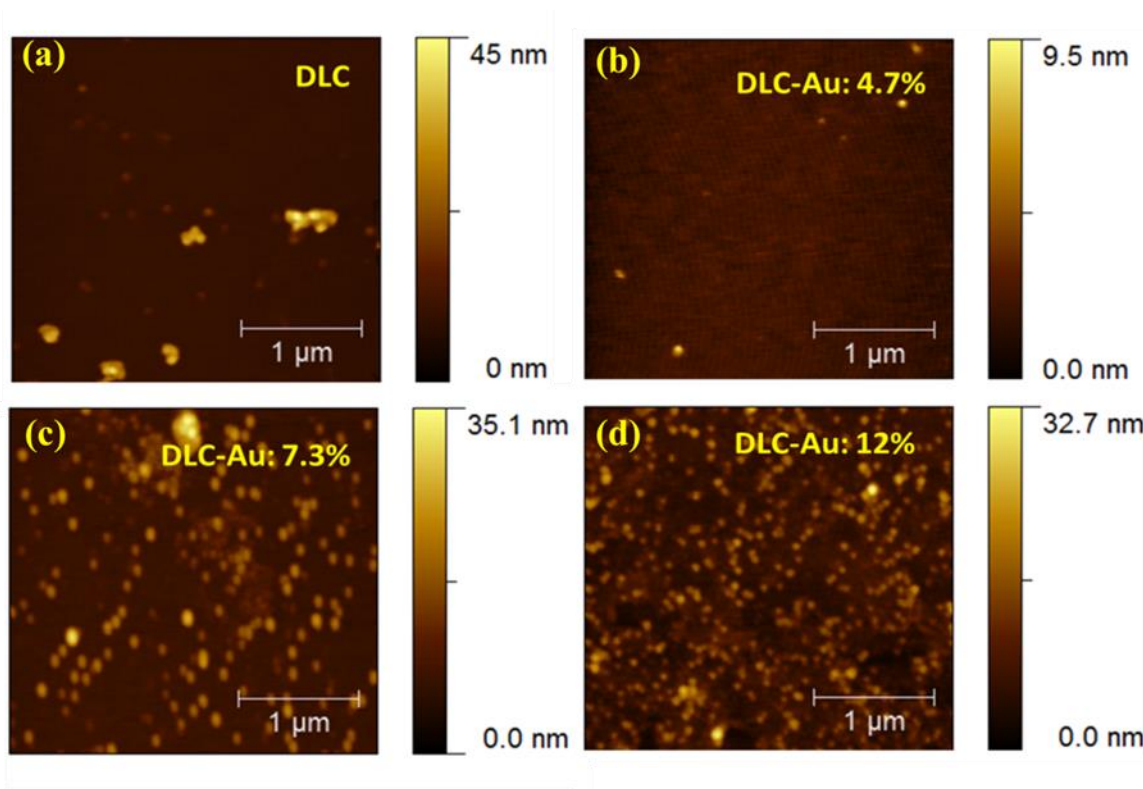


Figure 5.2. AFM micrographs of (a) DLC, (b) DLC-Au: 4.7%, (c) DLC-Au: 7.3%, and (d) DLC-Au: 12% specimens.

Figure 5.2. (a) indicates that DLC surface possess some small round shaped particles with a height ~ 20 nm and a few big irregular shaped particles with a height ~ 40 nm. These round and irregular particles can be assigned as the carbon nano-particles entrained with sp^2 clusters of various size and bond properties.⁵⁶

Figure 5.2. (b) shows a very smooth surface of DLC-Au: 4.7% specimens with few round shaped small nano- particles with a height ~ 9 nm. These small nano-particles may be carbon or Au nano-particles. In addition, **Figure 5.2. (c, d)** indicates that DLC-Au: 7.3% and DLC-Au: 12% show similar AFM heights but the number density of small round shaped nano-particles increases with increase in Au content. Hence it can be concluded that number density of Carbon and Au nano-particles increases with increase in Au content.

5.3.3. Structural Analysis

5.3.3.1. XRD Study

Figure 5.3. (a-d) presents the XRD pattern of DLC and DLC-Au nano-composites with pure gold (Au) film as reference, respectively.⁶⁵ The observed four diffraction peaks of Au at 2θ values of 38.2° , 44.5° , 64.9° and 74.9° correspond to (1 1 1), (2 0 0), (2 2 0) and (3 1 1) planes, respectively. These peaks with broad width indicate that the Au grains are in nano-

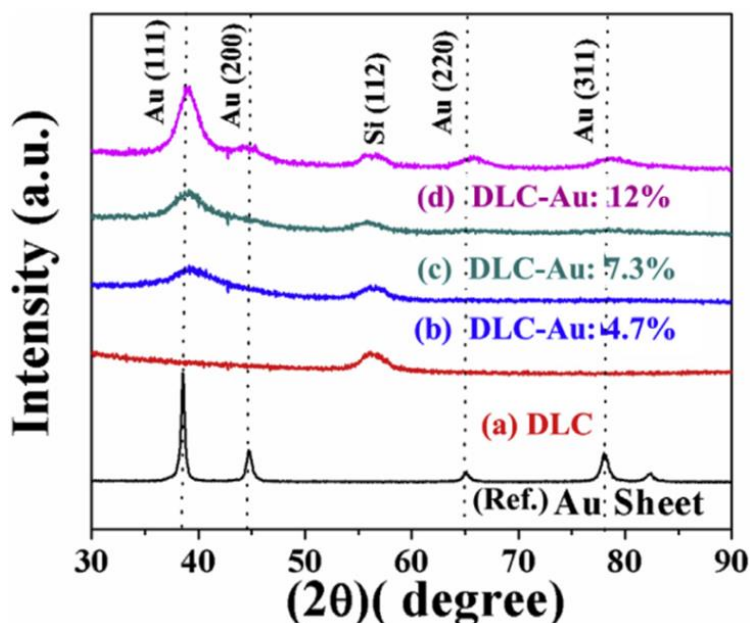


Figure 5.3. XRD patterns of (a) DLC, (b) DLC-Au: 4.7%, (c) DLC-Au: 7.3%, and (d) DLC-Au: 12% films.

crystalline form.^{65, 134} The peak at 56.4° corresponds to Si substrate. In **Figure 5.3. (d)**, the highest intensity and narrow FWHM of (111) peak predicts that DLC-Au: 12% possesses highest Au content with largest cluster. The FWHM of (111) peak for DLC-Au: 7.3% and DLC-Au: 4.7% increases indicating a decrease in crystallite size with decrease in gold content. The average crystallite size (d) is calculated from the FWHM of Au peaks.^{65, 134} The estimated crystallite size of DLC-Au: 12%, DLC-Au: 7.3%, and DLC-Au: 4.7% films are 3.3, 2.6 and 2.0 nm, respectively. The Au (111) peak also shows a shift towards higher 2θ value, which increases with decrease in Au content.⁶⁵

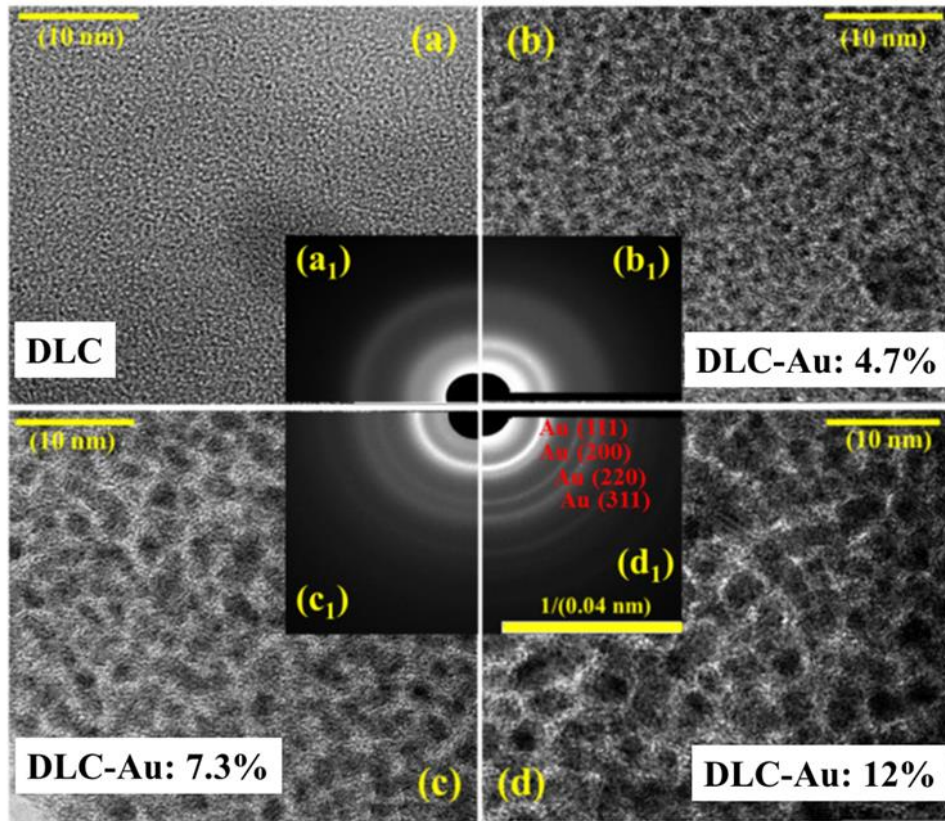


Figure 5.4. HRTEM micrographs of (a) DLC, (b) DLC-Au: 4.7% (c) DLC-Au: 7.3%, (d) DLC-Au: 12% films with corresponding diffraction patterns as insets (a₁, b₁, c₁, and d₁).

In this study, the reason for smaller Au crystallite size and higher Au (111) peak shift in DLC-Au: 4.7% can be attributed to the relatively higher residual stress of the DLC matrix experienced by the Au nano-clusters at lower Au content.⁶⁵ This result indicates that the interaction between Au and C atoms dominates over Au and Au atomic interaction, which results in a reduction in compressive stress of the film. It is interesting to note that, with increase in gold content, the gold cluster size also increases which is indicative of the dominance of Au - Au atomic interaction over Au - C atomic interaction.¹³⁷

5.3.3.2. TEM Investigation

The TEM micrographs of DLC and DLC-Au nano-composites films along with their electron diffraction pattern (as insets) are shown in **Figure 5.4. (a-d)**.⁶⁵ The diffraction patterns shown in **Figure 5.4. (b₁-d₁)** indicate faint rings for Au nano-crystallites with a halo inside arising from the DLC matrix (shown in **Figure 5.4. (a₁)**). The rings in DLC-Au: 12% corresponds to the Au planes as (1 1 1), (2 0 0), (2 2 0) and (3 3 1).^{138, 139} The rise in number and intensity of rings from DLC-Au: 4.7% to DLC-Au: 12%, indicates the appearance of new plane due to clustering of Au nano-crystallites with rise in gold content. **Figure 5.4. (d)** indicates clustering in the DLC matrix. This can be attributed to gold clustering (Au-Au interaction) at higher gold content, which induces clustering in the DLC matrix (C-C interaction). The estimated average Au crystallite size from HRTEM micrographs are 1.5, 2.5 and 3.3 nm for DLC-Au: 4.7%, DLC-Au: 7.3% and DLC-Au: 12% specimens, respectively. The observed results are consistent with the XRD measurements except for DLC-Au: 4.7%. The deviation observed in DLC-Au: 4.7% can be attributed to the neglecting of strain contribution during the estimation of crystallite size from XRD data. Therefore the TEM data is considered as more appropriate.⁶⁵

5.3.4. Compositional Analysis

5.3.4.1. XPS Study

A detailed compositional analysis of DLC and DLC-Au nano-composite specimens was carried out by XPS. The reported survey spectra clearly shows the photoelectron emission of C and O in DLC at ~ 285.0 eV and ~ 533.0 eV, respectively with additional lines corresponding to Au atoms.⁶² The 4f photoelectron emission line of Au is observed prominently. In addition, doublet at binding energy of 84.4 eV ($4f_{7/2}$) and 88.2 eV ($4f_{5/2}$) followed by 4d doublet at 335.8 eV ($4d_{5/2}$) and 353.8 eV ($4d_{3/2}$), and $4p_{3/2}$ at 546.7 eV of the 4p doublet for all DLC-Au nano-composites were also observed.¹⁴⁰ The presence of small and more or less same fraction of oxygen in all specimens is due to the contamination of the specimen surface through exposure to ambient environment. **Table 5.1.** lists the detailed elemental composition calculated from ratio of integrated intensity.⁶² The C1s XPS peaks were deconvoluted into five distinct Gaussian-Lorentzian peaks after Shirley background correction and presented in **Figure 5.5. (a-d)**. The sp^3 and sp^2 contents of DLC and DLC-Au nano-composite specimens obtained from **Figure 5.5. (a-d)** are also tabulated in **Table 5.1.**⁶⁵

Table 5.1. Atomic % of different elements, sp^3 , and sp^2 bonding content as obtained from XPS.

Specimen Name	C (%)	O ₂ (%)	Au (%)	sp^3 content (%)	sp^2 content (%)
DLC	94	6	0	31.6	55.5
DLC-Au: 12%	81.4	6.6	12	29.9	55.2
DLC-Au: 7.3%	86.9	5.8	7.3	37.8	49.7
DLC-Au: 4.7%	89.3	6	4.7	41.4	46.7

Table 5.1. depicts that DLC-Au: 12% specimen possesses highest gold (12 at %) while DLC-Au: 4.7% specimen possesses highest sp^3 content (41.4%) with lowest (4.7 at %) Au contents in DLC matrix. The order of Au content in DLC for indexing angles 10° (DLC-Au: 12%), 20° (DLC-Au: 7.3%) and 30° (DLC-Au: 4.7%) follows the fractions of the time (or laser shots) on Au segment to the graphite segment as 7:5, 1:2 and 5:13, respectively. The sp^3 content decreases with increase in gold content.⁶⁵

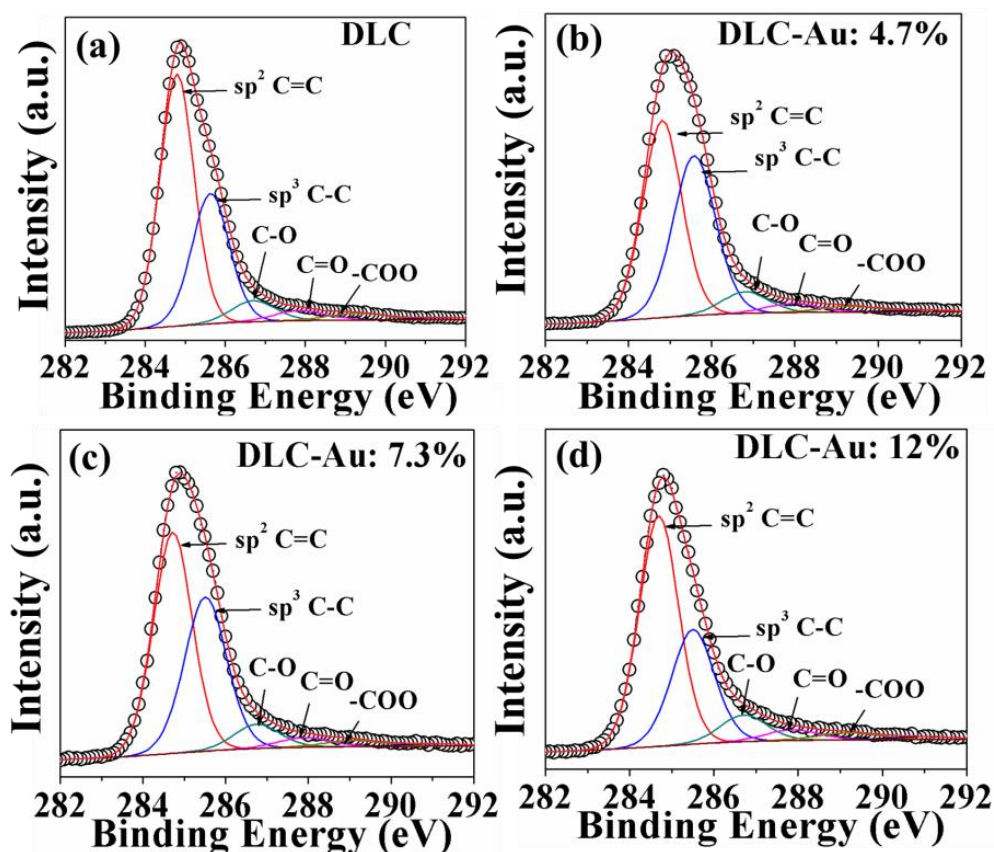


Figure 5.5. De-convoluted C 1s spectra of (a) DLC, (b) DLC-Au: 4.7% (c) DLC-Au: 7.3%, (d) DLC-Au: 12% specimens.

In DLC-Au: 12%, the sp^3 content is less than pure DLC. The lower value of sp^3 content in DLC, DLC-Au: 7.3% and DLC-Au: 12% indicate that, Au content (4.7 at %) in

DLC-Au: 4.7% specimen act as an optimum value for maximum Au-C interaction resulting highest sp^3 content.⁶⁵ Hence, C and Au atoms clustering dominate in DLC, DLC-Au: 7.3% and DLC-Au: 12% specimens due to dominance of Au-Au and C-C interactions over Au-C interaction.⁶⁵ This result demands further investigation of X-ray photoelectron emission lines of O 1s and Au 4f, which is discussed in the following paragraph.

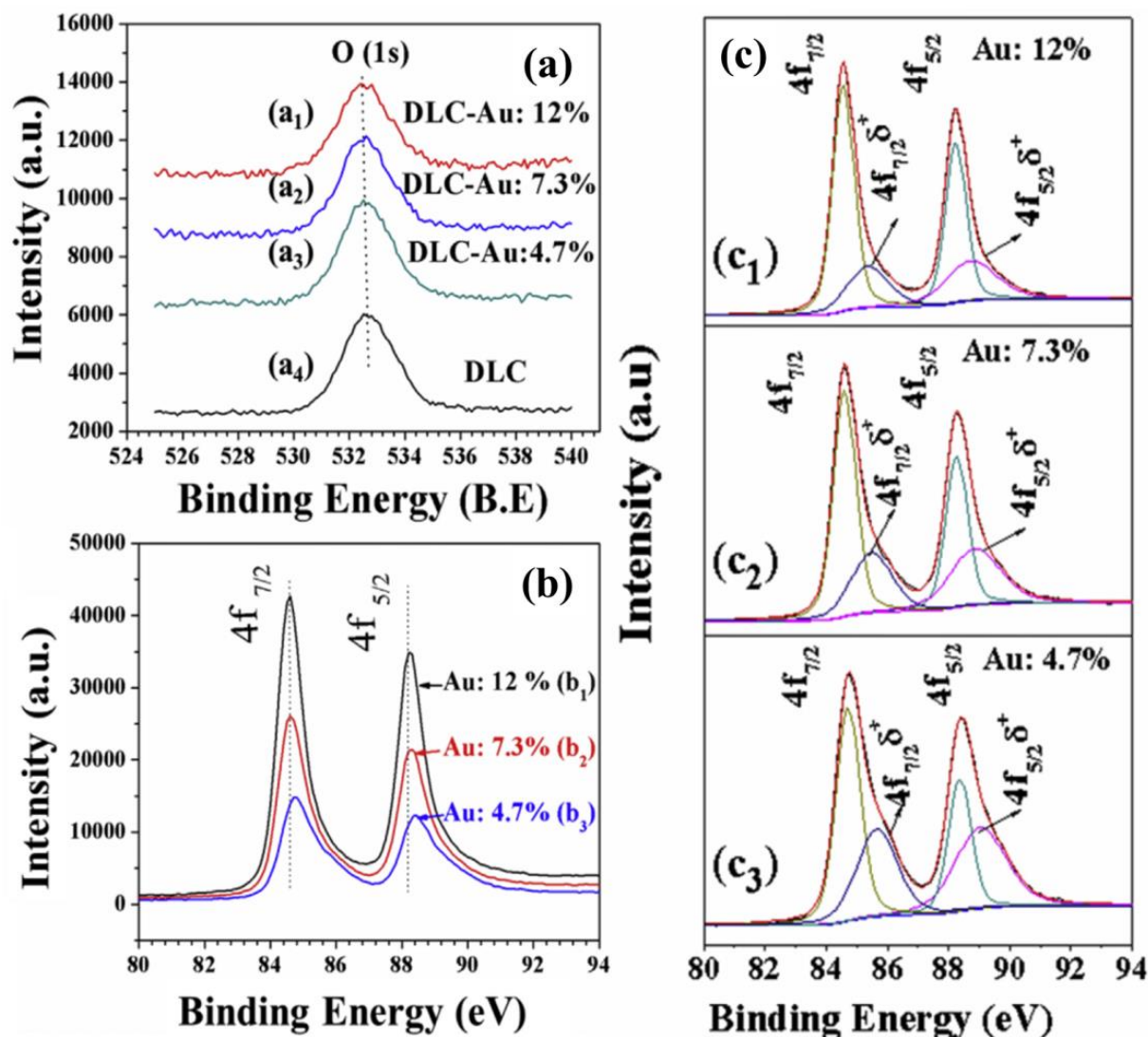


Figure 5.6. (a) O 1s X-ray photoelectron emission lines, (b) Au 4f X-ray photoelectron emission lines and (c) De-convoluted Au 4f X-ray photoelectron emission lines.

The X-ray photoelectron emission lines of O 1s and Au 4f are presented in **Figure 5.6. (a and b)** for the detailed investigation to observe the influence of DLC matrix and oxygen on Au. **Figure 5.6. (a₁-a₄)** shows no peak shift of O 1s indicating absence of Au influence on the oxidation state of oxygen in the DLC matrix. The peak position of O 1s at ~533.0 eV indicates the formation of -O-C- bonding due to adsorbed moisture. In addition, the possibility of Au-O- is also ruled out due to the symmetric O 1s peak occurrence at ~530.0 eV. **Figure 5.6. (b₁-b₃)** indicate a significant peak shift for Au 4f emission lines. It is observed that the decrease in Au content shifts the Au 4f peak towards higher binding energy indicating a decrease in Au cluster size.^{141, 142} This observation is also in concurrent with XRD and TEM analysis.⁶⁵ The observed binding energy shift of the cluster is due to coulomb charging as the photoelectron is emitted during the photoemission process.⁶⁵ In addition, **Figure 5.6. (c)** shows the prominent evolution of asymmetric peak for $4f_{7/2}^{+\delta}$ and $4f_{5/2}^{+\delta}$ with decrease in gold content. The Au 4f core-level spectra is de-convoluted by using two spin-orbit split as Au $4f_{7/2}$ and Au $4f_{5/2}$ components with a separation of 3.7 eV, in a fixed intensity ratio (1.33). The peak positions and full width at half-maximum (FWHM) values are reported in **Table 5.2**.

Table 5. 2. Peak position and FWHM of various Au state.

Specimen Name	Au $4f_{7/2}$ Peak Pos ⁿ (eV)	Au $4f_{7/2}$ FWHM (eV)	Au $4f_{7/2}^{+\delta}$ Peak Pos ⁿ (eV)	Au $4f_{7/2}^{+\delta}$ FWHM (eV)	Au $4f_{5/2}$ Peak Pos ⁿ (eV)	Au $4f_{5/2}$ FWHM (eV)	Au $4f_{5/2}^{+\delta}$ Peak Pos ⁿ (eV)	Au $4f_{5/2}^{+\delta}$ FWHM (eV)
DLC-Au: 12%	84.6	0.8	85.5	1.7	88.2	0.8	89	1.6
DLC-Au: 7.3%	84.6	0.9	85.5	1.7	88.2	0.9	89.2	1.5
DLC-Au: 4.7%	84.7	0.9	85.6	1.6	88.3	0.9	89.2	1.5

It indicates that Au $4f_{7/2}$ component at $BE=84.6 \pm 0.1$ and Au $4f_{7/2}^{+\delta}$ component at $BE=85.5 \pm 0.1$ eV, similarly Au $4f_{5/2}$ component at $BE=88.2 \pm 0.1$ and Au $4f_{5/2}^{+\delta}$ component at $BE=89.1 \pm 0.1$ eV which can be assigned to Au^0 and Au^{+1} species, respectively.^{143, 144} In this study, the evolution of area under peaks for $4f_{7/2}^{+\delta}$ and $4f_{5/2}^{+\delta}$ with gold cluster size/content in the DLC matrix (**Figure 5.6. (c)**) justifies the origin of Au^{+1} species, which can be attributed to the interaction between gold atom and DLC matrix (Au-C interaction). Whereas, the lower binding energy component corresponds to the interaction among gold atoms (Au-Au interaction). The decrease of $4f_{7/2}^{+\delta}$ and $4f_{5/2}^{+\delta}$ species content in DLC-Au nano-composites with increase in gold contents (**Figure 5.6. (c)**) indicates that interaction among gold atoms (Au-Au) dominates at higher gold contents leading towards the formation of pure metallic Au.⁶⁵ At lower gold content, the smaller gold cluster size with larger surface area interact more with the surrounding carbon matrix (Au-C interaction) and gives rise to an increase in the higher binding energy state of $4f_{7/2}^{+\delta}$ and $4f_{5/2}^{+\delta}$.⁶⁵ Similar effect is also observed in the C 1s peak. At lower Au content, the sp^3 content was more in DLC-Au: 4.7% than the pure DLC coating and as the gold content increases in the DLC matrix, the sp^3 content decreases to the value of pure DLC coating. Hence, DLC-Au: 4.7% nano-composite possesses highest sp^3 content and maximum number of Au^{+1} species with lowest Au content.⁶⁵ The Au^{+1} species available in DLC-Au: 4.7% reduces the compressive stress of film by interacting with the sp^3 bonded carbons. The reduction of compressive stress is discussed in detail in the Raman section.

5.3.4.2. EDS Study

Figure 5.7. (a-d) presents the EDS spectra of DLC and DLC-Au nano-composite specimens. The EDS profiles indicate the presence of C, Si and Au. Si peak arises from the Si (111)

substrates. The evolution of Au content in DLC-Au nano-composites is found to be in agreement with the XPS results. Whereas the tabulated (as inset) Au content values such as 1.6, 3.8 and 9.2 at% for DLC-Au: 4.7%, DLC-Au: 7.3% and DLC-Au: 12% are different from the XPS values, respectively.⁶⁵ This variation in EDS and XPS results arises due to the experimental limitations and nature of the characterization techniques, which is neglected in this study. Since evolution of Au content is same in both the studies, so from accuracy aspect XPS result is considered in discussions of further results.

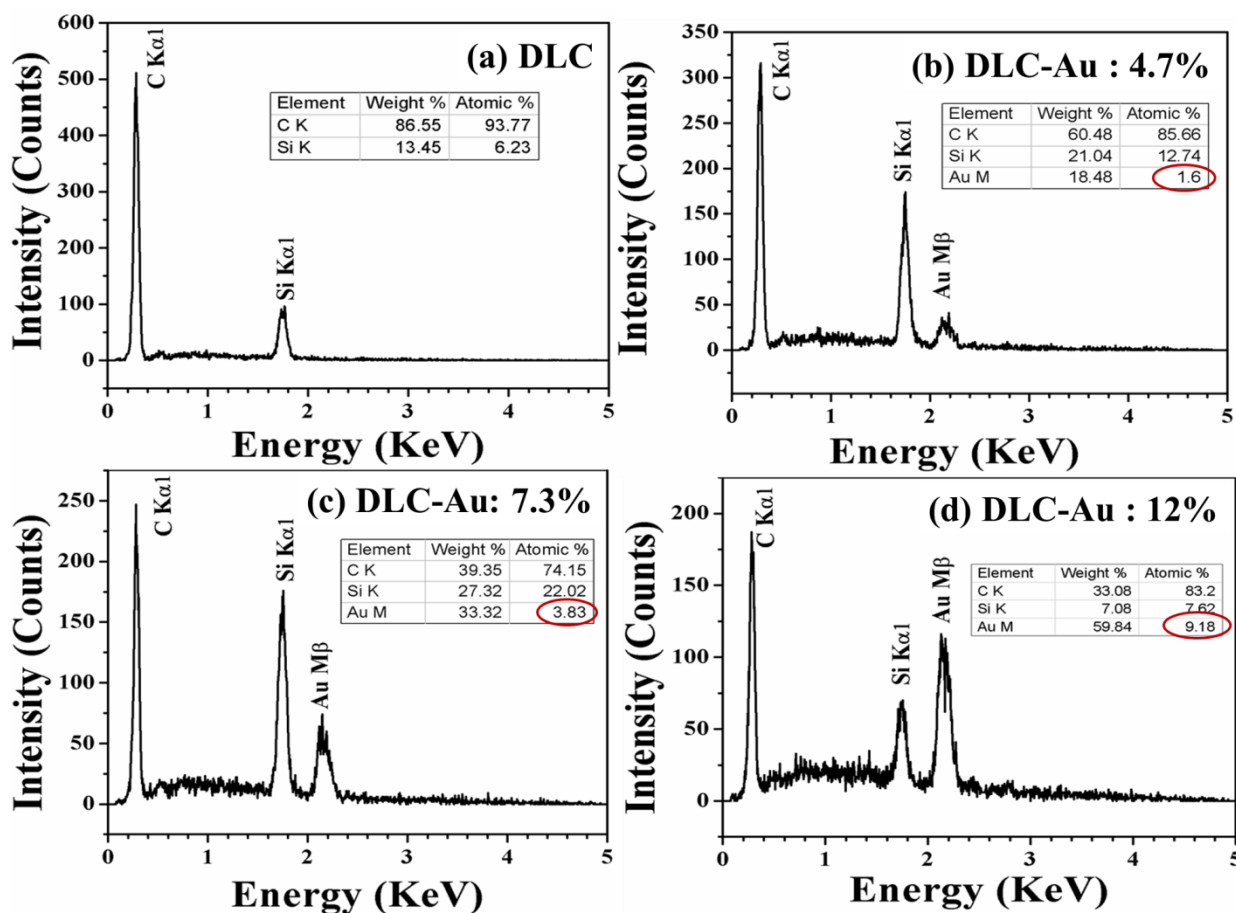


Figure 5.7. EDS spectra of (a) DLC, (b) DLC-Au: 4.7% (c) DLC-Au: 7.3%, (d) DLC-Au: 12% specimens.

5.3.5. Vibrational Analysis

5.3.5.1. EELS Study

The Carbon C (1s) K edge electron energy loss spectra of DLC and DLC-Au nano-composites in the energy loss range from 275 to 340 eV are presented in **Figure 5.8. (a-d)**. The sp^3 content can be determined from the Carbon C (1s) K edge loss spectra using an empirical technique developed by Bruley *et. al.* ¹⁴⁵ The peaks in the regions 284 to 288 eV and above 289 eV arise due to the excitation of electrons from the 1s ground state to the vacant π^* anti-bonding state and from the 1s ground state to the higher σ^* state, respectively.

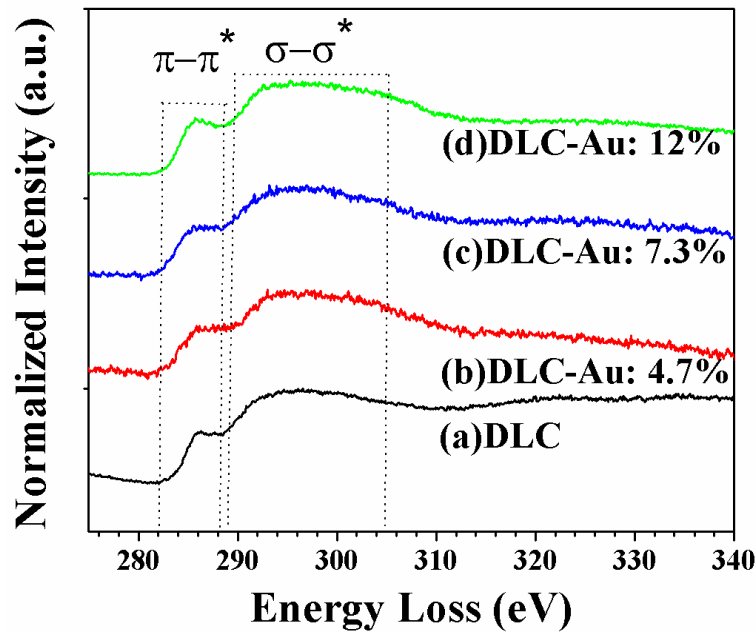


Figure 5.8. Carbon C (1s) K edge EELS spectra of (a) DLC, (b) DLC-Au: 4.7% (c) DLC-Au: 7.3%, and (d) DLC-Au: 12% specimens.

The relative number of π^* and σ^* orbitals are apparently proportional to the ratio of the integrated areas under these two energy windows. The atomic fraction of sp^2 bonded carbon (x) can be estimated using the following equation:

$$\frac{(I_{\pi}/I_{\sigma})_s}{(I_{\pi}/I_{\sigma})_r} = \frac{3x}{4-x} \quad \dots\dots (5.1)$$

Where, $I(\pi)$ is the integrated intensity in the range from 282 to 288eV, and $I(\sigma)$ is the integrated intensity in the range from 289 to 305eV. The subscripts s and r stands for the ratio determined for the DLC, DLC-Au nano-composites and a reference material (graphite) with 100 % sp^2 bonding, respectively. In the present study, the qualitative evolution of sp^2 content in DLC and DLC-Au nano-composites with the Au content is discussed by comparing $I(\pi)$. **Figure 5.8. (a-d)** indicates that $I(\pi)$ value in DLC-Au: 4.7% decreases as compared to DLC, whereas it increases with increase in Au content for DLC-Au: 7.3% and DLC-Au: 12% specimens. Hence, it can be concluded that sp^2 content in DLC: 4.7% is less than DLC and sp^2 content increases with increase in Au content for DLC-Au: 7.3% and DLC-Au: 12% specimens. This result is in concurrent with the XPS and EDS results.

5.3.5.2. Raman Study

Figure 5.9. (a-d) shows de-convoluted Raman spectra of DLC and DLC-Au nano-composite specimens. In **Figure 5.9. (a-d)**, an asymmetric evolution of the Raman peaks with increase in gold content is observed. The G ($1537 - 1560 \text{ cm}^{-1}$) and D ($1341 - 1370 \text{ cm}^{-1}$) bands in Raman spectrum of DLC and DLC-Au films correspond to the stretching and breathing modes of C–C sp^2 hybridized bond, respectively. The visible Raman spectrum is used to probe the ordering of sp^2 sites due to its lower photon energy and indirectly measures the sp^3 fraction in the film. **Figure 5.9. (a-d)**, depicts that in addition to G and D peaks, a third prominent peak at 1120 cm^{-1} also emerges in all specimens. This assigned to distorted C–C sp^3 stretching vibration.^{61, 65, 132} It is also observed that in DLC-Au: 4.7% nano-composite, the contribution from distorted C–C sp^3 stretching vibrations (third peak) is less than DLC,

whereas in DLC-Au: 7.3% and DLC-Au: 12%, it increases with increase in Au content. The sp^3/sp^2 ratio and sp^2 cluster size are estimated from I_D/I_G ratio (obtained from ratio of intensity under the curve). **Figure 5.9.** (a, d) presents that DLC-Au: 4.7% exhibits lower I_D/I_G value than pure DLC which represents smaller sp^2 cluster size and larger sp^3 fraction in this film.^{61, 62, 65}

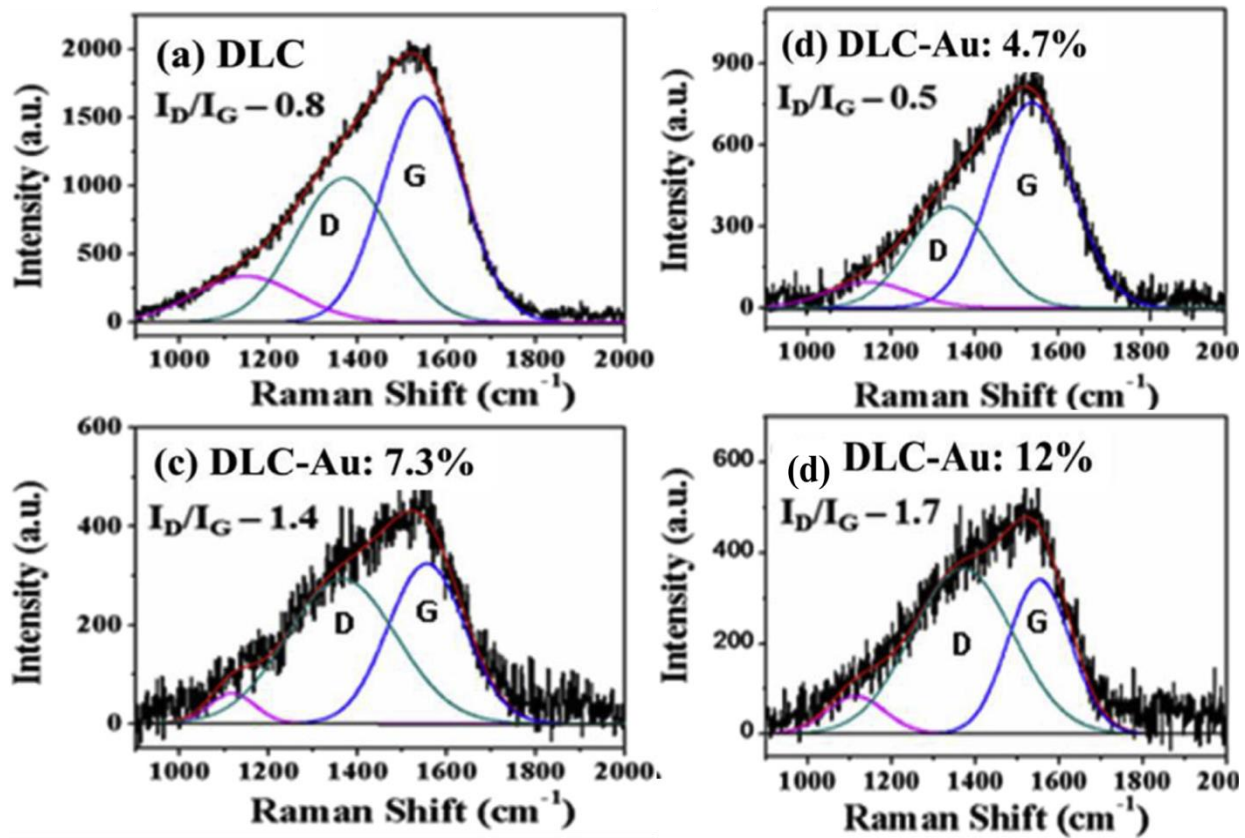


Figure 5.9. De-convoluted Raman spectra of (a) DLC, (b) DLC-Au: 4.7% (c) DLC-Au: 7.3%, and (d) DLC-Au: 12% specimens.

It is clearly observed from **Figure 5.9.** (a, d) that in DLC-Au: 4.7% the D-line indicated a shift in the peak positions towards lower wave number, whereas it shows a shift towards higher wave number for DLC-Au: 7.3% and DLC-Au: 12%. This result indicates

that the bond length of rings is longer than that of chains (olefins) present in DLC-Au: 4.7% and reverse in DLC-Au: 7.3% and DLC-Au: 12%.^{65, 132} Thus, the Raman study concludes that these films are composed of sp^3 -bonded carbon matrix with dispersed sp^2 -bonded carbon clusters.

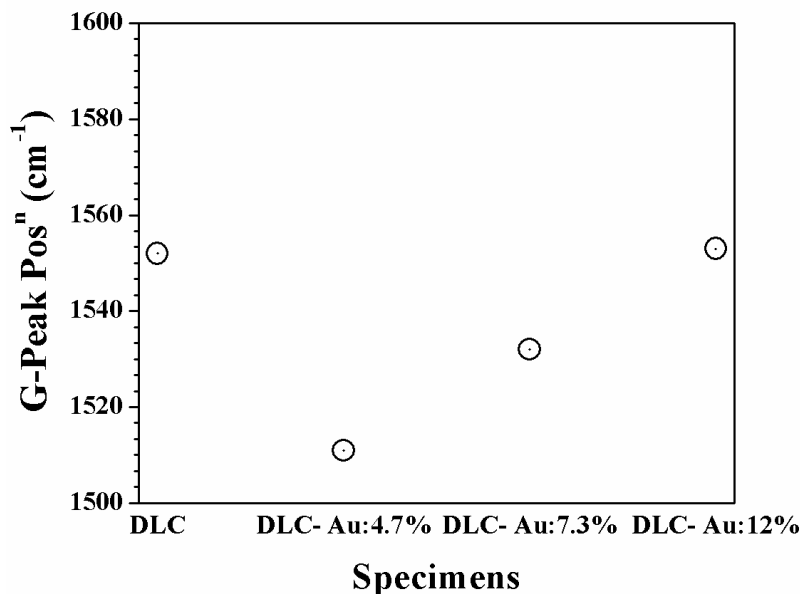


Figure 5.10. G-Peak position evolutions in DLC and DLC-Au nano composites specimens.

Figure 5.10. represents the G-peak position evolutions in DLC-Au nano-composites specimens with Au at.%. In this study the Raman G-peak shifts are used to determine the compressive stress reduction in DLC-Au nano-composites with respect to the pure DLC film. The expression for compressive stress, δ , is given as: ^{65, 146}

$$\delta = 2G \frac{(1+\nu)}{(1-\nu)} \frac{\Delta\omega}{\omega_0} \dots\dots\dots (5.2)$$

where $\Delta\omega$, ω_0 , G and ν are the shift in the Raman wavenumber, the wavenumber of a reference state (pure DLC in this study), the shear modulus of the material and the Poisson ratio, respectively. Value of $2G(1+\nu)/(1-\nu)$ for DLC is considered as 300 GPa and the

estimated compressive stress reduction for DLC-Au: 7.3% and DLC-Au: 4.7% films with respect to the pure DLC film are found as 3.9 and 7.9 GPa, respectively. **Figure 5.10.** also presents no significant G-peak shift for DLC-Au: 12%, which indicates no reduction of compressive stress due to equalization of Au-Au and C-C interactions with Au-C interaction. The detailed Raman analysis of various parameters (G-peak shift and I_D/I_G) indicates a contradictory result to literature that DLC-Au: 4.7% film shows highest compressive stress reduction (7.9 GPa) with highest sp^3 content.^{132, 136} This contradiction can be explained on the basis of evolution of number of Au⁺ species in DLC-Au nano-composites with Au content discussed in the XPS section. The higher number of Au⁺ species in DLC-Au: 4.7% reduces the compressive stress irrespective of the sp^3 content by enhancing the Au-C interaction.

5.4. Summary

DLC-Au nano-composite films were deposited using graphite-Au composite target by Pulsed Excimer laser Deposition at three different laser indexing angles. FESEM and AFM morphology studies indicate that the number density of Au clusters increases with increase in laser track on the gold foil. XPS, EDS and EELS studies show that the Au incorporations in DLC modified the sp^2/sp^3 of the specimens. Moreover optimized doping concentration enhanced the sp^3 fraction with the formation of ultra-nano gold crystallites. The Au crystallite size was determined from TEM and XRD studies. The Raman analysis confirms that DLC-Au: 4.7% film shows highest compressive stress reduction (7.9 GPa) with highest sp^3 content, lowest Au content/ smallest Au cluster and higher number of Au⁺ species, thus indicating it to be a preferred specimen.

CHAPTER 6

A Study on Mechanical and Tribological Performance of DLC-Au Nano-composites

“ Be faithful in small things because it is in them that your strength lies”

Mother Teresa

This chapter starts with a discussion on mechanical and tribological properties of DLC-Au nano-composites from literature. A brief introduction regarding the influence of Au content, on Au cluster size, C-C sp^2 cluster size, morphology, composition and vibrational property of DLC-Au nano-composite films from chapter-5 is presented. In addition, a detailed investigation to study the influence of Au content/ cluster size on the mechanical and tribological properties of DLC-Au nano-composites, along with the vibrational properties of tribo-tracks and ball scars, is also carried out through various characterizations such as: nano-indentation, tribology and Raman study on tribo-tracks and ball scars, respectively.

6.1. Introduction

The embodiment of noble metals into the DLC matrices forms a nano-composite with improved physical properties and complementary functionalities. Gold and silver (Au, Ag) like noble metals govern the high intrinsic residual compressive stress in the DLC based nano-composites.^{131, 132} The compositional variation of metals helps to control the physical and mechanical properties of the nano-composites for various optical, mechanical and tribological applications.¹³²⁻¹³⁶ More recently, enhanced nano-tribological property of DLC-

Ag nano-composites with various Ag contents have been reported by Constantinou *et. al.*¹³⁶ Similarly a report on synthesis and nano-mechanical properties of hydrogenated DLC-Au nano-composites of varying gold content (2–7%) and Au crystallite size in the range of 2.7–3.5 nm has been reported by Paul *et. al.*^{134, 147} In the present study, the first ever attempt is made to the best of our knowledge to understand the influence of Au content/ cluster size on tribological property of un-hydrogenated DLC-Au nano-composites in a systematic manner. For this investigation the un-hydrogenated DLC-Au nano-composites are synthesized from a composite target of graphite and Au using an excimer laser at various laser indexing angles. It is observed that the variation of Au content in un-hydrogenated DLC matrix modulates the intrinsic stress along with the evolution of Au cluster size, sp^3 content, sp^2 cluster size and the number of Au^{+1} species as discussed in chapter-5.⁶⁵ It is observed that DLC-Au: 4.7% nano-composite shows highest compressive stress reduction (7.9 GPa) along with highest sp^3 content, lowest Au content/ smallest Au cluster and higher number of Au^{+1} species.⁶⁵ The present chapter deals with the influence of Au content/ Au cluster size on mechanical and tribological properties of un-hydrogenated DLC-Au nano-composites followed by vibrational investigation of tribo-track and ball scar.

6.2. Characterization

The un- hydrogenated DLC-Au nano-composites specimens are labeled as DLC–Au: 12%, DLC–Au: 7.3% and DLC–Au: 4.7% depending on the Au contents.⁶⁵ The thickness of DLC and DLC-Au nano-composites are 160 and 100 nm, respectively.⁶⁵ The Mechanical and tribological properties as well as the vibrational properties of the tribo-track and ball scar of un- hydrogenated DLC-Au nano-composites specimens are determined using Nano-Indentation, tribometer and Raman Spectroscopy, respectively. Since the details of the

synthesis conditions and characterization procedures are already discussed in the corresponding sections of chapter-2, no further experimental details are provided here to avoid repetition.

6.3. Results and Discussion

6.3.1. Mechanical properties of DLC-Au nano-composites

The indentation test has been performed to reveal the penetration resistance of DLC and DLC-Au nano-composites by a known geometry indenter under a fixed load. Load-displacement curve is one of the possible and widely used methods to study the behavior of the elastic recovery of the thin film. The deformation due to loading during indentation test is considered to be both elastic and plastic in nature, whereas during unloading, it is assumed that only the elastic displacements are recovered. The elastic nature of the unloading curve facilitates the analysis.

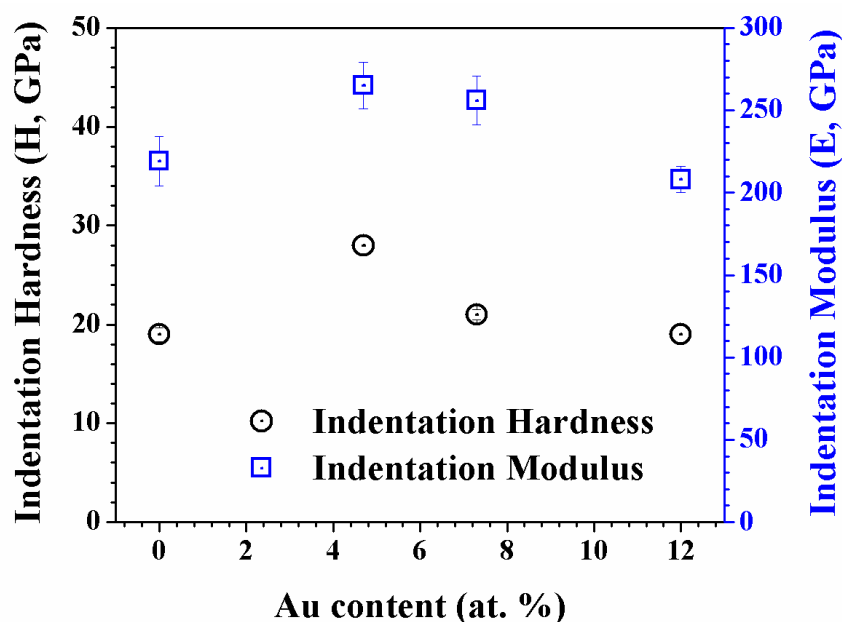


Figure 6.1. Evolution of hardness (H) and elastic modulus (E) with Au content in DLC matrix.

The loading and unloading curves for DLC and DLC-Au nano-composites are obtained by indenting the films at 0.1 mN peak load to obtain contact depths under 10% of the film's thickness. The absence of creep and thermal drift in DLC and DLC-Au nano-composites films is verified by holding the indenter at maximum load for 2 sec (no variation in penetration depth). The indentation hardness (H) and modulus (E) of these specimens are extracted from the loading and unloading of the indentation curve using Oliver and Pharr method as described in section 2.3.10..⁹¹ The evolution of hardness (H) and elastic modulus (E) for DLC and DLC-Au nano-composites films with Au content are shown in **Figure 6.1.**

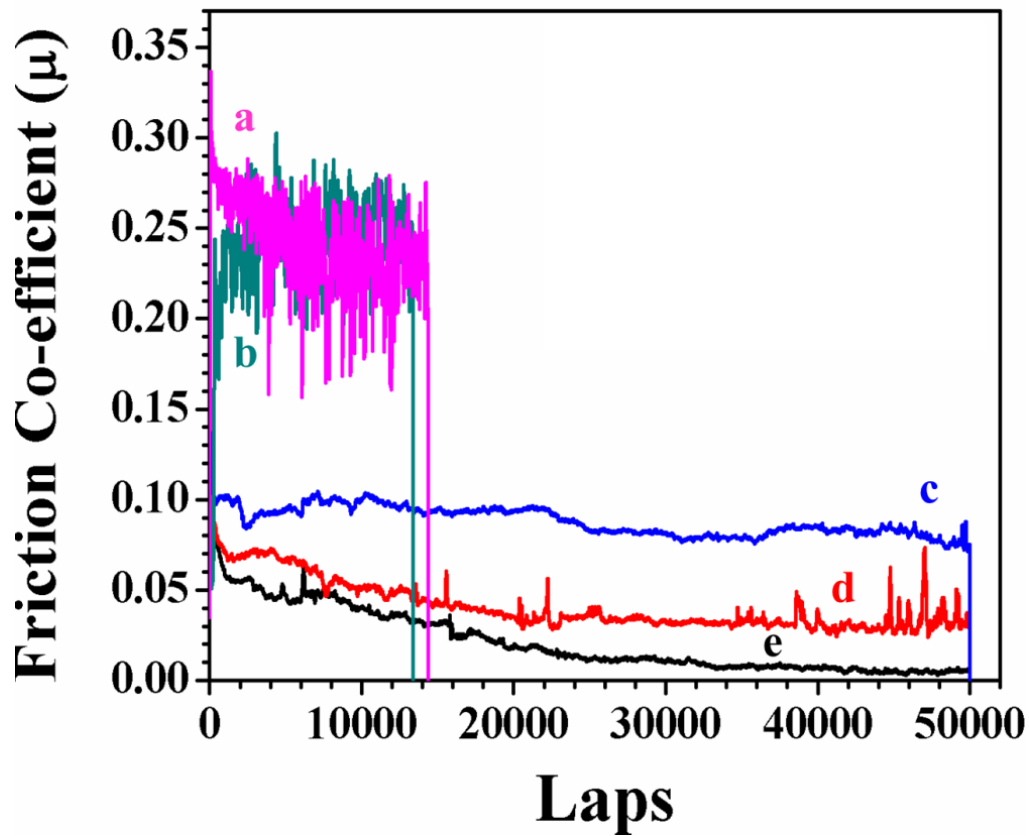


Figure 6.2. Micro tribo test carried out at ambient and unlubricated conditions on (a) Si(100), (b)DLC, (c)DLC-Au: 12%, (d)DLC-Au: 7.3%, and (e)DLC-Au: 4.7% specimen.

It is observed from **Figure 6.1.** that the hardness (H) and elastic modulus (E) of the DLC-Au: 4.7% films is significantly enhanced as compared to pure DLC film. In addition, it is also observed that H and E values of DLC-Au: 7.3% and DLC-Au: 12% films decreases, this result can be attributed to the consequences of rise in Au content, such as enhanced clustering of Au and sp^2 bonded carbons and reduction in sp^3 content.⁶⁵ The evolution of sp^3 content and clustering of Au and sp^2 bonded carbons have been verified by XPS, EDS, EELS, XRD, and TEM characterization techniques, and the detailed discussion is presented in chapter-5.⁶⁵

6.3.2. Tribological study of DLC-Au nano-composites

The friction behavior of DLC and DLC-Au nano-composites is shown in **Figure 6.2.** (a- e). **Figure 6.2. (a- e).** reveals that DLC and DLC-Au nano-composite specimens exhibit lower CoF as compared to Si (100) substrate. But the DLC specimen could sustain only for few laps followed by the complete detachment of the film from the substrate. This is due to the poor adherence of DLC specimen to the silicon substrate, which is the consequence of the residual compressive stress produced during the deposition process.^{132, 136} However, DLC-Au nano-composites (**Figure 6.2. (b-e)**) show ultralow Co-efficient of Friction (CoF) values and good adhesion.

This observation indicates that Au incorporation in DLC has reduced the residual compressive stress in the matrix and improved the adhesion and the wear resistance properties. It is also found that DLC-Au: 4.7% exhibits lowest CoF (~ 0.05). It is reported that low friction in DLC depends on several factors like sp^2/sp^3 ratio, transfer layer formation, changes in specimen structure during sliding and temperature changes that occur during sliding.^{132, 136, 147} However, in the DLC-Au: 4.7% specimen, the low value of CoF

couldn't be explained by the high fraction of sp^3 bonding as evident from XPS and Raman study. Since high sp^3 fraction in DLC-Au: 4.7% specimen exhibits high shear resistance dissipating high frictional energy due to its tetrahedral structure, this increases CoF. Tribology tests have been carried out several times to ensure the accuracy of the results. Hence, the observed tribological response could be assigned to the other factors like formation of transfer layer, variations in specimen structure during sliding and temperature changes that occur during sliding, which arises due to dispersion of metallic Au nanoparticles and Au^{+1} species in the DLC matrix. XRD, TEM and XPS result revealed that DLC-Au: 4.7% possess smallest Au cluster and higher fraction of Au^{+1} species at lowest Au content, which enhances sp^3 content resulting high hardness and chemical reactivity.⁶⁵ The reduced value of CoF in DLC-Au: 4.7% can also be attributed to the reduced contact area of gold clusters at the interface during sliding, which provides less shear resistance dissipating low frictional energy and results low CoF.^{148, 149}

A gradual decrease in CoF with sliding distance is also noticed in DLC-Au: 4.7% film, this can be attributed to the formation of graphitized tribo-film. To corroborate this assumption, additional measurements were carried out in loop tribo-condition under similar experimental parameters with Raman analysis on tribo-track and ball scars. The first loop measurements was carried out up to 15000 laps and second loop up to 50000 laps on DLC-Au: 4.7% specimen.⁶⁵ The specimens were labeled as DLC-Au: 4.7% –15000 laps and DLC-Au: 4.7% –50000 laps, respectively. In addition, Raman analysis on tribo-track and ball scar was carried out systematically.

6.3.3. Raman investigation of tribo-tracks

Micro-Raman spectroscopy is carried out across the tribo-track for describing the nature of the secondary phases in order to have better understanding of evolution of the chemical characteristics in DLC and DLC-Au nano-composite film under loop tribo-conditions.

Figure 6.3. (b and c) represent the optical image of tribo-track created under loop condition for DLC-Au: 4.7% with reference to DLC **Figure 6.3.** (a) along with the corresponding Raman spectra obtained from various regions across the tribo-tracks.

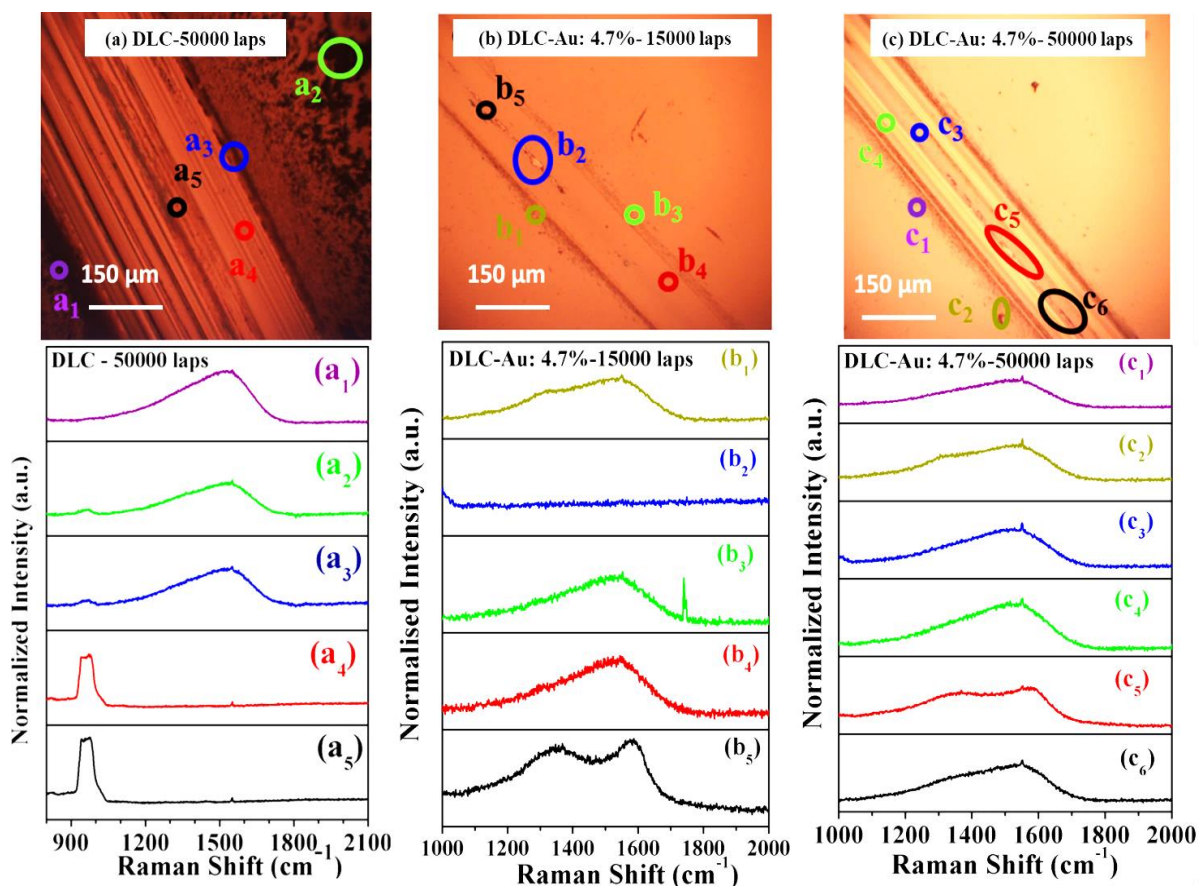


Figure 6.3. Optical Image of Tribo-track and corresponding Raman spectra at various locations of (a) DLC -50000 laps, (b). DLC-Au: 4.7%-15000 laps, and (c) DLC-Au: 4.7% -50000 laps specimens.

Figure 6.3. (**a₄** and **a₅**) depict absence of DLC signature on tribo-track, whereas signature of DLC was evident at debris (**Figure 6.3. (a₁-a₃)**), which indicates that DLC is loosely adhered to the substrate. **Figure 6.3. (b₁, b₃, b₄ and b₅)** except **Figure 6.3.(b₂)**, showed the evidence of DLC and amorphized//graphitized DLC on tribo-track of DLC-Au: 4.7% after 15000 laps run. **Figure 6.3. (c₂, c₅, and c₆)** represent the Raman spectra obtained from debris and some deformed regions on tribo-track of DLC-Au: 4.7% after 50000 laps run. This showed evolution of D-peak which clearly indicates increase in I_D/I_G , whereas other plane regions shown in **Figure 6.3. (c₁, c₃, and c₄)**, showed no significant changes. The evolution of D-peak with increase in I_D/I_G can be attributed to graphitization.^{61, 62, 132}

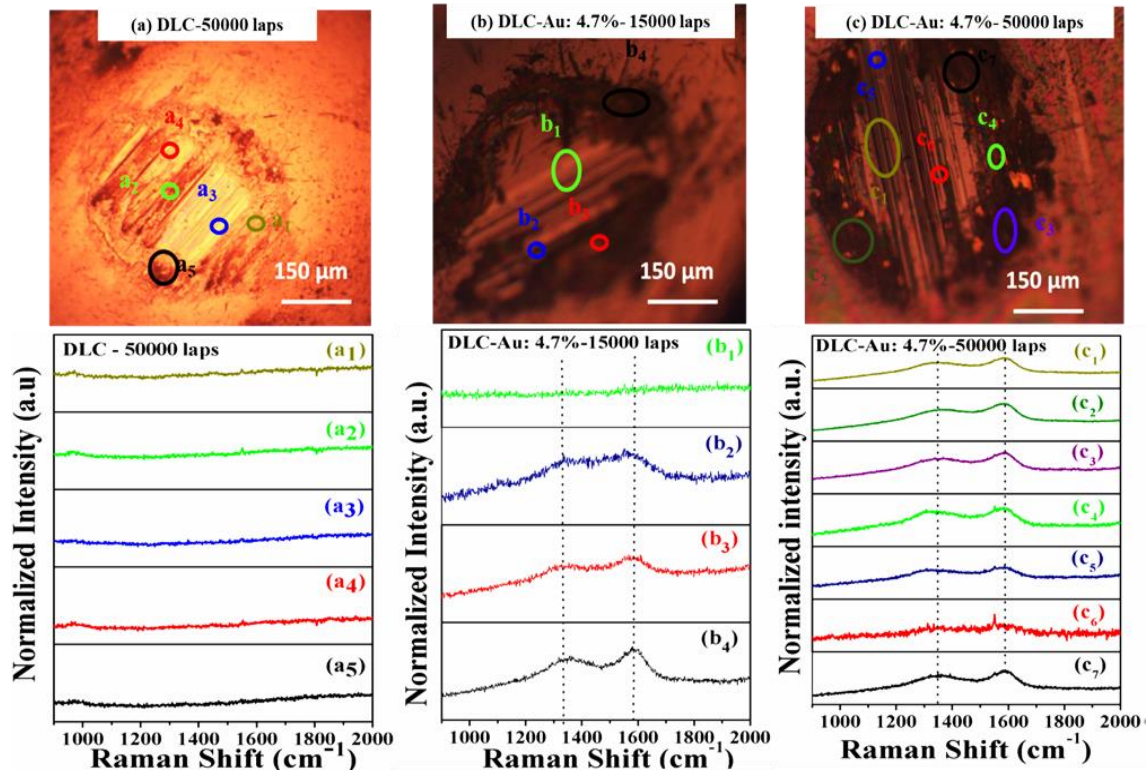


Figure 6.4. Optical Image of scar on ball and corresponding Raman spectra at various regions of (a) DLC -50000 laps, (b). DLC – Au: 4.7% –15000 laps and (c) DLC – Au: 4.7% –50000 laps specimens.

A comparison between **Figure 6.3. (b₁, b₂, b₅)** and **Figure 6.3. (c₂, c₅, c₆)**, indicate that debris sustains similar graphitization but in the detached film region; graphitization nucleated at line scratch and gets modified with sliding distance up to 50000 laps. It is also observed that the probability of graphitization decreases from the line scratch of DLC-Au: 4.7%-15000 to the deformed region of DLC-Au: 4.7%-50000 laps specimen. These results indicate the formation of tribo-film on the ball and require the Raman investigation on the scar of the ball.

6.3.4. Raman investigation of ball scars

Micro-Raman spectroscopy is also carried out across the ball-scar for DLC and DLC-Au nano-composite films under loop tribo-conditions to evident the suspect of tribo-film formation and also for a better understanding of evolution of the chemical characteristics. **Figure 6.4. (a-c)** shows optical image of scar on ball and corresponding Raman spectra of DLC, DLC – Au: 4.7% –15000 laps and DLC-Au: 4.7% –50000 laps samples, respectively. **Figure 6.4. (a)** exposes no tribo-film formation on ball, whereas **Figure 6.4. (b and c)** confirmed tribo-film formation on the sliding ball. It is also clear from **Figure 6.4. (b and c)** that the tribo- film nucleated on the ball at 15000 laps spread over the ball at 50000 laps leading to the decrease in CoF.

In **Figure 6. 3. (b and c)** and **Figure 6.4. (b and c)**, DLC signature with various chemical nature is observed at some regions on both tribo-track and ball-scar of DLC-Au: 4.7% films under loop tribo-condition. This result demands a detailed analysis of the obtained Raman spectra. Hence, in order to better understand the chemical evolution at the interface of track and ball during sliding, the Raman spectra obtained from the tribo-track and scar on ball are de-convoluted into and presented in **Figure 6.5.** and **Figure 6.6,**

respectively. The G ($1537 - 1560 \text{ cm}^{-1}$) and D ($1341 - 1370 \text{ cm}^{-1}$) bands in Raman spectrum of DLC and DLC-Au films correspond to the stretching and breathing modes of C-C sp^2 hybridized bond, respectively. **Figure 6.5.** and **Figure 6.6,** show that in addition to G and D peaks, a third prominent peak at 1120 cm^{-1} also emerges in all specimens. This assigned to distorted C-C sp^3 stretching vibration.^{61, 65, 132}

All the deconvoluted Raman spectra show prominent D-Peak as a shoulder, which indicates presence of aromatic sp^2 clusters. Hence I_D/I_G is the suitable parameter to observe the chemical evolution on tribo-track and scar of ball.

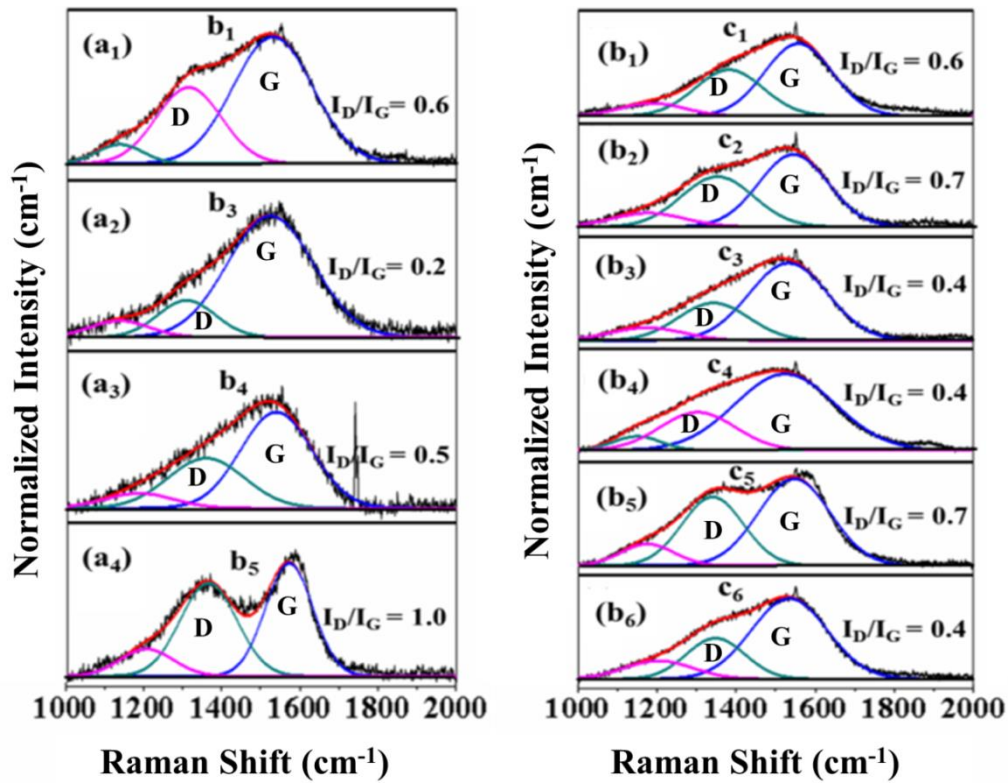


Figure 6.5. I_D/I_G determination from deconvoluted Raman spectra on tribo-track at various regions of (a) DLC-Au: 4.7%-15000 laps and (b) DLC-Au: 4.7%-50000 laps specimens.

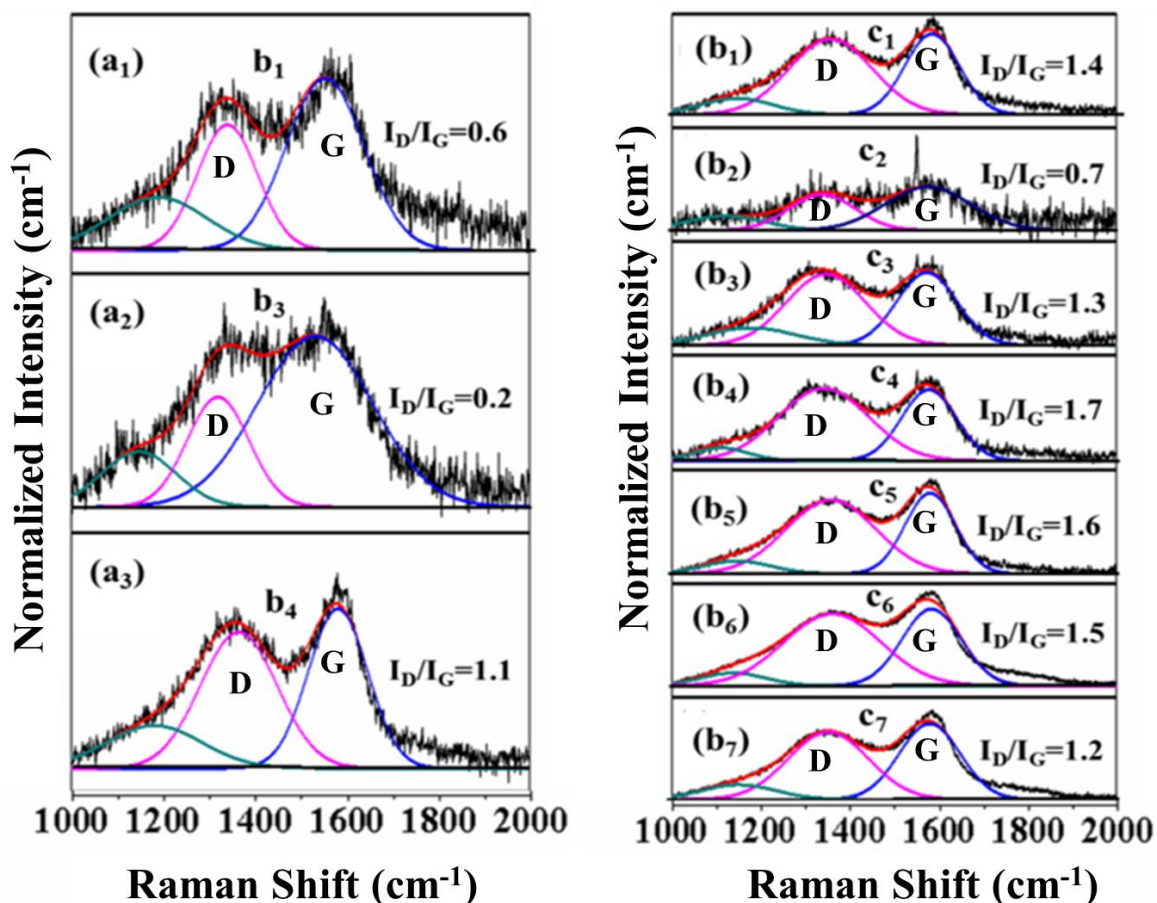


Figure 6.6. I_D/I_G determination from deconvoluted Raman spectra on ball scar at various regions of (a) DLC-Au: 4.7%-15000 laps and (b) DLC-Au: 4.7%-50000 laps specimens.

The I_D/I_G is estimated from the corresponding integrated peak intensity of the deconvoluted Raman spectra. The average value of I_D/I_G from various regions of tribo-track and scar on ball under loop tribo-condition is considered for better understanding. **Figure 6.7.** represents the evolution of I_D/I_G on tribo-track and scar on the ball with laps. It is observed from **Figure 6.7.** that the I_D/I_G obtained from tribo-track shows no significant change with higher sliding laps, whereas I_D/I_G for ball enhances from 0.6 ± 0.5 to 1.3 ± 0.5

with increase of laps from 15000 to 50000 laps indicating formation of graphitized tribo-film on the ball.^{17, 132} This graphitized tribo-film on the ball-scar act as a lubricant and reduces the CoF to ultra-low value gradually with increase in the sliding laps.

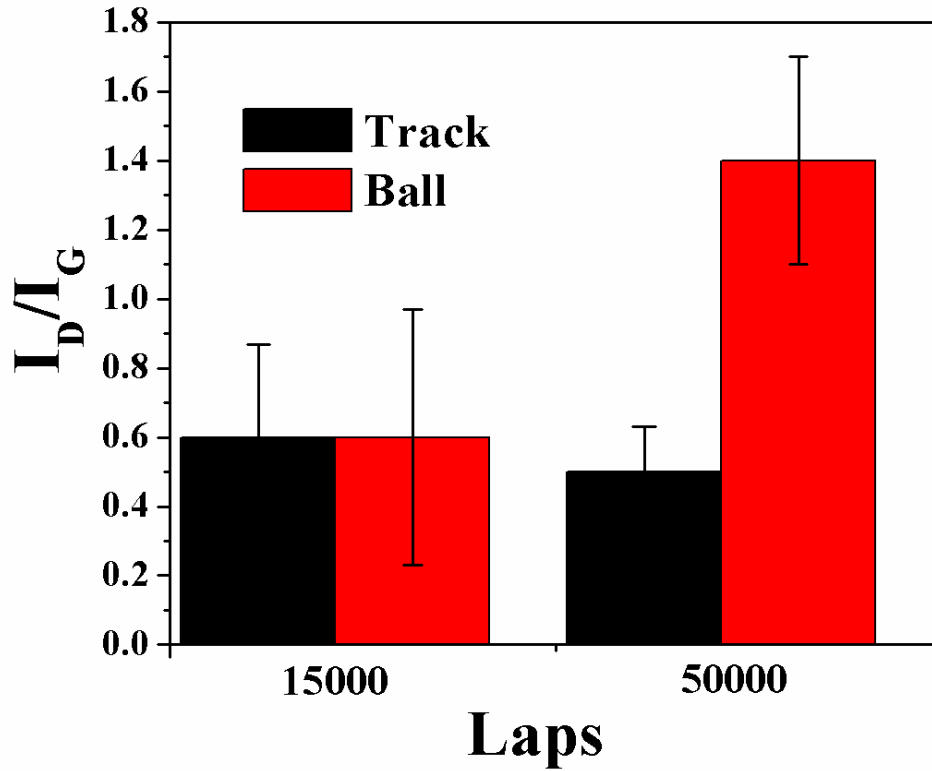


Figure 6.7. I_D/I_G vs laps on track and ball scar.

6.4. Summary

The mechanical properties and tribological behavior of DLC-Au nano-composites are explored using nano-indentation and tribometer. It is found that DLC-Au: 4.7% exhibited maximum indentation hardness (28 ± 0.9 GPa) and elastic modulus (265 ± 14 GPa). It is also noticed that the tribological behavior of DLC-Au: 4.7% nano-composite showed ultralow CoF value of ~ 0.05 and high wear resistance with a gradual decrease in CoF to ultra-low value with sliding distance. A comprehensive micro-Raman spectroscopy investigation on

tribo-track and ball scar under loop tribo-condition revealed that the gradual decrease in CoF to ultra-low value is due to a graphitized (sp^2 rich) tribo-film formed on ball scar, this acts as a lubricant at the sliding interfaces and governs the tribological behaviors.

CHAPTER 7

Conclusions and Future Directions

“Progress in Science comes when experiments contradict theory.”

Richard P. Feynman

This chapter summarizes the key results and conclusive remarks of the present thesis work. In addition to that, a few future directions has also been proposed as an extent to the present thesis, based on the present understanding of the subject area.

7.1. Conclusions

The present thesis reports the growth of particulate laden DLC films and DLC-Au nano-composites by PLD techniques, using Nd: YAG and Excimer laser, respectively. The synthesis of particulate laden DLC films is carried out by ablation of a pure graphite target at various laser pulse energies, whereas the DLC-Au nano-composites are synthesized from the ablation of a graphite-Au composite target at various laser indexing angles. Thickness and morphological study of particulate laden DLC films indicate that thickness of film, size and no. density of particulates on specimen surface increases with increase in laser pulse energies, respectively. The vibrational property investigation of particulate laden DLC films using vis- Raman mapping and multi-excitation Raman concludes that both flat and particulate regions follow two different growth mechanisms. The flat region follows sub-plantation model up to 300 mJ and above it follows thermal spike model, whereas the particulate region completely depends on the structural modifications of the particulates in the plasma. It is also observed that the surface energy and contact angle of the DLC

specimens are influenced by the presence of particulates. Composition and mechanical investigations predicted DLC-3 as the stiffest and hardest specimen with maximum sp^3 content, suggesting as optimum laser pulse energy.

In addition, DLC-Au nano-composites are synthesized from the ablation of a graphite-Au composite target at various laser tracks by varying the laser indexing angles (10^0 , 20^0 , 30^0). The morphological study by FESEM and AFM reveals that Pure DLC possesses small particulates, whereas size and number density of Au clusters increase with increase in laser track on the Au foil. The presence of Au nano-clusters in DLC-Au nano-composite is confirmed from structural characterizations by XRD and TEM. These studies indicate that the Au cluster size increases with increase in laser track on Au foil. The compositional analysis on DLC-Au nano-composites by XPS and EDS indicate that the laser ablation from laser track on gold at 30^0 indexing angle incorporates minimum Au content (4.7 %) in DLC, which increases with increase in laser track on Au foil. It is also observed that the increase in Au content increases the Au cluster size, whereas the sp^3 content decreases in DLC-Au nano-composite films. EELS study also provides the qualitative analysis for sp^3 content. In addition, Raman analysis reveals the evolution of sp^2 cluster size and compressive residual stress with Au contents. It is observed that the DLC-Au nano-composite corresponding to the laser indexing angle 30^0 (Au: 4.7 at %) possesses highest sp^3 fraction (41.4 %) with the formation of ultra-nano gold crystallites (1.5 nm). The smallest Au cluster in DLC Au: 4.7% improves the mechanical properties of DLC matrix leading to modified tribological behavior of films, which shows ultralow CoF of ~ 0.05 and high wear resistance. In addition, the gradual decrease in CoF to ultra-low value with sliding distance is governed by sp^3/sp^2 phase transformation in the sliding interfaces. This was comprehensively

investigated by micro-Raman on tribo-track and ball scar. It reveals that the graphitized tribo-film formed on ball helps in gradual decrease of CoF to ultra-low value.

7.2. Future Directions

The current thesis reports on the growth, characterizations and tribological performance of DLC-Au nano-composites with various sizes Au nano- clusters synthesized by PLD using KrF laser source. An attempt through micro- Raman spectroscopy has given to understand the reason behind low CoF and its gradual decrease to ultra-low value for DLC-Au nano-composites with smallest Au clusters (1.5 nm). However, still several issues (listed below), need to be addressed to get clear picture for the application of DLC-Au nano-composites:

- Tribological study on DLC-Au nano-composites at various loads with different balls for better understanding of tribological mechanism.
- High temperature tribological study of DLC-Au nano-composites.
- Synthesis and investigation of chameleon nano-composites by PLD with DLC-Au matrix using both composite target architecture and multi-targets.

References

1. Preparation of chameleon coatings for space and ambient environments, C. C. Baker, R. R. Chromik, K. J. Wahl, J. J. Hu, A. A. Voevodin, *Thin Solid Films*, 2007, 515, 6737–6743.
2. Chameleon Coatings: Adaptive Surfaces to Reduce Friction and Wear in Extreme Environments, C. Muratore and A. A. Voevodin, *Annu. Rev. Mater. Res.*, 2009, 39, 297–324.
3. Adaptive multicomponent nano-composite coatings in surface engineering, A. D. Pogrebnjak, A. A. Bagdasaryan, A. Pshyk, K. Dyadyura, *Physics-USpekhi*, 2017, 60 (6), 586-607.
4. Hard coatings with high temperature adaptive lubrication and contact thermal management: review, A. A. Voevodin, C. Muratore, S. M. Aouad, *Surf. and Coat. Techn.*, 2014, 257, 247- 265.
5. Growth and structural characterization of yttria-stabilized zirconia–gold nano-composite films with improved toughness, A. A. Voevodin, J. J. Hu, J. G. Jones, T. A. Fitz, J. S. Zabinski, *Thin Solid Films*, 2001, 401, 187–195.
6. Die Beeinflussung von festen Oberflächen durch eine ionisierte, H. Schmellenmeier, *Exp. Tech. Phys.*, 1953, 1, 49-68.
7. Ion-beam deposition of thin films of diamond-like carbon, S. Aisenberg, and R. Chabot, *J. Appl. Phys.*, 1971, 42, 2953-2958.
8. Cutting applications of DLC, hard carbon and diamond films, T. C. S. Vandavelde, K. Vandierendonck, M. V. Stappen, W. D. Mong and P. Perremans, *Surf. and Coat. Techn.*, 1999, 113 (1-2), 80-85.
9. Tribological properties of aC: H multilayer structures, L. Knoblauch-Meyer and R. Hauert, *Thin Solid Films*, 1999, 338 (1-2), 172-176.
10. Chemical, mechanical and tribological characterization of ultra-thin and hard amorphous carbon coatings as thin as 3.5 nm: recent developments, B. Bhushan, *Diam. and Relat.*

- Mater., 1999, 8 (11), 1985-2015.
11. New application perspective for tetrahedral amorphous carbon coatings, S. Neuville, QScience Connect, 2014, 2014 (1), 8 (1-27).
 12. Future media manufacturing-more than just conventional sputtering, B. Cord and J. Scherer, IEEE transactions on magnetics, 2000, 36 (1), 67-72.
 13. Handbook of micro/nano tribology, B. Bhushan, CRC press, 1998.
 14. Preparation of amorphous diamond-like carbon by pulsed laser deposition: a critical review, A. A. Voevodin and M. S. Donley, Surf. and Coat. Techn., 1996, 82 (3), 199-213.
 15. Effect of laser intensity on the microstructural and mechanical properties of pulsed laser deposited diamond-like-carbon thin films, M. Tabbal, P. Merel, M. Chaker, M. A. El Khakani, E. G. Herbert, B. N. Lucas, and M. E. O'Hern, J. Appl. Phys., 1999, 5 (7), 3860-3865.
 16. An examination of trace surface on diamond-like carbon film after ball-on disk measurement, W. S. Choi, M. Park and B. Hong, Thin Solid Films, 2007, 515(19), 7560-7565.
 17. Diamond-like amorphous carbon, J. Robertson, Materials science and engineering: R: Reports, 2002, 37 (4-6), 129-281.
 18. Diamond-like carbon: state of the art, A. Grill, Diamond and related materials, 1999, 8 (2-5), 428-434.
 19. Diamond-like carbon—present status, Y. Lifshitz, Diam. and Relat. Mater., 1999, 8 (8-9), 1659-1676.
 20. Raman spectroscopy of amorphous, nanostructured, diamond-like carbon, and nanodiamond, A. C. Ferrari and J. Robertson, Philosophical Transactions of the Royal Society of London. Series A: Math. Phys. and Eng. Sci., 2004, 362 (1824), 2477-2512.
 21. Environmental effects on the friction of hydrogenated DLC films, H. I. Kim, J. R. Lince, O. L. Eryilmaz, and A. Erdemir, Tribology Letters, 2006, 21 (1), 51-56.

22. The effect of relative humidity on wear of a diamond-like carbon coating, J. Jiang, S. Zhang, and R. D. Arnell, *Surf. and Coat. Techn.*, 2003, 167 (2-3), 221-225.
23. Thermal stability of amorphous carbon films grown by pulsed laser deposition, T. A. Friedmann, K. F. McCarty, J. C. Barbour, M. P. Siegal and Dean C. Dibble. *Applied physics letters*, 1996, 68 (12) 1643-1645.
24. Optical emission studies of atomic, molecular, and particulate carbon produced from a laser vaporization cluster source, E. A. Rohlfing, *The Journal of chemical physics*, 1988, 89 (10), 6103-6112.
25. Pulsed laser deposition of functionally gradient diamond- like carbon (DLC) films using a 355 nm picosecond laser, H. Cho, S. Kim, H. Ki, *Acta Materialia*, 2012, 60, 6237-6246.
26. Characterization of DLC coatings deposited by rf magnetron sputtering, S. Chowdhury, M. T. Laugier, I. Z. Rahman, *J. Mater. Process. Technol.*, 2004, 153-154, 804-810.
27. Structural and mechanical properties of a-C:H and Si doped *a-C:H* thin films grown by LF-PECVD, C. Chouquet, G. Gerbaud, M. Bardet, S. Barrat, A. Billard, F. Sanchette, and C. Ducros, *Surf. and Coat. Techn.*, 2010, 204 (9-10), 1339-1346.
28. Intrinsic mechanical properties of diamond-like carbon thin films deposited by filtered cathodic vacuum arc, Z. Gan, Y. Zhang, G. Yu, C. M. Tan, S. P. Lau, and B. K. Tay, *J. Appl. Phys.*, 2004, 95 (7), 3509-3515.
29. Electron-energy-loss spectroscopy of mass-selected ion-beam-deposited diamond-like carbon, J. Kulik, Y. Lifshitz, G. D. Lempert, J. W. Rabalais, and D. Marton, *J. Appl. Phys.*, 1994, 76 (9), 5063-5069.
30. Boronated tetrahedral amorphous carbon (*ta-C: B*), M. Chhowalla, Y. Yin, G. A. J. Amaratunga, D. R. McKenzie and T. Frauenheim, *Diam. and Rel. Mat.*, 1997, 6 (2-4), 207-211.
31. Mechanism of sp^3 bond formation in the growth of diamond-like carbon, J. Robertson, *Diam. and Rel. Mat.*, 2005, 14 (3-7), 942-948.

32. Thermophysical effects in laser processing of materials with picosecond and femtosecond pulses, P. P. Pronko, S. K. Dutta, D. Du and R. K. Singh, *J. Appl. Phys.*, 1995, 78 (10), 6233-6240.
33. Laser fluence dependence of the elastic properties of diamond-like carbon films prepared by pulsed-laser deposition, X. Liu, T. H. Metcalf, P. Mosaner and A. Miotello, *App. Surf. Sci.*, 2007, 253 (15), 6480-6486.
34. Parametric studies of diamond-like carbon by pulsed Nd: YAG laser deposition, S. S. Yap, W. O. Siew, C. H. Nee and T. Y. Tou, *Diam. and Rel. Mater.*, 2011, 20 (3), 294-298.
35. Effects of pulse duration in laser processing of diamond-like carbon films, T. V. Kononenko, V. V. Kononenko, S. M. Pimenov, E. V. Zavedeev, V. I. Konov, V. Romano and G. Dumitru, *Diam. and Rel. Mater.*, 2005, 14 (8), 1368-1376.
36. Effect of laser power density and deposition temperature on electrical and optical properties of pulsed laser ablated diamond-like carbon films, J. Levoska and S. Leppävuori, *Appl. Surf. Sci.*, 1995, 86 (1-4), 180-184.
37. Dynamics of amorphous carbon film growth by pulsed laser deposition: kinetic energy of the incident particles, D. T. Peeler and P. T. Murray, *Diam. and Rel. Mater.*, 1994, 3 (8), 1124-1127.
38. Photoablation of a graphite target by a KrF laser beam. Realisation of hard carbon thin films, C. Germain, C. Girault, J. Aubreton, A. Catherinot, S. Bec, and A. Tonck, *Diam. and Relat. Mater.*, 1995, 4 (4), 309-313.
39. Optical emission study of ablation plasma plume in the preparation of diamond-like carbon films by KrF excimer laser, Y. Yamagata, A. Sharma, J. Narayan, R. M. Mayo, J. W. Newman and K. Ebihara, *J. Appl. Phys.*, 1999, 86 (8), 4154-4159.
40. Diamond-like carbon films prepared by pulsed-laser evaporation, T. Sato, S. Furuno, S. Iguchi and M. Hanabusa, *Applied Physics A*, 1988, 45 (4), 355-360.
41. Particulates generation and solutions for their elimination in pulsed laser deposition, E. György, I. N. Mihailescu, M. Kompitsasa and A. Giannoudakosa, *Journal of*

- Optoelectronics and Advanced Materials, 2004, 6 (1), 39-46.
42. Pulsed-laser deposition of smooth high- T_c superconducting films using a synchronous velocity filter, E. V. Pechen, A. V. Varlashkin, S. I. Krasnosvobodtsev, B. Brunner and K. F. Renk, *Applied physics letters*, 1995, 66 (17), 2292-2294.
 43. Off-axis laser deposition of $\text{YBa}_2\text{Cu}_3\text{O}_{7-\delta}$ thin films, B. Holzapfel, B. Roas, L. Schultz, P. Bauer and G. Saemann-Ischenko, *Applied Physics Letters*, 1992, 61 (26), 3178-3180.
 44. Processes occurring in an erosion plasma during laser vacuum deposition of films. III. Condensation in gas flows during laser vaporization of materials, S. V. Gaponov, A. A. Gudkov and A. A. Fraerman, *Sov. Phys. Tech. Phys*, 1982, 27, 1130-1133.
 45. Stress-induced formation of high-density amorphous carbon thin films, J. Schwan, S. Ulrich, T. Theel, H. Roth, H. Ehrhardt, P. Becker and S. R. P. Silva, *J. Appl. Phys.*, 1997, 82 (12), 6024-6030.
 46. Preparation of WC: H coatings by reactive magnetron sputtering, K. Bewilogua and H. Dimigen, *Surf. and Coat. Techn.*, 1993, 61 (1-3), 144-150.
 47. Hydrogen-free amorphous carbon preparation and properties, D. R. McKenzie, Y. Yin, N. A. Marks, C. A. Davis, B. A. Pailthorpe, G. A. J. Amaratunga and V. S. Veerasamy, *Diam. and Relat. Mater.*, 1994, 3 (4-6), 353-360.
 48. Ab initio simulations of the structure of amorphous carbon, D. G. McCulloch, D. R. McKenzie and C. M. Goringe, *Physical Review B*, 2000, 61 (3), 2349.
 49. Deposition and processing of thin films, Y. Pauleau, *Handbook of thin film materials*, 2002, 1, 455.
 50. Pulsed laser deposition of diamond-like carbon films: reducing internal stress by thermal annealing, P. Mosaner, M. Bonelli and A. Miotello, *Appl. Surf. Sci.*, 2003, 208, 561-565.
 51. Structure and mechanical properties of low stress tetrahedral amorphous carbon films prepared by pulsed laser deposition, M. Bonelli, A. C. Ferrari, A. Fioravanti, A. L. Bassi, A. Miotello and P. M. Ossi, *The European Physical Journal B-Condensed Matter and*

- Complex Systems, 2002, 25 (3), 269-280.
52. Fabrication of delamination free, low stress diamond like carbon (DLC) films using pulsed laser deposition (PLD), A. C. Arjunan, K. Balasundaram, P. Kumar, J. Lee, S. H. Yoon, S. Kim, S. Gupta and R. K. Singh, *Electrochemical and Solid-State Letters*, 2011, 15 (1), H17-H19.
 53. Iron, nitrogen and silicon doped DLC thin films: a comparative study, S. C. Ray, W. F. Pong and P. Papakonstantinou, *Thin Solid Films*, 2016, 610, 42-47.
 54. Non-destructive characterisation of carbon films, A. C. Ferrari, In *Tribology of Diamond-Like Carbon Films*, 2008, Springer, Boston, MA, (pp. 25-82).
 55. Influence of transition metal doping on the tribological properties of pulsed laser deposited DLC films, S. Gayathri, N. Kumar, R. Krishnan, T. R. Ravindran, S. Amirthapandian, S. Dash, A. K. Tyagi and M. Sridharan, *Ceramics International*, 2015, 41 (1), 1797-1805.
 56. Compositional and electrochemical characterization of noble metal– diamond like carbon nano-composite thin films, N. Menegazzo, J. Chunming, R. J. Narayan and B. Mizaikoff, *Langmuir*, 2007, 23 (12), 6812-6818.
 57. Tribological properties of pulsed laser deposited DLC/TM (TM= Cr, Ag, Ti and Ni) multilayers, S. Gayathri, N. Kumar, R. Krishnan, T. R. Ravindran, S. Dash, A. K. Tyagi, B. Raj and M. Sridharan. *Tribology International*, 2012, 53, 87-97.
 58. The deformation and ageing of mild steel: III discussion of results, E. O. Hall, *Proceedings of the Physical Society. Section B*, 1951, 64 (9), 747.
 59. The cleavage strength of polycrystals, N. J. Petch, *Journal of the Iron and Steel Institute*, 1953, 174, 25-28.
 60. Supertough wear-resistant coatings with ‘chameleon’ surface adaptation, A. A. Voevodin and J. S. Zabinski, *Thin Solid Films*, 2000, 370 (1-2), 223-231.
 61. Nano scale investigation of particulate contribution to diamond like carbon film by pulsed laser deposition, M. Panda, G. Mangamma, R. Krishnan, K. K. Madapu, D. N. G. Krishna,

- S. Dash and A. K. Tyagi, RSC Advances, 2016, 6 (8), 6016-6028.
62. Spectroscopic studies on diamond like carbon films synthesized by pulsed laser ablation, M. Panda, R. Krishnan, T. R. Ravindran, Arindam Das, G. Mangamma, S. Dash and A. K. Tyagi. In AIP Conference Proceedings, AIP Publishing, 2016, 1731 (1), 080040.
63. Influence of particulate on surface energy and mechanical property of diamond-like carbon films synthesized by pulsed laser deposition, M. Panda, R. Krishnan, K. K. Madapu, P. Panda, M. Sahoo, R. Ramaseshan, T. Sundari and M. Kamruddin, Appl. Surf. Sci., 2019, 484, 1176-1183.
64. Intrinsic stress modulation in diamond like carbon films with incorporation of gold nanoparticles by PLA, M. Panda, R. Krishnan, N. G. Krishna, K. K. Madapu, and M. Kamruddin, In AIP Conference Proceedings, AIP Publishing, 2018, 1942 (1), 080023.
65. Tuning the tribological property of PLD deposited DLC-Au nano-composite thin films, M. Panda, R. Krishnan, N. G. Krishna, S. Amirthapandian, P. Magudapathy and M. Kamruddin, Ceramics International, 2019, 45 (7), 8847-8855.
66. Vacuum deposited thin films using a ruby laser, H. M. Smith, and A. F. Turner, Applied Optics, 1965, 4 (1), 147-148.
67. Pulsed laser deposition of thin films: applications-led growth of functional materials, R. Eason, A Wiley-Interscience publication (2007), (ISBN No. 0-471-44709-9).
68. Vapor deposition of polystyrene thin films by intense laser vibrational excitation, D. M. Bubb, M. R. Papantonakis, J. S. Horwitz, R. F. Haglund Jr, B. Toftmann, R. A. McGill, and D. B. Chrisey, Chemical physics letters, 2002, 352 (3-4), 135-139.
69. Enhanced photoluminescence in epitaxial ZnGa_2O_4 : Mn thin-film phosphors using pulsed-laser deposition, Y. E. Lee, D. P. Norton, and J. D. Budai, Applied physics letters, 1999, 74 (21), 3155-3157.
70. Effect of ambient pressure on laser ablation and plume expansion dynamics: A numerical simulation, Z. Chen, D. Bleiner, and A. Bogaerts, Journal of applied physics, 2006, 99 (6), 063304.

71. Laser fundamentals, W. T. Silvast, 2nd edition, Cambridge university press, 2004.
72. Available from: web.phys.ksu.edu/vqm/laserweb/Ch-6/6-15.gif.
73. Pulsed laser deposition of thin films, D. B. Chrisey, and G. K. Hubler, Wiley Interscience Publication, 1994 (3).
74. History and future prospects of excimer lasers, D. Basting, K. D. Pippert, and U. Stamm, In Second International Symposium on Laser Precision Microfabrication, 2002, 4426, 25-34. (International Society for Optics and Photonics)
75. Introductory Raman Spectroscopy, J. R. Ferraro, K. Nakamoto, and C. W. Brown, 2nd edition, San Diego, CA: Academic, 2003.
76. An Introduction to Surface Analysis by XPS and AES, J. Watts and J. Wolstenholme, John Wiley & Sons, 2003
77. Atomic force microscope, G. Binning, C. F. Quate, Ch. Gerber and E. Weibel, Phys. Rev. Letts, 1986, 56, 930-933.
78. Atomic force microscopy and spectroscopy, Y. Seo, and W. Jhe, Reports on Progress in Physics 71, 2007, 1, 016101.
79. Quantitative determination of contact stiffness using atomic force acoustic microscopy, U. Rabe, S. Amelio, E. Kester, V. Scherer, S. Hirsekorn, and W. Arnold, Ultrasonics, 2000, 38 (1-8), 430-437.
80. Atomic force acoustic microscopy methods to determine thin-film elastic properties, D. C. Hurley, K. Shen, N. M. Jennett, and J. A. Turner, Journal of applied physics, 2003, 94 (4), 2347-2354.
81. Atomic force acoustic microscopy for quantitative nanomechanical characterization, F. Marinello, P. Schiavuta, S. Vezzù, A. Patelli, S. Carmignato, and E. Savio, Wear , 2011, 271 (3-4), 534-538.
82. Imaging and measurement of local mechanical material properties by atomic force acoustic microscopy, U. Rabe, S. Amelio, M. Kopycinska, S. Hirsekorn, M. Kempf, M.

- Göken, and W. Arnold. Surface and Interface Analysis, 2002, 33 (2), 65-70.
83. SPM characterization of pulsed laser deposited nanocrystalline CrN hard coatings, G. Mangamma, K. Mohan Kant, M. S. R. Rao, S. Kalavathy, M. Kamruddin, S. Dash, and A. K. Tyagi, Journal of nanoscience and nanotechnology, 2007, 7 (6), 2176-2181.
84. Characterization of films with thickness less than 10 nm by sensitivity-enhanced AFM, M. Muraoka, and S. Komatsu, Nanoscale Res Lett, 2011, 6 (1), 33.
85. <https://www.testandmeasurementtips.com/basics-of-the-scanning-electron-microscope/>
86. Encyclopedia of materials characterization: surfaces, interfaces, thin films, C. Brundle, Richard, C. A. Evans, and Shaun Wilson, Gulf Professional Publishing, 1992.
87. Elements of X-ray Diffraction, B. D. Cullity, and S. R. Stock, New Jersey: Prentice hall, 2001, 3.
88. Physical principles of electron microscopy, R. F. Egerton, New York, Springer, 2005, 41.
89. Electron energy-loss spectroscopy in the electron microscope, R. F. Egerton, Springer Science & Business Media, 2011.
90. III. An essay on the cohesion of fluids, T. Young, Philosophical transactions of the royal society of London, 1805, (95): 65-87.
91. Measurement of hardness and elastic modulus by instrumented indentation: Advances in understanding and refinements to methodology, J. W. C. Oliver, and G. M. Pharr, Journal of materials research, 2004, 19 (1), 3-20.
92. Friction and wear mechanisms in MoS₂/Sb₂O₃/Au nanocomposite coatings, T.W. Scharf, P.G. Kotula, S.V. Prasad, Acta Mater. 2020, 58 (1) 4100–4109.
93. Elastic heterogeneities at the nanoscale in DLC films grown by PLD, F. J. F. Ruiz, A. H. Gomez, E. Camps, and F. J. E.-Beltran, Materials Research Express, 2015, 2 (2), 025009.
94. Mechanical properties of diamond-like carbon composite thin films prepared by pulsed laser deposition, Q. Wei, A. K. Sharma, J. Sankar, and J. Narayan, Composites Part B: Engineering, 1999, 30 (7), 675-684.

-
95. Particulates Generated by Pulsed Laser Ablation, L.C. Lin, and L. C. Chen, Wiley, Pulsed Laser Deposition of Thin Films, 1994, 167-198.
 96. The role of ambient gas and pressure on the structuring of hard diamond-like carbon films synthesized by pulsed laser deposition, A. C. Popescu, G. E. Stan, L. Duta, C. Nita, C. Popescu, V. A. Surdu, M. A. Husanu, B. Bitu, R. Ghisleni, C. Himcinschi, and V. Craciun, *Materials*, 2015, 8 (6), 3284-3305.
 97. Effect of substrate bias in amorphous carbon films having embedded nanocrystallites, Ishpal, O. S. Panwar, A. K. Srivastava, S. Kumar, R. K. Tripathi, M. Kumar, and S. Singh, *Surf Coat Technol*, 2011, 206, 155-164.
 98. Effect of substrate bias in nitrogen incorporated amorphous carbon films with embedded nanoparticles deposited by filtered cathodic jet carbon arc technique, O.S. Panwar, Sushil Kumar, Ishpal, A.K. Srivastava, Abhilasha Chouksey, R.K. Tripathi, A. Basu, *Materials Chemistry and Physics*, 2012, 132 (2–3), 659-666.
 99. Structural, nanomechanical, field emission and ammonia gas sensing properties of nitrogenated amorphous carbon films deposited by filtered anodic jet carbon arc technique, R. K. Tripathi, O. S. Panwar, A. K. Srivastava, I. Rawal, and S. Chockalingam, *Talanta*, 2014, 125, 276-283.
 100. Diamond-like carbon thin films for high-temperature applications prepared by filtered pulsed laser deposition, F. Balona, V. Stolojan, S.R.P. Silva, M. Michalka, and A. Kromka, *Vacuum*, 2005, 80, 163–167.
 101. Reflectance and photoluminescence spectra of as grown and hydrogen and nitrogen incorporated tetrahedral amorphous carbon films deposited using an S bend filtered cathodic vacuum arc process, O.S. Panwar, M.. A. Khan, B. Bhattacharjee, A.K. Pal, B.S. Satyanarayana, P.N. Dixit, R. Bhattacharyya, and M.Y. Khan, *Thin Solid Films*, 2006, 515, 1597–1606.
 101. Intrinsic stress and stiffness variations in amorphous carbon, P. C. Kelires, *Diamond and Related Materials*, 2001, 10 (2), 139-144.

102. Deposition mechanisms for promoting sp^3 bonding in diamond-like carbon, J. Robertson, Diamond and related materials, 1993, 2 (5-7), 984-989.
103. Interpretation of Raman spectra of disordered and amorphous carbon, A. C. Ferrari, and J. Robertson, Physical review B, 2000, 61(20), 14095.
104. Resonant Raman spectroscopy of disordered, amorphous, and diamondlike carbon, A. C. Ferrari and J. Robertson, Phys. Rev. B: Condens. Matter Mater. Phys., 2001, 64, 075414,1-13.
105. Structural models of aC and $aC:H$, J. Robertson, Diamond and related materials, 1995, 4 (4), 297-301.
106. Quantitative measurements of sp^3 content in DLC films with Raman spectroscopy, W. G. Cui, Q. B. Lai, L. Zhang, and F. M. Wang, Surface and Coatings Technology, 2010, 205, 7, 1995-1999.
107. Common force field for graphite and polycyclic aromatic hydrocarbons, C. Mapelli, C. Castiglioni, G. Zerbi, and K. Müllen, Physical Review B, 1999, 60, (18), 12710.
108. Modeling studies of amorphous carbon, D. Beeman, J. Silverman, R. Lynds, and M. R. Anderson, Physical Review B, 1984, 30 (2) 870.
109. Ultraviolet and visible Raman analysis of thin a-C films grown by filtered cathodic arc deposition, J. Wasyluk, T. S. Perova, D. W. M. Lau, M. B. Taylor, D. G. McCulloch, and J. Stopford, Diamond. Relat. Mater., 2010, 19, 514–517.
110. Characterization of amorphous and nanocrystalline carbon films, P. K. Chu and L. Li, Mater.Chem. and Phys., 2006, 96, 253–277.
111. Determination of bonding in diamond-like carbon by Raman spectroscopy, A. C. Ferrari, Diamond Relat. Mater., 2002, 11, 1053–1061.
112. Direct quantitative detection of the bonding in diamond-like carbon films using ultraviolet and visible Raman spectroscopy, K. W. R. Gilkes, S. Prawer, K. W. Nugent, J. Robertson, H. S. Sands, Y. Lifshitz, and X. Shi, J. Appl. Phys., 2000, 87, 7283-7289.

-
113. Ultraviolet and visible Raman spectroscopy characterization of diamond-like carbon film growth by pulsed laser deposition, S.M. Huang, Z. Sun, Y.F. Lu, M.H. Hong, *Appl. Phys. A.*, 2002, 74, 519–523.
 114. A comparison of different methods to calculate the surface free energy of wood using contact angle measurements, M. Gindl, G. Sinn, W. Gindl, A. Reiterer, S. Tschegg, *Colloid. Surf. A Phys. Engin. Aspects.*, 2001, 181, 279-287.
 115. Wettability of nanostructured surfaces, L. Duta, A.C. Popescu, I. Zgura, N. Preda and I.N. Mihailescu, Chapter 8 in: "Wetting and Wettability", Dr. Mahmood Aliofkhazraei (Ed.), InTech, 2015, ISBN 978-953-51-2215-9.
 116. Radical modification of the wetting behavior of textiles coated with ZnO thin films and nanoparticles when changing the ambient pressure in the pulsed laser deposition process, A. C. Popescu, L. Duta, G. Dorcioman, I. N. Mihailescu, G. E. Stan, I. Pasuk, I. Zgura et al., *Journal of Applied Physics*, 2011, 110 (6), 064321.
 117. The wetting of steel, DLC coatings, ceramics and polymers with oils and water: The importance and correlations of surface energy, surface tension, contact angle and spreading, M. Kalin., and M. Polajnar, *Applied Surface Science*, 2014, 293, 97-108.
 118. Estimation of the surface free energy of polymers, D. K. Owens, and R. C. Wendt, *Journal of applied polymer science*, 1969, 13 (8), 1741-1747.
 119. The effect of PVD layer constitution on surface free energy, E. Lugscheider, K. Bobzin, M. Möller, *Thin Solid Films*, 1999, 355, 367–373.
 120. Chemical state and wettability of ion-irradiated diamond surfaces, L.Y. Ostrovskaya, A. Dementiev, I. Kulakova, V. Ralchenko, *Diam. Relat. Mater.*, 2005, 14, 486–490.
 121. Wettability of hydrogenated tetrahedral amorphous carbon, F. Piazza, G. Morel, *Diam. Relat. Mater.*, 2009, 18, 43–50.
 122. Correlations between microstructure and hydrophobicity properties of pulsed laser deposited diamond-like carbon films, A. M. Asl, P. Kameli.,; M. Ranjbar, H. Salamati, M. Jannesari, *Superlattices and Microstructures*, 2015, 81, 64–79.

-
123. Studies of diamond and diamond-like film surfaces using XAES, AFM and wetting, L. Y. Ostrovskaya, *Vacuum*, 2002, 68, 219–238.
 124. Pulsed laser deposition of diamond-like carbon coatings for industrial tribological applications, J. M. Lackner, C. Stotter, W. Waldhauser, R. Ebner, W. Lenz, and M. Beutl, *Surface and Coatings Technology* 174, 2003, 402-407.
 125. Determination of the sp^3/sp^2 ratio of aC: H by XPS and XAES , T. Y. Leung, W. F. Man, P. K. Lim, W. C. Chan, F. Gaspari, and S. Zukotynski, *Journal of non-crystalline solids*, 1999, 254 (1-3), 156-160.
 126. Growth mechanisms of DLC films from C^+ ions: experimental studies, Y. Lifshitz, G. D. Lempert, E. Grossman, I. Avigal, C. Uzan-Saguy, R. Kalish, J. Kulik, D. Marton, and J. W. Rabalais, *Diamond and Related Materials*, 1995, 4 (4), 318-323.
 127. Effect of laser intensity on the properties of carbon plasmas and deposited films, H. C. Ong, and R. P. Chang, *Physical Review B*, 1997, 55 (19), 13213.
 128. Mechanical properties of alternating high-low sp^3 content thick non-hydrogenated diamond-like amorphous carbon films, E.H.T. Teo, D.H.C. Chua, B.K. Tay, *Diam. Relat. Mat.*, 2007, 16, 1882-1886.
 129. Comparing hardness and wear data for tetrahedral amorphous carbon and hydrogenated amorphous carbon thin films, P. Lemoine, J. P. Quinn, P. Maguire, J.A. McLaughlin, *Wear*, 2004, 257, 509–522.
 130. Mechanical properties of arc-evaporated CrN coatings: Part I — nanoindentation hardness and elastic modulus, H. Ichimura and I. Ando, *Surf. Coat. Tech.*, 2001, 14, 88-93.
 131. Modulation of residual stress in diamond-like carbon films with incorporation of nanocrystalline gold, R. Paul, S. R. Bhattacharyya, R. Bhar, and A. K. Pal, *Applied Surface Science*, 2011, 257 (24), 10451-10458.
 132. Influence of transition metal doping on the tribological properties of pulsed laser deposited DLC films, S. Gayathri, N. Kumar, R. Krishnan, T. R. Ravindran, S. Amirthapandian, S. Dash, A. K. Tyagi, and M. Sridharan, *Ceramics International* ,2015,

- 41 (1), 1797-1805.
133. Surface plasmon characteristics of nanocrystalline gold/DLC composite films prepared by plasma CVD technique, R. Paul, S. Hussain, S. Majumder, S. Varma, and A. K. Pal, *Materials Science and Engineering: B*, 2009, 164 (3), 156-164.
 134. Nano-mechanical properties of nano-gold/DLC composite thin films, R. Paul, N. Bhadra, A. K. Mukhopadhyay, R. Bhar and A. K. Pal, *Eur. Phys. J. Appl. Phys.*, 2014, 68 (2) 20402.
 135. Spectroellipsometric characterization and modeling of plasmonic diamond-like carbon nanocomposite films with embedded Ag nanoparticles, I. Yaremchuk, S. Meskinis, V. Fitio, Y. Bobitski, K. Slapikas, A. Ciegis, Z. Balevicius, A. Selskis, and Sigita Tamulevicius, *Nanoscale Research Letters*, 2015, 10 (1), 157-164.
 136. Microstructure and nanomechanical properties of pulsed excimer laser deposited DLC: Ag films: Enhanced nanotribological response, M. Constantinou, M. Pervolaraki, P. Nikolaou, C. Prouskas, P. Patsalas, P. Kelires, J. Giapintzakis, and G. Constantinides, *Surface and Coatings Technology*, 2017, 309, 320-330.
 137. Coarsening of mass-selected Au clusters on amorphous carbon at room temperature, R. Popescu, R. Schneider, D. Gerthsen, A. Böttcher, D. Löffler, P. Weis, M.M. Kappes, *Surf. Sci.*, 2009, 603, 3119–3125
 138. Tunability and stability of gold nanoparticles obtained from chloroauric acid and sodium thiosulfate reaction, G. Zhang, J.B. Jasinski, J.L. Howell, D. Patel, D.P. Stephens, A.M. Gobin, *Nanoscale Research Letters*, 2012, 7, 337–345
 139. Pulsed laser deposition of a dense and uniform Au nanoparticles layer for surface plasmon enhanced efficiency hybrid solar cells, V. Resta, A.P. Caricato, A. Loiudice, A. Rizzo, G. Gigli, A. Taurino, M. Catalano, M. Martino, *J. Nano Res.*, 2013, 15, 2017–2023.
 140. Gas sensing with gold-decorated vertically aligned carbon nanotubes, P.R. Mudimela, M. Scardamaglia, O. Gonzalez-Leon, N. Reckinger, R. Snyders, E. Llobet, C. Bittencourt, J.F. Colomer, *Beilstein J. Nanotechnol.*, 2014, 5, 910–918.

-
141. Gold nanoclusters on amorphous carbon synthesized by ion-beam deposition, E. Thune, E. Carpena, K. Sauthoff, M. Seibt, P. Reinke, *J. Appl. Phys.*, 2005, 98 (1–9), 034304.
 142. Core level and valence band photoemission spectra of Au clusters embedded in carbon, K. Takahiro, S. Oizumi, A. Terai, K. Kawatsura, B. Tsuchiya, S. Nagata, S. Yamamoto, H. Naramoto, K. Narumi, M. Sasase, *J. Appl. Phys.*, 2006, 100 (1–6), 084325.
 143. XPS study of supported gold catalysts: the role of Au⁰ and Au^{+δ} species as active sites, M.P. Casaletto, A. Longo, A. Martorana, A. Prestianni, A.M. Venezia, *Surf. Interface Anal.*, 2006, 38, 215–218,
 144. Relationship between structure and CO oxidation activity of ceria supported gold catalysts, A.M. Venezia, G. Pantaleo, A. Longo, G.D. Carlo, M.P. Casaletto, F.L. Liotta, G. Deganello, *J. Phys. Chem. B*, 2005, 109, 2821–2827.
 145. Quantitative near-edge structure analysis of diamond-like carbon in the electron microscope using a two-window method, J. Bruley, D. B. Williams, J. J. Cuomot & D. P. Pappas, *Journal of Microscopy*, 1995, 180, 22- 32.
 146. Improvement of wear resistance of pulsed laser deposited diamond-like carbon films through incorporation of metals, R.J. Wei, J. Narayan, J. Narayan, A.K. Sankar, Sharma, *Mater. Sci. Eng. B*, 1998, 53, 262–266.
 147. Characterization of nanocrystalline gold/DLC composite films synthesized by plasma CVD technique, R. Paul, S. Hussain, A.K. Pal, *Appl. Surf. Sci.*, 2009, 255, 8076–8083.
 148. Tribological properties of nanoparticle-laden ultrathin films formed by covalent molecular assembly, S.R. Puniredd, Y.K. Wai, N. Satyanarayana, S.K. Sinha, M.P. Srinivasan, *Langmuir*, 2007, 23, 8299–8303.
 149. Adhesion and friction studies of nano-textured surfaces produced by self-assembling Au nanoparticles on silicon wafers, X. Zhang, X. Zhong, G. Yi, J. Jia, *Tribol. Lett.*, 2012, 46, 5–73.